# Non-Invasive Diagnostics of Microwave Integrated Circuits Using a Scanning Near-Field Probe

by

ANTHONY S. FORZLEY

A Thesis
Submitted to the Faculty of Graduate Studies
in Partial Fulfillment of the Requirements
for the Degree of

Master of Science

Department of Electrical and Computer Engineering
University of Manitoba
Winnipeg, Manitoba

ISBN 0-315-81712-7

# NON-INVASIVE DIAGNOSTICS OF MICROWAVE INTEGRATED CIRCUITS USING A SCANNING NEAR-FIELD PROBE

BY

ANTHONY S. FORZLEY

A Thesis submitted to the Faculty of Graduate Studies of the University of Manitoba in partial fulfillment of the requirements for the degree of

MASTER OF SCIENCE

# Abstract

The application of scanning near-field probes for non-invasive microwave integrated circuit diagnostics is investigated in this thesis. Presently conventional measurement techniques rely on direct electrical contact with the device under test. However, this provides information only at predetermined locations and is generally incapable of isolating internal fault locations. Direct electrical contacts are invasive in nature and can disturb the normal operation of the circuit under test. With the rapid rate of technological advancement the development of non-invasive measurement systems is becoming even more critical.

While the primary focus of the thesis is on the monopole near-field probe, other technologies in use today are first reviewed. These include electron beam and electro-optic probing which are complex and expensive. A simple inductively coupled loop probe is also discussed. The monopole probe which is capacitively coupled to the device under test is fabricated by simply stripping off a small section of the outer sheath of semi-rigid coax. The length of the monopole affects the probes sensitivity and resolution characteristics. The probe is positioned perpendicular to the plane of the circuit and measures the vertical component of the local electric field.

An integral equation is formulated to model the interaction between the monopole probe and a microstrip transmission line. As a first order approximation a static analysis was undertaken. A method of moments solution is implemented to analyze the resolution and sensitivity characteristics of the probe. While sensitivity is directly proportional to the monopole length, the resolution is a complex function of many parameters. To quantify the resolution, both an experimental and theoretical analysis are required. Preliminary testing indicates good agreement between experimental and theoretical results.

An alternative experimental method for dispersion measurements in open microstrip is presented. The method utilizes the monopole probe to directly measure the voltage standing wave (VSW) on the line under test. The guided wavelength is obtained by measuring the distance between successive voltage minimums. A variety of closed form dispersion expressions are included for comparison with experimental results. Previously investigated methods such as the sliding load and ring resonator techniques are also tested. The maximum rms errors of the various experimental techniques were; sliding load magnitude 3.66%, VSW (combined magnitude and phase) 2.64%, sliding load (phase)

2.02%, and ring resonator 1.28%. The dispersion characteristics and propagation of higher order modes in microstrip lines has also been considered. The cutoff frequencies of such modes have been calculated using the planar waveguide model. The presence of such modes can be directly detected using the scanning near-field probe.

Using a custom designed automated data acquisition system, a variety of microwave circuits were tested at frequencies up to 22 GHz. The measurement system consists of a network analyzer, computer, and a two-axis translation table (μm or mm resolution). The probe can be scanned in either a linear 1D or zig-zag 2D pattern. Tests on transmission lines (microstrip and coplanar), a coupled line filter, and an assortment of antennas have been completed. The results agree with theory and contribute additional information on the internal operation of the circuit.

# Acknowledgments

I wish to express my gratitude and appreciation to my family and friends who have supported me throughout my university education. I consider the completion of this thesis to be as much their success as it is my own. I would also like to thank Dr. G. Bridges for his guidance and encouragement. His knowledge and ideals have contributed a great deal to my development as a professional engineer.

Special thanks to Jeff Dickson and Danny Hajjar for their help with some of the graphics and to Sandra Salomone for her helpful suggestions.

Financial support from the Natural Sciences and Engineering Research Council of Canada and the donation of the test substrate by Rogers Corp. are gratefully acknowledged.

# Table of Contents

# List of Figures

# List of Tables

# Chapter 1

## Introduction

The purpose of this thesis is to investigate the application of electromagnetically coupled probes as non-invasive diagnostic tools for a broad range of microwave circuits. For this purpose, an automated measurement system has been designed and constructed capable of yielding information unavailable from conventional measurement techniques.

While the miniaturization and the enhanced speed performance of integrated circuit is constantly being improved, the experimental measurement of these circuits is becoming increasingly difficult. In fact, the performance characteristics of many devices, especially those based on GaAs technology, have surpassed the capabilities of conventional electronic measurement techniques. As P. May once said "the ability to test the performance of a particular technology underlies the progress in developing that technology" [1].

Conventional circuit measurement techniques rely on some form of direct electrical electrical contact with the point in the circuit being monitored. For example, digital integrated circuits are injected with test patterns and the outputs monitored to determine the overall functionality of the circuit. However this approach does not provide any information on the identification of individual internal faults when one arises. Likewise, conventional network analyzer measurements on microwave circuits impose similar limitations. Typically individual components are designed with a high degree of accuracy and reliability, however the integration of several components on a common substrate often gives rise to uncertainties in circuit performance. Often the performance is degraded by mutual coupling of elements due to the excitation of surface waves, particularly at mm wavelengths. Network analyzer measurements at the device input and output ports are incapable of isolating such problems.

Ideally a measurement device should be non-invasive in nature and capable of measuring waveforms at arbitrary points within the circuit. Depending on the application it may be desirable to perform voltage and/or current measurements. Preferably with magnitude and phase data. In addition, the measurement system must possess sufficient spatial and temporal resolution. Developing a measurement system with such characteristics is challenging and critical to the future development of reliable high quality integrated circuits.

The scope of the thesis is as follows. Chapter 2 provides a review of some of the non-invasive measurement techniques currently being researched within industry and the academic community. The relative advantages and disadvantages of each technique are discussed and sample measurements provided.

Chapter 3 is an introduction to the coaxial monopole probe and the formulation of an equivalent model for numerical analysis. The appropriate Green's functions are derived and the numerical results based on a Method of Moments solution are compared with experimental data.

A description of the hardware and software required for the automated data acquisition system is given in chapter 4.

Chapter 5 includes a discussion on dispersion and impedance analysis of open-microstrip. A summary of design equations is included for reference. In addition, a brief introduction to the dispersion characteristics of higher order modes is included. The experimental methods for determining the dispersion characteristics are discussed in chapter 6. A variety of experimental results are compared with closed-form dispersion formulas.

A broad range of measurement examples on microwave circuits is provided in chapter 7. Measurements were performed on printed antennas, transmission lines (coplanar and microstrip), and a coupled line filter.

Finally, chapter 8 includes some conclusions and recommendations for future research.

# Chapter 2

## Review of Non-Invasive Measurement Techniques

A brief summary of mechanical, electron-beam, and electro-optic probing techniques is presented. This summary will also state the main advantages and disadvantages of each technique and include sample measurements.

### 2.1 Mechanical Probes

The limitations of conventional mechanical probes have been cited by many researchers [2],[3] attempting to develop new and non-invasive measurement techniques. With the continuous decrease of device dimensions and push towards operating frequencies in the high GHz range the application of mechanical probes are becoming increasingly limited. Such probes tend to have inherently limiting factors from both an electrical and mechanical viewpoint.

Mechanical probe shortcomings such as inaccurate manipulation and their invasive nature are difficult if not impossible to overcome. The task of positioning probes mounted on a micro-manipulator and guided by view under an optical microscope is tedious and time consuming. Probe manipulation is limited by optical microscopes having spatial resolutions on the order of microns, short depth of foci, and extremely small working distances. As a result, the proper positioning of the probe is very difficult and potentially hazardous to the device under test. It is not uncommon for devices to fail due to open or short circuit lines caused by the probe. Probing multiple lines such as on a data bus is unpractical due to the amount of hardware one must work with. Typically one would work with no more than four mechanical probes at any one time.

An additional drawback involves the placement of probe pads which must be incorporated in the preliminary design stage. The number of such probe pads must be

limited since they occupy valuable real estate. As transistor sizes continue to decrease, the ratio of probe pad area to transistor area will increase as will the value of the area occupied. Therefore, the circuit designer must be judicious in the number probe pads implemented at the design stage.

From an electrical viewpoint one must consider the capacitive loading effects of the probe on the circuit. Excessive capacitive loading can influence the normal operation of the circuit. This problem is compounded by the development of smaller transistors which are capable of driving node capacitances on the order of femtofarads ($10^{-15}$). The ability of such transistors to drive the additional capacitance of the probe (typically a few pF) is questionable and can lead to a degradation of circuit performance. Also the increased circuit capacitance can easily alter signal measurements by increasing rise and fall times due to filtering of high frequency components.

Despite many drawbacks mechanical probes maintain two advantages. The first is the ability to inject signals at nodes which is a valuable option that is not readily available by any other means. The other advantage is cost, which in comparison to other technologies is minimal.

## 2.2 Electron Beam Probing

Several variations of electron-beam probing stations are in use today throughout industry and research institutions. The electron beam tester is based on a modified scanning electron microscope as shown in Fig. 2.1. A typical electron-beam probe station consists of:

- An electron gun for emitting primary electrons.
- A lens focusing system for focusing the primary electrons on the target.
- Equipment to collect and detect secondary electrons.
- Electronics for data acquisition and analysis.
- A high speed beam chopper for sampling measurements.

The electron gun which generates low energy primary electrons can either be of the field or thermionic emission type. In comparison, field emission guns are considered more desirable than the thermionic emission guns because of their high brightness and small probe diameter [4]. Emitted primary electrons are accelerated through a potential on the order of 0.5 to 2.5 kV. As the electrons are accelerated they are focussed via the lens focussing system to a submicron spot on the device under test (DUT). On impact with the

DUT, low energy secondary electrons are randomly emitted as a result of elastic collision. These secondary electrons have a well defined distribution of kinetic energies ranging from 0 to 20 eV.

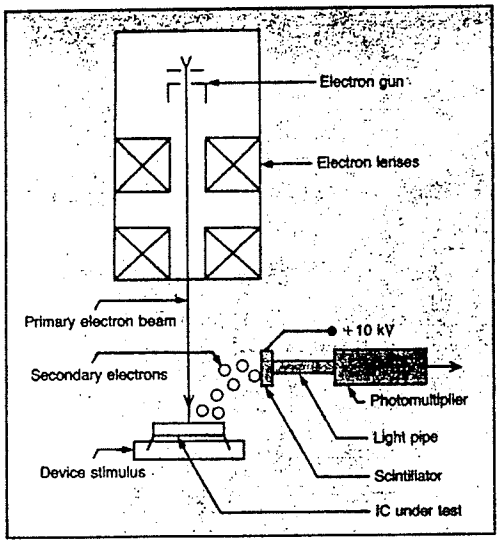


Figure 2.1. Electron beam probing equipment [2].

The secondary electrons are then collected and counted. One method of collecting the secondary electrons involves using a high potential electrostatic extraction field generated at the surface of the DUT. An alternate collecting method is to use a magnetic extraction field thus eliminating the need for the electrostatic field. The secondary electrons are put through a scintillator which converts the electrons into photons. These photons are then fed to a photomultiplier which generates a specific number of electrons for each incident photon. The photomultiplier output can be used to measure the voltage at the location of incidence of the primary electrons. It can be seen in Fig. 2.2 that probing a +5V transmission line will emit less secondary electrons then that of a -5V line. This is due to low energy electrons being attracted to the metal conductor by the positive potential of the +5V line while the negative potential of the -5V line repels such electrons.

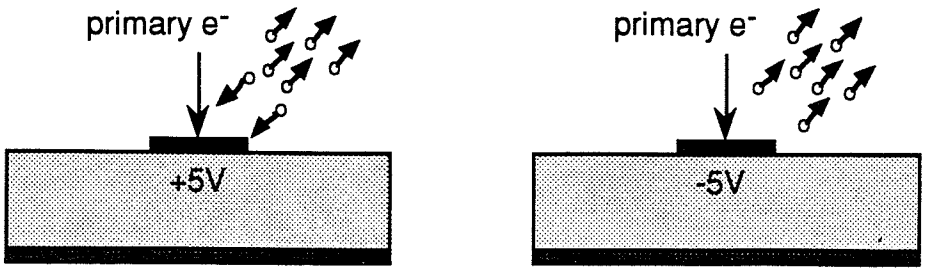


Figure 2.2. Secondary electrons (a) trapped by +5V potential, (b) repelled by -5V potential.

In general, the number of secondary electrons is inversely proportional to the potential within a limited vicinity of the point of impact of the primary electron beam. When a circuit is scanned with the electron beam the output of the photomultiplier is monitored. When converted to output for a video display, areas with a positive potential appear dark indicating low second electron yield, while negative areas appear bright indicating high second electron yield. This contrast in the video display output forms the basis for a process called *voltage-contrast imaging* [2],[3].

Measuring waveforms may be done in either an open-loop or closed-loop fashion where the secondary electron current is maintained at a constant level. Analog waveforms can be traced accurately with the closed loop system but the data acquisition time is increased by the settle time of the feedback loop. Alternatively, open loop measurements of digital waveforms may be quicker as the number of collected secondary electrons is compared to the threshold level to determine whether a high or low logic state exists. In order to achieve better performance, that is faster data acquisition, the electron beam can be chopped in order to create a sampling system. The beam chopper is simply an electronically controlled aperture for periodically blocking the flow of primary electrons. In this manner, the measurement bandwidth is limited by the smallest electron beam pulse that can be generated. Performance of a commercial system (Schlumberger IDS 5000) has been compared to a sampling oscilloscope with a rise time of 100 ps [2]. Specifications for an electron beam probe as described in [4] are included in table 2.1.

Table 2.1. Performance of an electron beam probing station [4].

| | |
|---|---|
| Electron probe | 0.1 $\mu$m |
| Potential detection | Range: +15 to−15 V<br>Resolution: 0.1 V |
| Time resolution | 1 ns |
| Electron gun | Cold-type field emission |
| Mode | Image mode: SE image, PD image, SPD image |
| Specimen stage | DIP package socket |
| Electron energy | 500–1000 V |

SE: Secondary electron
PD: Potential distribution
SPD: Stroboscopic potential distribution

Probing bare conductors is relatively straight forward but probing of buried (passivated) conductors presents additional complications. Probing bare conductors yields the potential on the conductor, while probing buried conductors yields the surface potential. The passivation layer acts as dielectric which capacitively couples the surface to the buried conductor. The electrical behavior of the buried conductor can be inferred from the surface measurement. The limitation here is that only AC signals can be measured reliably since any surface charge will leak and reestablish equilibrium. Reliable measurement of DC voltages is typically not possible due to the presence of a surface charge. The surface charge arises when the number of secondary electrons does not equal the number of primary electrons. This yield factor is a function of accelerating potential and dielectric material. Todokoro [4] has experimentally shown that the secondary electron yield approaches unity on PSG films when primary electrons exist with 1 keV of energy, thus the charging of electrons on the surface should be negligible.

In Fig. 2.3 the address buffer output of a 4 Kbit RAM is measured using both a mechanical probe and an electron beam probe, also included is a computer simulation for reference. The computer simulation and the electron beam measurement compare favorably with a delay time of 2.2 ns. The mechanical probe measurement exhibits a delay of 7.5 ns due to stray capacitance. While mechanical probes have a loading capacitance on the order of a few pF an electron beam probe has a capacitance on the order of $10^{-5}$ pF [4], thus explaining the discrepancies in delay times. A variety of applications such as measuring internal waveforms on a 1-K bipolar PROM, 1 GHz Gunn diode, and a 4-K MOS RAM can be found in [5].

Though electron-beam probing is impressive with its high temporal resolution (1ps - 1ns) and submicron spatial resolution it is a complex and expensive technology with inherent limitations. For instance the degree of testability of various integrated circuits is directly related to implementing special fabrication guidelines as outlined in [3]. Implementing such guidelines at the design level and subsequent fabrication can be both time consuming and expensive. Improvement is also required to obtain DC voltage measurements on buried conductors and amplitude measurements of AC signals superposed on a DC bias. Crosstalk from electric fields of nearby transmission lines is another factor and can affect the results by roughly 10% [4]. The electrical characteristics of the device under test may be altered as a result of the primary electrons penetrating into sensitive areas. This effect is most notable in MOS devices [4],[5] where the energy of the

primary electrons must be at a level which does not cause a significant shift in the threshold voltage of the transistor.

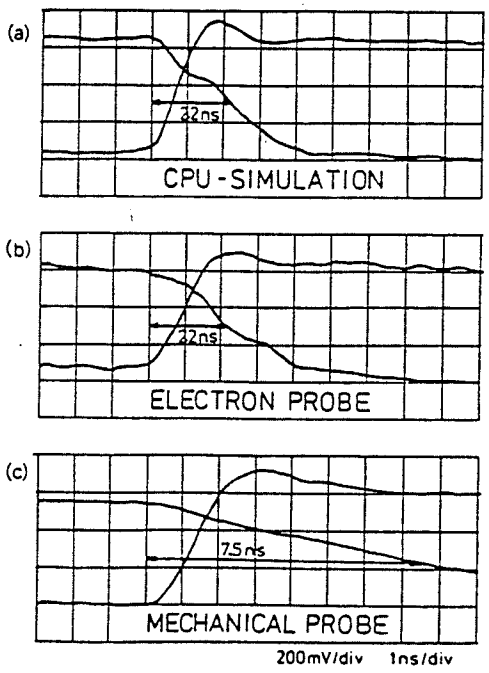


Figure 2.3. Waveforms at the address buffer output of a 4 Kbit RAM: (a) computer simulation; (b) by electron-beam tester ; (c) by mechanical probe tester [4].

## 2.3 Electro-Optic Probing

Electro-optic probing is a rather new technology developed based on the well known electro-optic effect [6]. When an electric field is applied across an electro-optic crystal the electron distribution is perturbed so that the polarizability and hence the refractive index of the medium changes anisotropically. As a result, the polarization of the light passing through the crystal is changed. This change which is linearly related to the electric field is known as the Pockells effect and can be measured optically.

While certain material such as GaAs and $LiTaO_3$ exhibit the Pockells effect others such as silicon do not. Two common forms of electro-optic probing include direct or internal electro-optic sampling and external electro-optic sampling as shown in Figs. 2.4a,b respectively.

In direct electro-optic sampling (Fig. 2.4a) the DUT is fabricated on a substrate that exhibits the electro-optic effect. As a result the polarization of the probe beam is altered via the electro-optic effect in the substrate. For external sampling (Fig. 2.4b) the DUT need

not be fabricated on an electro-optic substrate. Instead an electro-optic crystal is fused to the sampling head, hence allowing the electric fringing fields to penetrate the sampling crystal. The probe beam does not penetrate the DUT instead it is reflected off a reflective coating on the bottom of the crystal. Therefore the beam traverses the electric field twice before reaching the optical measurement system.

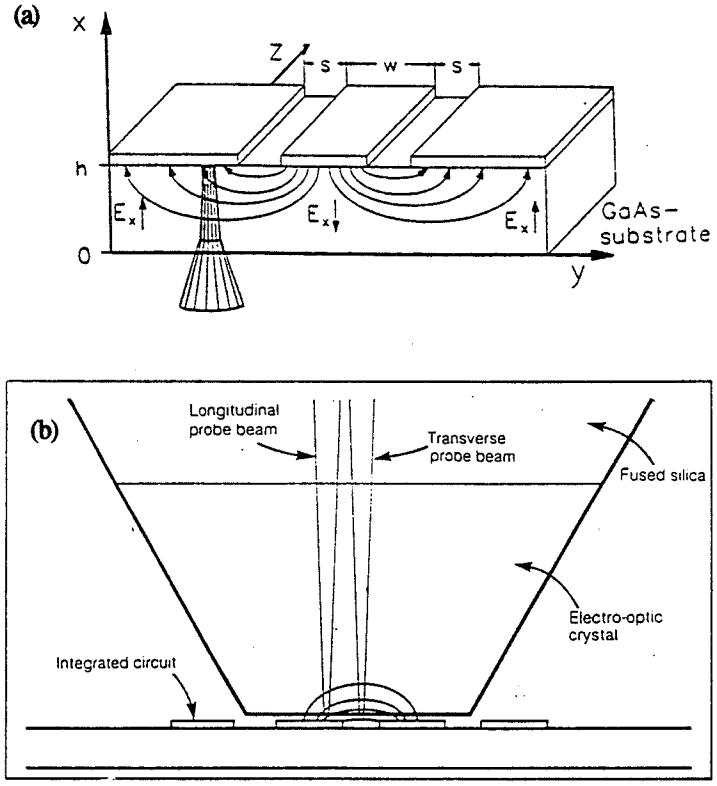


Figure 2.4. Common forms of electro-optic probing (a) direct backside probing geometry for a coplanar waveguide [7]; (b) external electro-optic probing [8].

Electro-optic probes can be sensitive to either longitudinal or transverse field components. In longitudinal probing the electro-optic effect is exhibited only for electric fields applied along the same axis and parallel to the optical beam. The advantage of this being that the crystals sensitive only to the fields normal to surface of the DUT which are strongest directly above conductors. Hence a quantity which is proportional to the voltage on the line can be measured reliably. In contrast, transverse probing is sensitive to electric fields parallel to the surface of the DUT. The disadvantage of this method is that it is highly susceptible to crosstalk from neighboring elements.

Operating in a longitudinal or transverse probing mode is dependent on the type of crystal utilized. The general layout of the external electro-optic sampling system is shown in Fig. 2.5. Here the laser source generates a beam which is split into two. One of these

beams repetitively triggers the electrical signal to be measured. This can be done directly by exciting a photosensitive device on the device under test, or indirectly by generating an electrical pulse via a photodetector coupled to the DUT. The other beam synchronously samples the induced change in polarization due to the electro-optic crystal.

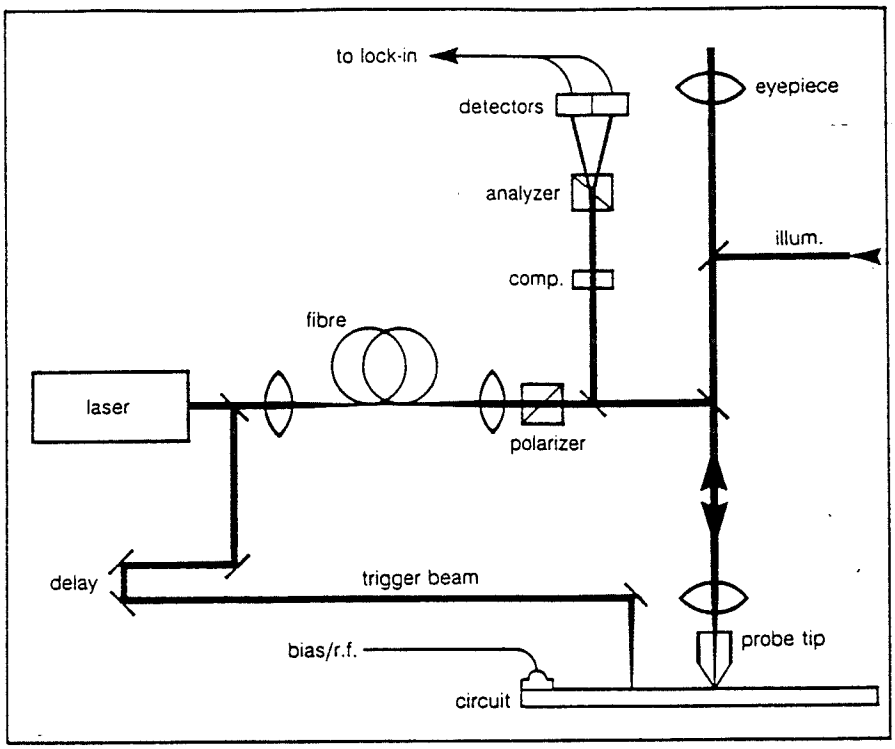


Figure 2.5. The general layout of the external electro-optic sampling system [8].

Electro-optic probing systems are capable of superior temporal resolution below 1 ps, however this requires expensive lasers. Spatial resolution is typically limited by the diameter of the focussed laser or the size of the smallest crystal which can be effectively implemented for external electro-optic probing. The smallest crystal is on the order of 1μm. A variety of sample measurements are available in the literature [7],[8],[9],[10]. The applications cover a broad range of topics including MMIC's, printed antennas, signal tracing on digital integrated circuits, and measurement of propagation delays. Electro-optic scanning of the coplanar waveguide in Fig. 2.4a at 2 kHz yields the results shown in Fig.2.6. The width of the center line is 40 μm and the spacing to the outer ground planes is 26μm. The substrate is a 410 μm thick GaAs with 3μm thick gold conductors. The electric fields have also been successfully mapped at 8.5 GHz.

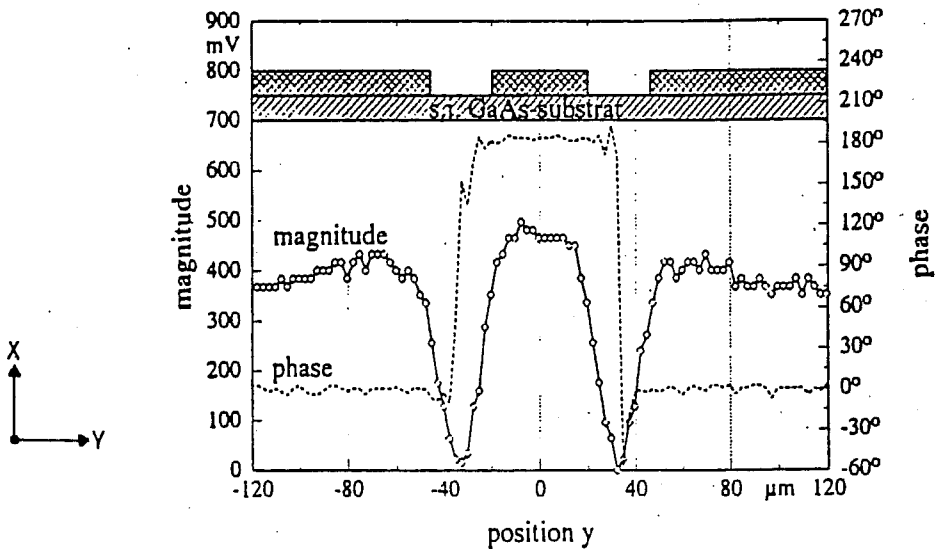


Figure 2.6. Measured magnitude and phase of the electro-optic signal (proportional to the electric field $E_x$) as a function of beam position y for a fixed z position [7].

As with electron beam probing, electro-optic probing is a complex and expensive technology. With temporal and spatial resolutions on the order of 1ps and 1μm respectively it is a very attractive technology. One area which requires considerable attention is that of voltage calibration [11]. Another area of uncertainty is the possible capacitive loading of the electro-optic crystals such as $LiTaO_3$ ($\varepsilon_r$=45). The perturbation of the electric field above above the DUT may affect the normal operation of the DUT. In addition, the minimization of crosstalk must be addressed by utilizing crystals suitable for longitudinal probing configurations. In spite of these difficulties, electro-optic sampling shows great promise as a high speed measurement technique for a broad range of devices.

## 2.4 Magnetic Field Double Loop Probe

Several attempts have been made at designing probes which are sensitive either to magnetic or electric fringing fields. An approximate form of the fields on a planar microstrip structure is shown in Fig. 2.7. Such probes should be lightly coupled to the DUT so as not to disturb its normal operation. Ideally these type of probes would require less expensive and more conventional measurement equipment.

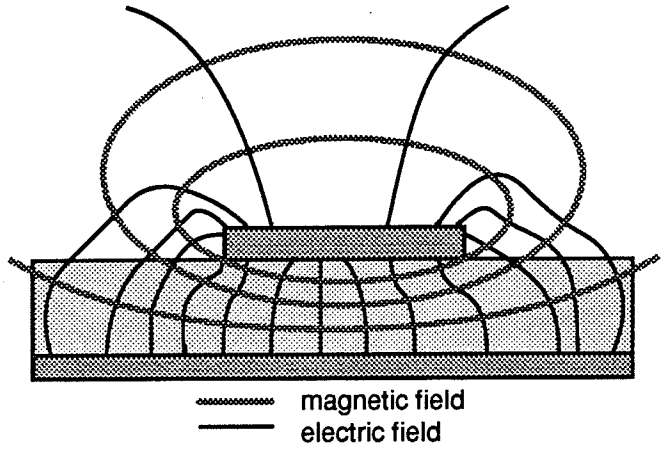


Figure 2.7. Approximate pattern of the fields generated by a typical circuit board trace.

The optimal design of a non-contacting magnetic field probe for measurements on the interior of planar high frequency circuits has been investigated [12]. The double loop probe shown in Fig. 2.8 is fed by a coplanar waveguide (CPW). The probe and the CPW feed are at right angles to one another.

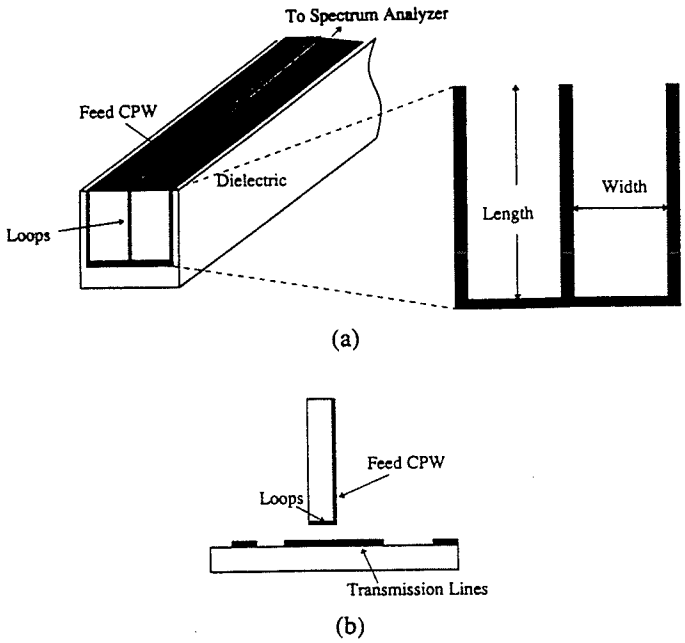


Figure 2.8. (a) Double-loop magnetic-field probe. (b) Probe in position over circuit under test [12].

The unique double loop design ensures that the probe response to radiation originating from distant sources is rejected. In Figs. 2.9a,b it is evident that the induced currents in the loops add constructively, however in Fig. 2.9c magnetic coupling from distant sources tend to induce currents in opposition to one another. Therefore, contributions from uniform distant sources tend to cancel and have no effect on the probe.

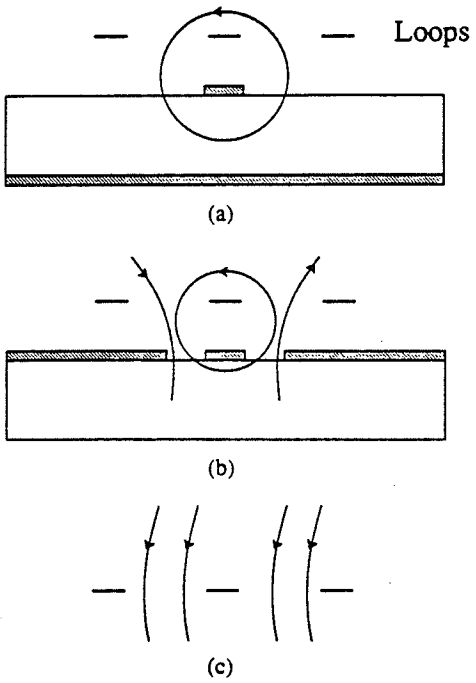


Figure 2.9. Double-loop magnetic probe coupling to magnetic fields of (a) microstrip, (b) coplanar waveguide. Radiation arriving from a distant source, as in (c), interacts with the two loops in such a way that their contributions tend to cancel [12].

The probe design arrived at in [12] was a result of both theoretical analysis and scale-model experiments. The model probe fabricated had a length of 15 mm, width of 7 mm, and conductor width of 0.25 mm for operation at 0.28 GHz. For operation at 28 GHz these probe dimensions must be scaled down by a factor of 100. The loop dimensions are a tradeoff between resolution, magnetic field sensitivity, and far field radiation rejection. Increasing the loop dimensions effectively decreases the resolution and far field radiation rejection efficiency while increasing the magnetic field sensitivity. In addition, the probe dimensions must be a small fraction of the wavelength at the test frequency of interest.

Two other design factors include the CPW feed and the width of the conductors forming the loops. To avoid mutual coupling between the CPW feed and the DUT a metal

shielding box is required. The box which partially shields the CPW feed must make good electrical contact with the outer planes of the CPW feed. The width of the conducting line influences the sensitivity of the probe to electrostatic coupling which can give rise to significant errors. The line width should be chosen as narrow as possible while ensuring that the conductor resistance and self inductance are negligible.

A typical measurement system is shown in Fig. 2.10. The magnitude of the induced probe current is measured by the spectrum analyzer. Phase measurements are obtained by mixing a reference signal of the same frequency with the probe signal. A phase shifter is then adjusted until the two signals are in phase and the magnitude reading on the spectrum analyzer is maximum. The variable phase shift is then compared relative to a reference point on the circuit.

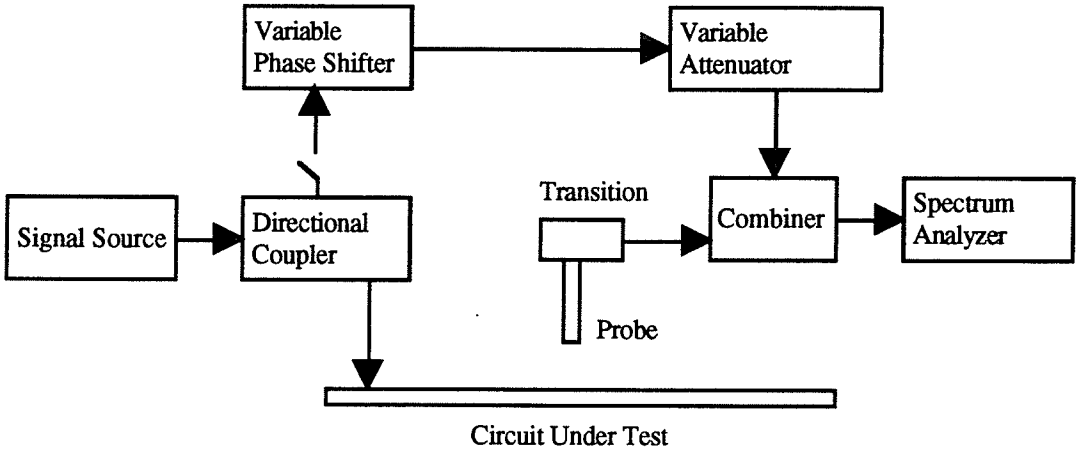


Figure 2.10. Configuration for magnitude and phase measurements [12].

The magnitude and phase response of the scale model probe as it was scanned along a loaded microstrip transmission line are shown in Figs. 2.11a,b respectively. It is assumed that similar results could be obtained for measurements at 28 GHz with all model dimensions scaled down by 100 times. The magnitude of a transverse scan of the line at 150 MHz is shown in Fig. 2.11c. The tri-lobed configuration can be explained with the help of Fig. 2.9. The center maximum corresponds to the situation illustrated in Fig. 2.9a where the magnetic coupling induces currents which add constructively. As the probe transverses from the center of the line we notice a null which corresponds to Fig. 2.9c where the induced currents are in opposition to one another. The side lobes arise as the probe continues to move further from the center of the line and the coupling tends to be with the nearest loop. The loop probe has also been used for S-parameter measurements [12].

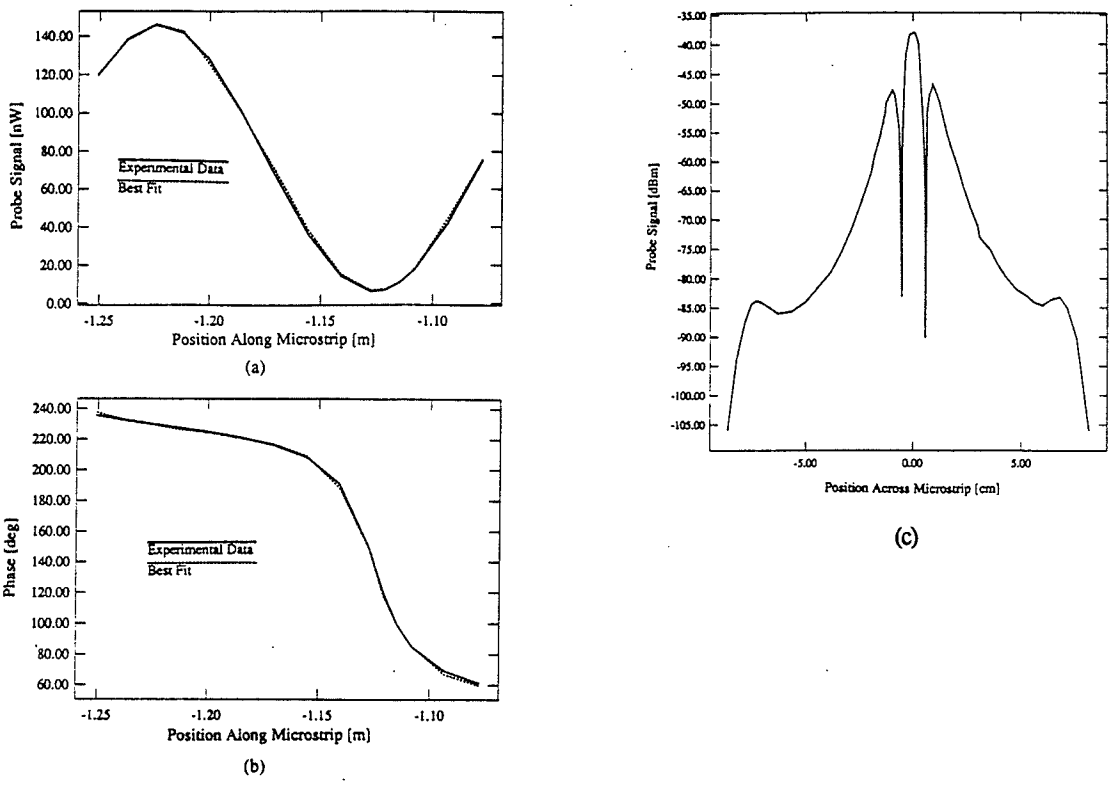


Figure 2.11. Experimental and best-fit curves of (a) The square-magnitude and (b) The phase of a standing wave. The measurement was made at 280 MHz using a scale model probe placed at a height of 2.4 mm above a microstrip having a center conductor width of 5 mm, and a dielectric with $\varepsilon_r$=12 and thickness 6.35 mm. (c) Transverse pattern of an open-circuited microstrip at 150 MHz [12].

Osofsky and Schwarz [12] cite 3 main sources of error which are: 1) uncontrolled variations in the physical position of the probe; 2) disturbance by the probe of the circuit being measured; and 3) undesirable electrostatic coupling. From scale model measurements it was found that for standing wave ratios less than 3.0 the magnitude accuracy is better than 0.8 dB and the phase better than 7° when compared to numerical calculations [12]. S-parameter measurements were accurate to within 1 dB for the magnitude and 5° for phase.

The fabrication of reliable small scale probes for operation at 28 GHz is a major problem. Conventional photolithography techniques have so far proven to be unreliable [13]. One of the difficulties is in establishing good electrical contact between the loops and CPW feed which are at right angles to one another. If a new fabrication method is devised which can produce reliable small scale probes the loop probe could become a viable diagnostic tool.

# Chapter 3

## Numerical Modeling of the Monopole Near-Field Probe

In contrast to the loop probe described in chapter 2 which is primarily an inductively coupled structure, a coaxial probe has been developed which is a capacitively coupled structure. The coaxial probe illustrated in Fig. 3.1 has received considerable attention from both an experimental and theoretical viewpoint [14],[15],[16],[17],[18]. The ease of fabrication and commercial availability of semi-rigid coaxial cable in variety of sizes (outer diameter $D_o \geq 0.008$") are two attractive features of such probes.

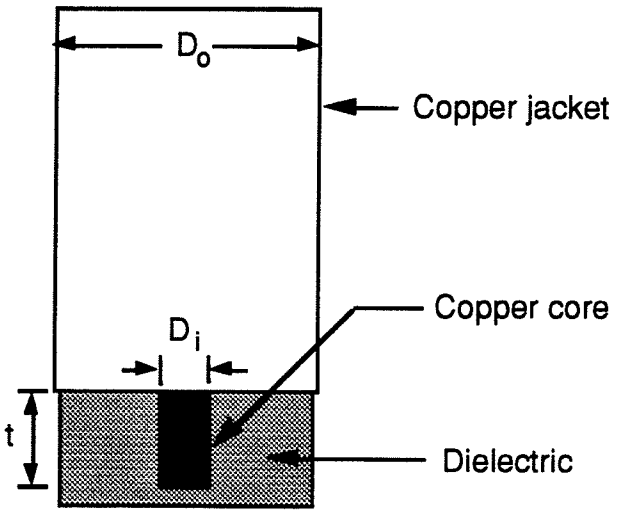


Figure 3.1. Monopole near field probe.

The coaxial probe is sensitive to the local charge density and essentially measures the vertical component of the electric field close to the surface of the DUT. A potential difference between the inner and outer conductors is induced when the center conductor protrudes beyond the outer conductor in the form of a monopole of length t (Fig. 3.1). The surrounding dielectric provides support to the tip and prevents it from making direct contact

with the DUT. Although an exact theoretical model is unavailable Frayne [16] has developed a preliminary model which he used to model the interaction between a coaxial probe and an isolated conducting strip of finite width and infinite length.

Some fundamental properties of the coaxial probe are now discussed. Firstly, the spatial resolution of the probe is not purely a factor of the coax outer diameter. Instead, the operating frequency and standing wave ratio on the structure must also be considered. Rapid phase variation at the voltage minima makes detecting these points difficult and error prone.

Secondly, the sensitivity of the probe is directly proportional to the tip length t. As t increases so does the number of electric field lines terminating on the center conductor, hence a greater potential difference between the conductors is induced. On the other hand, the resolution as a function of tip length is difficult to calculate and cannot be readily quantified. The most tactical approach to quantify the resolution would be to incorporate both an experimental and theoretical analysis on probes of various sizes and tip lengths.

Finally, the net probe response is due to both capacitive and inductive coupling. The magnetic field coupling is due to the transverse magnetic field component which is proportional to the axial current density (Fig. 3.2). Ideally, the coaxial probe should respond only to electric field coupling, hence it is the natural dual of the loop probe. In contrast, while the coaxial probe measurement error arises from magnetic field coupling, the error in the loop probe measurement is due to electric field coupling.

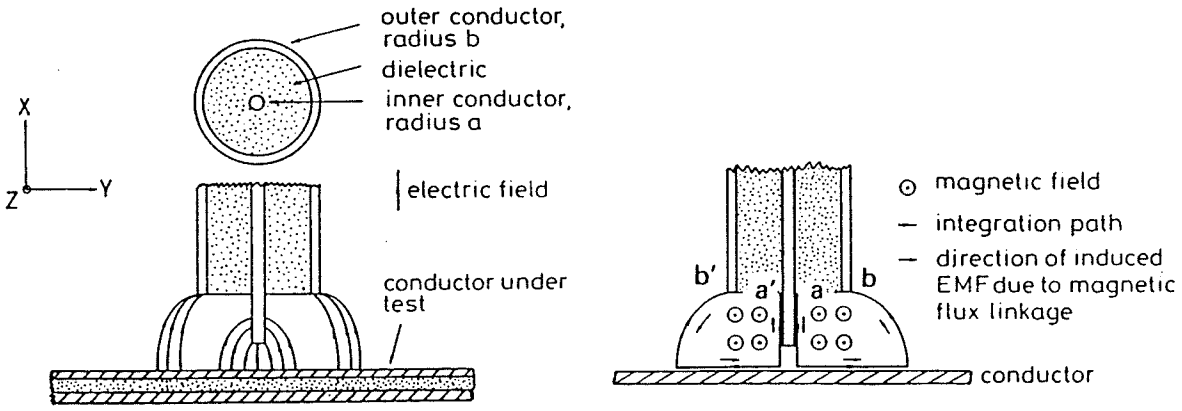


Figure 3.2. Electric and magnetic field coupling of monopole probe [16].

The useable bandwidth of the coaxial probe is a function of its dimensions. Both the tip length and outer diameter must be a small fraction of the wavelength in the medium being measured. This restriction is necessary to avoid any spurious radiation by the probe. The measurement error incurred as a result of undesirable magnetic field coupling is another limitation. It has been shown [16] that the magnitude and phase errors decrease with the outer diameter and increase frequency, also substrates with high permittivities tend to have a high degree of magnetic coupling.

## 3.1 Monopole Probe and Equivalent Circuit Model

In many cases numerical modeling is used to predict performance characteristics and aid in the decision of whether or not the chosen probe design is feasible. In addition, there can be great savings in experimental costs and testing time. Another benefit of formulating a numerical model rather than relying on experimental data is that once the code is formulated it can be used for a variety of test cases with varying parameters. It is for these and several other reasons that an equivalent circuit model has been developed.

The spatial resolution and sensitivity characteristics of the probe have been analyzed using a probe/transmission line structure as shown in Fig. 3.3 along with the corresponding equivalent circuit model. Since at the typical operating frequencies all the critical coupling dimensions are much smaller than the wavelength in the medium being measured, a static analysis will provide an adequate analytical approximation and is used to model the circuit probe coupling. The problem is formulated by determining the various coupling capacitances shown in Fig. 3.3. For a given probe location and transmission line excitation voltage the differential mode induced voltage between the inner and outer conductors of the coax can be calculated. The spatial resolution is then obtained by a transverse scan at discrete intervals of the microstrip line. The same approach may also be taken to obtain resolution information for buried transmission lines. An integral equation formulation is used to calculate the unknown coupling capacitances used in the equivalent circuit model. From this model, assuming the capacitance $C_{ol}$ is small the induced voltage is given as [19]

$$V^{ind} = \phi_l \frac{Z_t j\omega C_{il}}{1 + Z_t j\omega (C_{ii} + C_{oi} + C_{il})}. \tag{3.1}$$

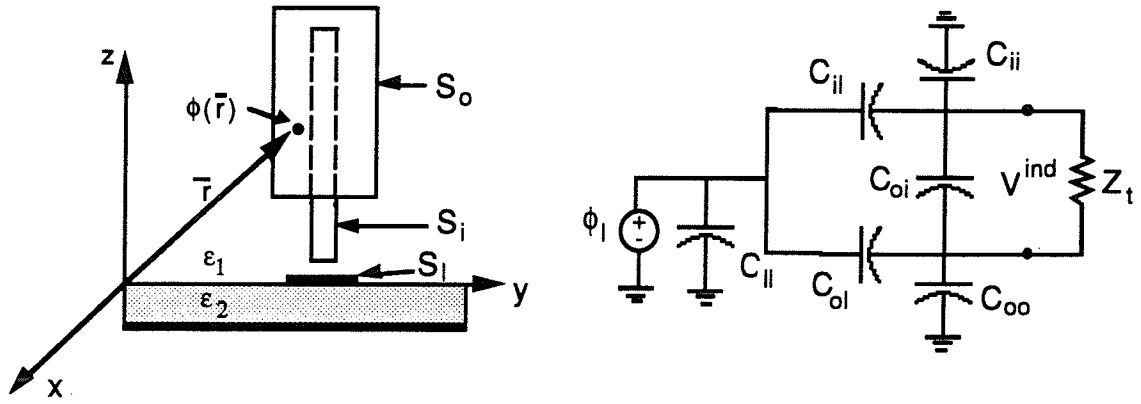


Figure 3.3. Probe and microstrip line along with the corresponding equivalent circuit model.

### 3.1.1 Integral Equation Formulation

The formulation of an integral equation determines the unknown charge distribution $\sigma(\bar{r})$ on the surfaces of the outer and inner conductors and the printed circuit line, $S_o$, $S_i$, and $S_l$ respectively. Potentials on each of these surfaces are then specified, $\phi_o$, $\phi_i$, and $\phi_l$, so that an integral equation can then be developed which satisfies all boundary conditions

$$\phi(\bar{r}) = \iint_{S_o+S_i+S_l} \sigma(\bar{r}')G(\bar{r},\bar{r}')d\bar{r}', \quad \bar{r} \in S_o, S_i, S_l. \tag{3.2}$$

A complete formulation of the integral equation requires the Green's function $G(\bar{r},\bar{r}')$ for a unit point charge located embedded within (0>z'>-d) or above (z'>0) the dielectric of a grounded dielectric slab as shown in Fig. 3.4. Therefore the Green's functions can be used to model microstrip or buried transmission lines. Of course the two solutions should converge for the case of a point charge located at z'=0. Derivation of the Green's function for the case of the charge above the dielectric requires that above the dielectric Poisson's equation be solved subject to the boundary conditions that both the normal flux density and the potential be continuous at z=0. Within the dielectric region Laplace's equation must be solved subject to the boundary condition that the tangential electric field must be zero at z= -d. Likewise, the same boundary conditions are applied for the case of the point charge embedded within the dielectric but with the regions of solution for Laplace's and Poisson's equations reversed.

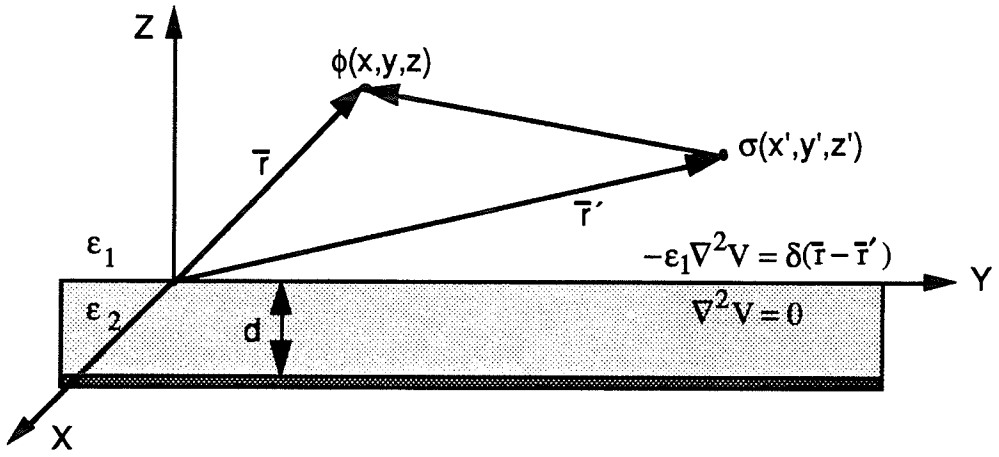


Figure 3.4. Point charge over a grounded dielectric slab.

To solve the system of partial differential equations in Fig. 3.4, first consider the case of a point charge in a homogeneous medium of permittivity ε. The potential is given by

$$V = \frac{q}{4\pi\varepsilon r} \tag{3.3a}$$

where $r=\sqrt{\rho^2+(z-z')^2}$ is the radial distance from q to the observation point expressed in cylindrical coordinates. Using a Bessel transform [20] it can be shown that (3.3a) can be expressed in an equivalent integral form as

$$V = \frac{q}{4\pi\varepsilon}\int_0^\infty J_0(\lambda\rho)e^{-\lambda|z-z'|}d\lambda. \tag{3.3b}$$

### 3.1.2 Green's Function Derivation

#### 3.1.2.1 Point Charge Above a Grounded Dielectric Slab

Using the results of (3.3a) and (3.3b) the integral equations for the potential due to a point charge above the dielectric substrate (z′>0) can be expressed in terms of the integral transform as

$$V(\rho,z) = \frac{q}{4\pi\varepsilon_1}\int_0^\infty\left[e^{-\lambda|z-z'|} + Re^{-\lambda(z+z')}\right]J_0(\lambda\rho)d\lambda \qquad ;z>0 \tag{3.4a}$$

$$V(\rho,z)=\int_0^\infty\left[C_1e^{-\lambda z}+C_2e^{\lambda z}\right]J_0(\lambda\rho)d\lambda \qquad ;0>z>-d \qquad (3.4b)$$

where R, $C_1$, and $C_2$, are unknown coefficients to be determined by applying the appropriate boundary conditions. Equation (3.4a) satisfies certain properties that are expected. For instance, the potential in the region z>0 contains a singularity at the source (as $\rho\rightarrow 0$ and $z=z'$) which is a diminishing quantity as $z\rightarrow\infty$. The $Re^{-\lambda(z+z')}$ term is included to account for an image charge of strength R located at $z=-z'$. In contrast, the lower region (0>z>-d) contains no singularity and since z is finite both $e^{-\lambda z}$ and $e^{+\lambda z}$ terms are included.

To determine the unknown coefficients, the appropriate boundary conditions must be applied. At the perfectly conducting base z=-d the tangential electric field component must vanish, therefore

$$E_\rho\Big|_{z=-d}=-\frac{\partial V}{\partial\rho}\Big|_{z=-d}=0. \qquad (3.5)$$

Applying this condition to (3.4b) implies that the integrand must equal zero and yields

$$C_1=-C_2e^{-2\lambda d}. \qquad (3.6)$$

Continuity of potential at z=0 implies that the integrand of (3.4a) equals the integrand of (3.4b). Substituting (3.6) into (3.4b) and enforcing this condition gives

$$\frac{q}{4\pi\varepsilon_1}e^{-\lambda z'}(R+1)=C_1\left(1-e^{2\lambda d}\right). \qquad (3.7)$$

Finally, enforcing the continuity of the normal flux density begins with obtaining the $D_z$ components of (3.4a,b). By applying $D=-\varepsilon\nabla V$ to (3.4a,b) we obtain

$$D_{z1}=-\varepsilon_1\frac{\partial V}{\partial z}=-\frac{q}{4\pi}\int_0^\infty\lambda\left(e^{-\lambda(z'-z)}-Re^{-\lambda(z'+z)}\right)J_0(\lambda\rho)d\lambda \qquad ;z>0 \qquad (3.8)$$

$$D_{z2}=-\varepsilon_2\frac{\partial V}{\partial z}=\varepsilon_2\int_0^\infty\lambda C_1\left(e^{-\lambda z}+e^{\lambda(z+2d)}\right)J_0(\lambda\rho)d\lambda \qquad ;0>z>-d \qquad (3.9)$$

At z=0, $D_{z1}$ must equal $D_{z2}$ which results in

$$\frac{q}{4\pi\varepsilon_1}e^{-\lambda z'}(1-R)=-\frac{\varepsilon_2}{\varepsilon_1}C_1\left(1+e^{2\lambda d}\right). \tag{3.10}$$

Equations (3.6), (3.7), and (3.10) constitute a set of three equations and three unknowns. The R coefficient is obtained by dividing equation (3.7) by (3.10) which yields the same result as given in [20]

$$R=-\left[\frac{1-(\varepsilon_1/\varepsilon_2)\tanh\lambda d}{1+(\varepsilon_1/\varepsilon_2)\tanh\lambda d}\right]. \tag{3.11}$$

The $C_1$ coefficient is then obtained by substituting (3.11) into (3.7), while $C_2$ then follows from (3.6) with the final results given by

$$C_1=\frac{q}{4\pi\varepsilon_1}\frac{2e^{-\lambda z'}}{\left(1-e^{2\lambda d}\right)\left(1+(\varepsilon_2/\varepsilon_1)\coth\lambda d\right)} \tag{3.12}$$

$$C_2=\frac{q}{4\pi\varepsilon_1}\frac{2e^{-\lambda z'}}{\left(1-e^{-2\lambda d}\right)\left(1+(\varepsilon_2/\varepsilon_1)\coth\lambda d\right)}. \tag{3.13}$$

The integral equations (3.4a,b) are now complete.

### 3.1.2.2 Point Charge Embedded Within a Grounded Dielectric Slab

For the case of a buried point charge (0>z′>-d) the integral equations for the potential in the two regions are expressed as

$$V(\rho,z)=\int_0^\infty Te^{-\lambda z}J_0(\lambda\rho)d\lambda \qquad ;z>0 \tag{3.14a}$$

$$V(\rho,z)=\int_0^\infty\left[\frac{q}{4\pi\varepsilon_2}e^{-\lambda|z-z'|}+C_3e^{-\lambda z}+C_4e^{\lambda z}\right]J_0(\lambda\rho)d\lambda \quad ;0>z>-d \tag{3.14b}$$

where the unknown coefficients are obtained by applying the appropriate boundary conditions. The integral equation (3.14a) for z>0 consists of the factor $Te^{-\lambda z}$ which

approaches zero for large z and T is considered the transmission coefficient. For this case the singularity appears in (3.14b) when $z=z'$ and $\rho \to 0$.

At the perfectly conducting base z=-d the tangential electric field component expressed in (3.5) must be zero. Enforcing this boundary condition results in

$$C_4 = -\left[\frac{q}{4\pi\varepsilon_2} e^{-\lambda z'} + C_3 e^{2\lambda d}\right]. \tag{3.15}$$

Continuity of potential requires that the integrand of (3.14a) equal that of (3.14b) at z=0. The result is

$$T = \frac{q}{4\pi\varepsilon_2} e^{\lambda z'} + C_3 + C_4. \tag{3.16}$$

Continuity of the flux density at z=0 leads to

$$T = \frac{\varepsilon_2}{\varepsilon_1}\left[\frac{q}{4\pi\varepsilon_2} e^{\lambda z'} + C_3 - C_4\right]. \tag{3.17}$$

After some lengthy algebraic manipulations of (3.15), (3.16), and (3.17) explicit expressions for T, $C_3$, and $C_4$, were found to be

$$T = \frac{q}{4\pi\varepsilon_2}\left[\frac{2(\cosh\lambda z' \tanh\lambda d + \sinh\lambda z')}{1+(\varepsilon_1/\varepsilon_2)\tanh\lambda d}\right] \tag{3.18}$$

$$C_3 = \frac{q}{4\pi\varepsilon_2}\left[\frac{2((\varepsilon_1/\varepsilon_2)\sinh\lambda z' - \cosh\lambda z')}{(1+e^{2\lambda d})(1+(\varepsilon_1/\varepsilon_2)\tanh\lambda d)}\right] \tag{3.19}$$

$$C_4 = \frac{q}{4\pi\varepsilon_2}\left[\frac{2(\cosh\lambda z' - (\varepsilon_1/\varepsilon_2)\sinh\lambda z')}{(1+e^{-2\lambda d})(1+(\varepsilon_1/\varepsilon_2)\tanh\lambda d)} - e^{\lambda z'}\right]. \tag{3.20}$$

### 3.1.2.3 Summary of Green's Functions

Utilizing equations (3.3a), (3.3b), and expanding the hyperbolic functions in terms of their exponential representation the Green's functions can be extracted from integral equations (3.4a,b), and (3.14a,b).

For a point charge above the dielectric surface $z' \geq 0$

$$G(\bar{r},\bar{r}') = \begin{cases} \dfrac{1}{4\pi\varepsilon_1}\left[\dfrac{1}{|\bar{r}-\bar{r}'|} - \displaystyle\int_0^\infty \left[\dfrac{(\varepsilon_1/\varepsilon_2)\tanh\lambda d - 1}{(\varepsilon_1/\varepsilon_2)\tanh\lambda d + 1}\right] e^{-\lambda(z+z')} J_0(\lambda\rho)\,d\lambda\right] & ;z > 0 \\ \dfrac{1}{4\pi\varepsilon_1}\left[\displaystyle\int_0^\infty \dfrac{2\sinh\lambda(d+z)}{\sinh\lambda d + (\varepsilon_2/\varepsilon_1)\cosh\lambda d} e^{-\lambda z'} J_0(\lambda\rho)\,d\lambda\right] & ;0 \geq z > -d \end{cases} \tag{3.21}$$

For a point charge embedded within the dielectric $0 > z' > -d$

$$G(\bar{r},\bar{r}') = \begin{cases} \dfrac{1}{4\pi\varepsilon_1}\left[\displaystyle\int_0^\infty \dfrac{2\sinh\lambda(d+z')}{\sinh\lambda d + (\varepsilon_2/\varepsilon_1)\cosh\lambda d} e^{-\lambda z} J_0(\lambda\rho)\,d\lambda\right] & ;z > 0 \\ \dfrac{1}{4\pi\varepsilon_2}\left[\dfrac{1}{|\bar{r}-\bar{r}'|} - \displaystyle\int_0^\infty \left[\dfrac{(\varepsilon_2/\varepsilon_1)\cosh\lambda z' - \sinh\lambda z'}{\sinh\lambda d + (\varepsilon_2/\varepsilon_1)\cosh\lambda d} e^{-\lambda(z+d)} - \dfrac{(\varepsilon_2/\varepsilon_1 - 1)\sinh\lambda(d+z')}{\sinh\lambda d + (\varepsilon_2/\varepsilon_1)\cosh\lambda d} e^{\lambda z}\right] J_0(\lambda\rho)\,d\lambda\right] & ;0 \geq z > -d \end{cases} \tag{3.22}$$

where $|\bar{r}-\bar{r}'| = \sqrt{(x-x')^2 + (y-y')^2 + (z-z')^2}$ and $\rho = \sqrt{(x-x')^2 + (y-y')^2}$.

A special case of interest occurs when $z'=0$ which is useful for modeling microstrip transmission lines. It can be shown that both (3.21) and (3.22) converge to the same solution with the potential given by

$$V(\rho,z) = \frac{q}{4\pi\varepsilon_1}\int_0^\infty \frac{2\varepsilon_1/\varepsilon_2}{\varepsilon_1/\varepsilon_2 + \coth\lambda d} J_0(\lambda\rho)\,d\lambda \qquad ;z>0 \tag{3.23}$$

In an attempt to reduce computation time an approximation has been derived which eliminates the integral in equation (3.4a) for $z>0$ [20]. The approximation is derived by expanding the $\tanh(\lambda d)$ term in (3.11) into a Maclaurin series as follows

$$R = -\left[\frac{1-(\varepsilon_1/\varepsilon_2)\left(\lambda d - \frac{2}{3!}(\lambda d)^3 + \ldots\right)}{1+(\varepsilon_1/\varepsilon_2)\left(\lambda d - \frac{2}{3!}(\lambda d)^3 + \ldots\right)}\right]$$

$$R = -\left[1 - 2\left(\frac{\varepsilon_1}{\varepsilon_2}\right)\lambda d + \ldots\right]$$

$$\approx -e^{-2(\varepsilon_1/\varepsilon_2)\lambda d} \tag{3.24}$$

where (3.24) is obtained from the truncation of the Maclaurin series for $e^x \approx 1+x$ for small x. Substituting (3.24) into the original integral equation (3.4a) gives

$$V(\rho,z) \approx \frac{q}{4\pi\varepsilon_1}\int_0^\infty \left[e^{-\lambda|z-z'|} - e^{-\lambda(z+z'+2d(\varepsilon_1/\varepsilon_2))}\right] J_0(\lambda\rho)\,d\lambda \tag{3.25}$$

from which the Green's function can be written as

$$G(\bar{r},\bar{r}') \approx \frac{1}{4\pi\varepsilon_1}\left[\frac{1}{|\bar{r}-\bar{r}'|} - \frac{1}{\sqrt{(x-x')^2+(y-y')^2+(z+z'+2d\varepsilon_1/\varepsilon_2)^2}}\right] \tag{3.26}$$

where (3.26) is only to be used when the following constraint equation is satisfied

$$2d\frac{\varepsilon_1}{\varepsilon_2} << \sqrt{(z+z')^2+\rho^2}\,. \tag{3.27}$$

To check the accuracy of the approximation the image factor of the Green's functions given in (3.21) and (3.26) are compared in Fig. 3.5 for various values of $z+z'$. The substrate parameters are $\varepsilon_r=2.2$ and $d=0.508$ mm. The integration in equation (3.21) was computed using a gaussian quadrature technique. In Fig. 3.5 excellent agreement is obtained except for the case $(z+z')=0.2$ mm and $\rho<0.5$ mm. When used under circumstances which ensure that the Green's function approximation is reasonably accurate considerable computation time can be saved due to the elimination of the integration.

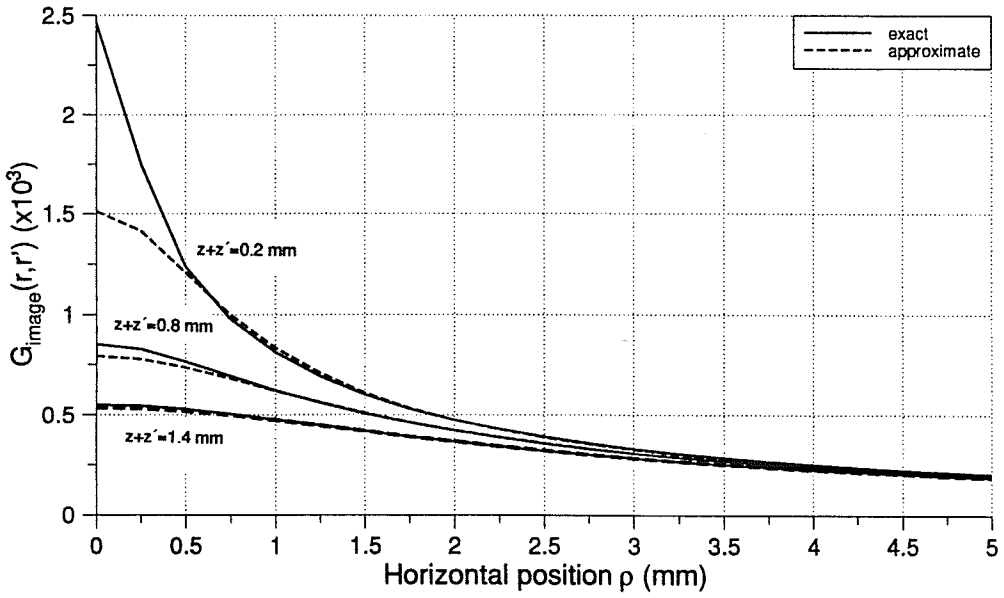


Figure 3.5. Comparison of the exact and approximate image factor term of the Green's function for a point charge above a grounded dielectric slab.

## 3.2 MOM Integral Equation Solution

To solve the resulting integral equation numerically a method of moments (MOM [21]) solution was utilized. The coupling capacitances of Fig. 3.1 can then be calculated. As shown in Fig. 3.6, the charge distribution $\sigma(\bar{r})$ was expanded using pulse basis expansion functions as

$$\sigma(\bar{r}) = \sum_{i=1}^{N} \frac{q_i}{A_i} \cdot \Omega_i(\bar{r}) \tag{3.28}$$

where $\sigma(\bar{r})$ is approximated as a constant charge $q_i$ on each patch. $A_i$ is the area of each patch with $\Omega_i$=1 if $\bar{r}$ is located on the patch and zero otherwise. Using the original integral equation a matrix is created by using delta testing functions at the center points of each patch, Using (3.28) the integral equation

$$\phi(\bar{r}) = \int_S \sigma(\bar{r}')G(\bar{r},\bar{r}')d\bar{r}' \tag{3.29}$$

can be written as a linear set of equations as

$$\phi(\bar{r}_j) = \sum_{i=1}^{N} \frac{q_i}{A_i} \int_{A_i} G(\bar{r}_j, \bar{r}')d\bar{r}', \quad j = 1,2,...N \tag{3.30}$$

where j varies from 1 to N (N being the total number of patches). An NxN matrix is thus developed in terms of the N unknown charges and potentials specified at N surface points.

$$\begin{bmatrix} \phi_1 \\ \vdots \\ \phi_N \end{bmatrix} = \begin{bmatrix} G_{11} & \cdots & G_{1N} \\ \vdots & \ddots & \vdots \\ G_{N1} & \cdots & G_{NN} \end{bmatrix} \begin{bmatrix} q_i \\ \vdots \\ q_N \end{bmatrix} \tag{3.31}$$

$$G_{ji} = \frac{1}{A_i} \int_{A_i} G(\bar{r}_j, \bar{r}')d\bar{r}' \tag{3.32}$$

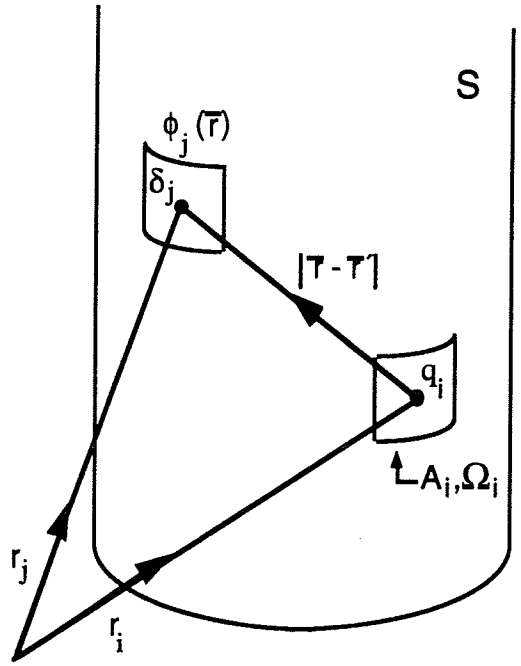


Figure 3.6. MOM expansion.

To solve for [q] the potentials [$\phi$] are specified and the interaction matrix [G] inverted. The unknown coupling capacitances may then be obtained. For example, the capacitance between the center conductor and the transmission line $C_{il}$ is determined by specifying $\phi_I$=1V, $\phi_i$=$\phi_o$=0V and integrating the charge induced on the center conductor as

$$C_{il} = \frac{1}{\phi_1} \int_{S_i} \sigma(\bar{r}')d\bar{r}' \tag{3.33}$$

Similar forms are used to calculate $C_{ol}$ and $C_{io}$.

The code for the MOM solution was written in Fortran [22]. A transmission line of finite length was modeled using a patch segmentation so that effects of charge perturbation on the line can be monitored. As a first order approximation the dielectric spacer in the coax was not taken into account. A typical segmentation with roughly 1200 patches is shown in Fig. 3.7.

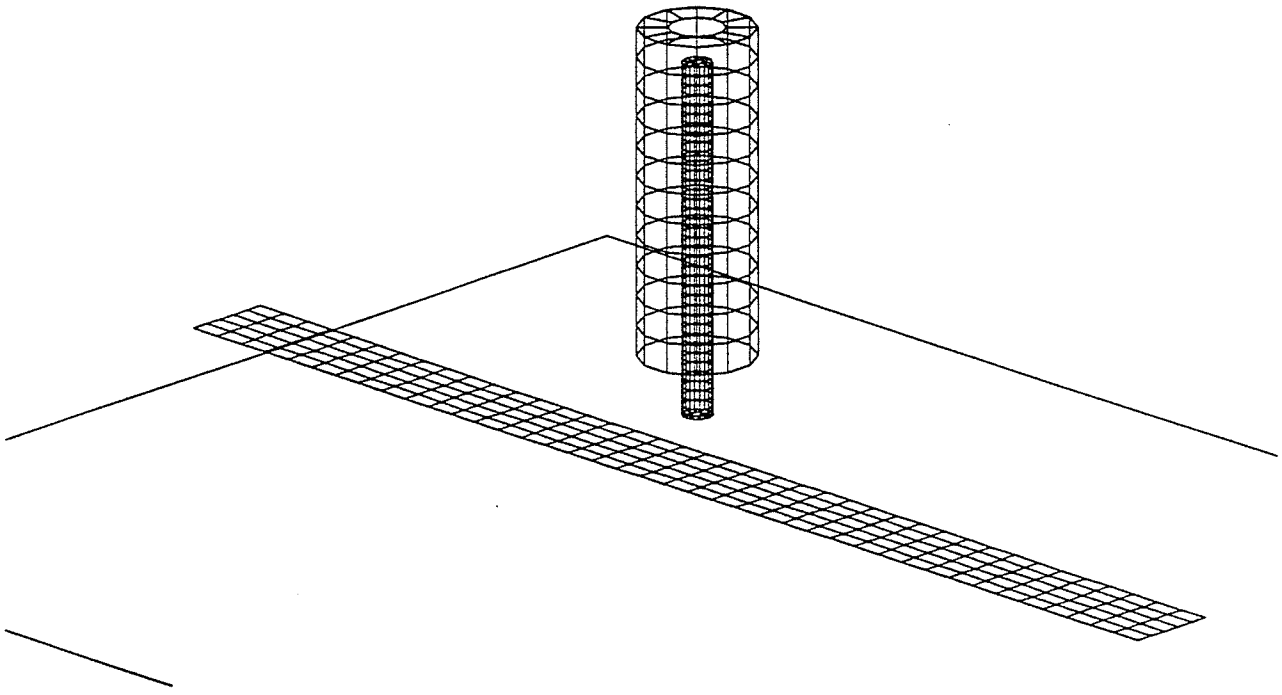

Figure 3.7. Segmentation for MOM solution.

## 3.3 Numerical and Experimental Comparison

In order to compare experimental and analytical results a transverse scan of the probe over a transmission line was investigated. The configuration tested experimentally and theoretically analyzed is shown in Fig. 3.8. Information on the measurement system can be found in chapter 4.

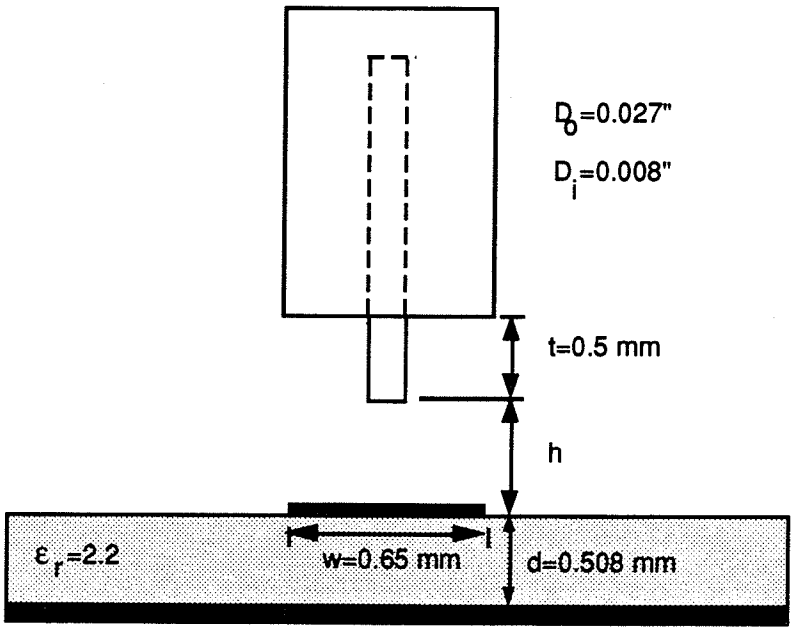


Figure 3.8. Sensor cross section used for simulation and experimental test.

With the potentials specified as $\phi_l$=1 V, and $\phi_i$=$\phi_o$=0 V equation (3.33) can be used to calculate the critical coupling capacitance $C_{il}$. Fig. 3.9 is a plot of $C_{il}$ for various heights h of the probe above the line and incremental displacements relative to the center of the line. The approximate formula for the Green's function (3.26) was used in the theoretical analysis. It is readily visible from the case of h=0.5 mm that $C_{il}$ decreases with increasing $\varepsilon_r$ ($\varepsilon_r$=1.0 and 2.2) of the dielectric substrate. This is to be expected since the electric field tends to concentrate beneath the transmission line with increasing $\varepsilon_r$. The length of the probe modeled was chosen such that the charge density at the point of termination was negligible relative to the density near the tip. In addition, the length of transmission line modeled must be chosen such that the calculated capacitance values converge. Calculation of the remaining coupling capacitances shown in Fig. 3.1 and additional results can be found in [22].

Finally, a comparison between experimental and theoretical results is plotted in Fig. 3.10. Three transverse scans of the transmission line of Fig. 3.8 were performed at heights h=0.5, 1.0, 1.5 mm. Experimental results were measured at an operating frequency of 1 GHz. Agreement is very good over a broad range. The discrepancy between the two sets of data can be contributed to both experimental and modeling errors. The predominant experimental error occurs when calibrating the height of the probe above the transmission line, especially for small h values where the probe response is more sensitive to height fluctuations. An approximation in the numerical model is that the outer conductor was assumed to have zero thickness when in reality it does not. Additional results for a similar configuration can be found in [22] where a test frequency of 5 MHz was used.

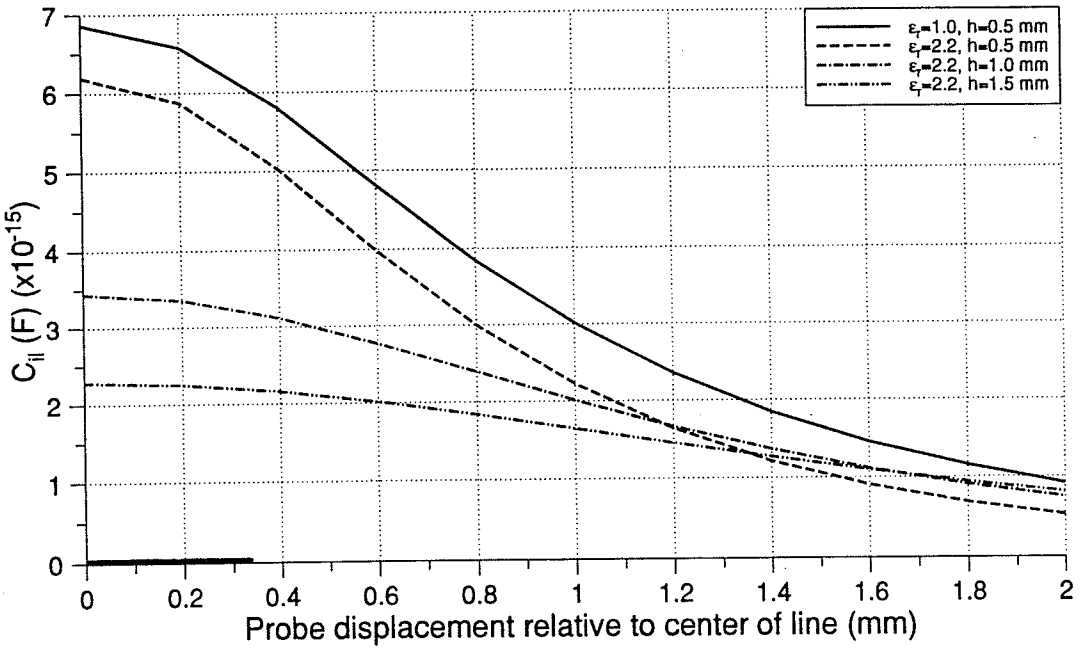


Figure 3.9. Calculation of the critical coupling capacitance.

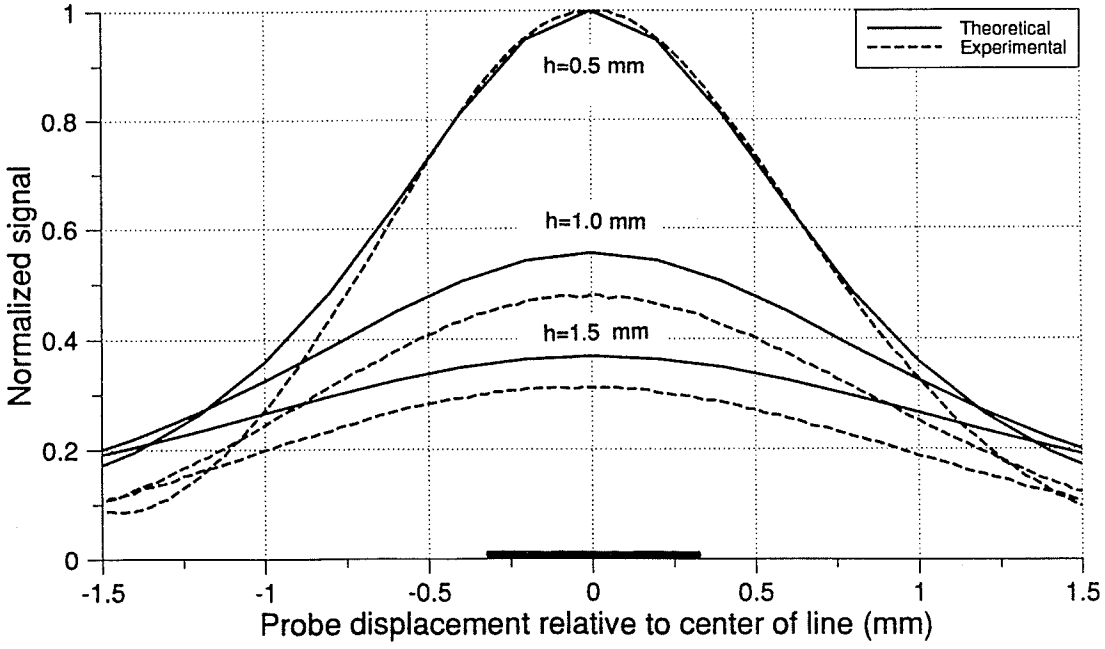


Figure 3.10. Comparison of experimental and analytical results for h=0.5, 1.0, and 1.5 mm at f=1 GHz.

# Chapter 4

## Automated Data Acquisition System

As one would expect, the design of an automated measurement system for near-field probing is both hardware and software intensive. Both the software and hardware must be flexible in order to facilitate testing on wide range of applications. The software required for such a system must be user friendly and capable of driving various measurement instruments. Since experiments may require μm or mm scale resolution depending on the circuit dimensions two sets of hardware apparatus are required. The corresponding probe design and its characteristic dimensions must compliment the application. This chapter briefly describes both the hardware and software required for the measurement system used to obtain the experimental results.

### 4.1 Hardware Requirements

The measurement system shown in Fig. 4.1 consists of a Wiltron 360 network analyzer, a computer workstation, and a two axis translation table. The computer acts as the central controller which positions the probe via the serial port and subsequent data acquisition via the general purpose interface bus (GPIB or also commonly known as the IEEE-488 standard). The IEEE-488 interface is superior in terms of flexibility, speed of data acquisition, and accuracy when compared to previous systems which required independent analog to digital convertors [17].

Depending on the application two different translation tables were used. For applications requiring mm or sub-mm sampling intervals the HP7220C plotter has proven to be reliable and versatile. The scan area of the plotter is limited by the design of the probe support. Currently scans on the order of 15 cm by 28.5 cm with a minimum step resolution of 0.025 mm. Alternatively, for probing on small scale circuits where μm to

sub-μm resolution is required a DC motor driven table was used. Two limitations of the DC motors are backlash and speed. If the backlash of each motor is known it can be compensated for in the software. The minimum step size is 0.1 μm with each axis capable of 25 mm of movement.

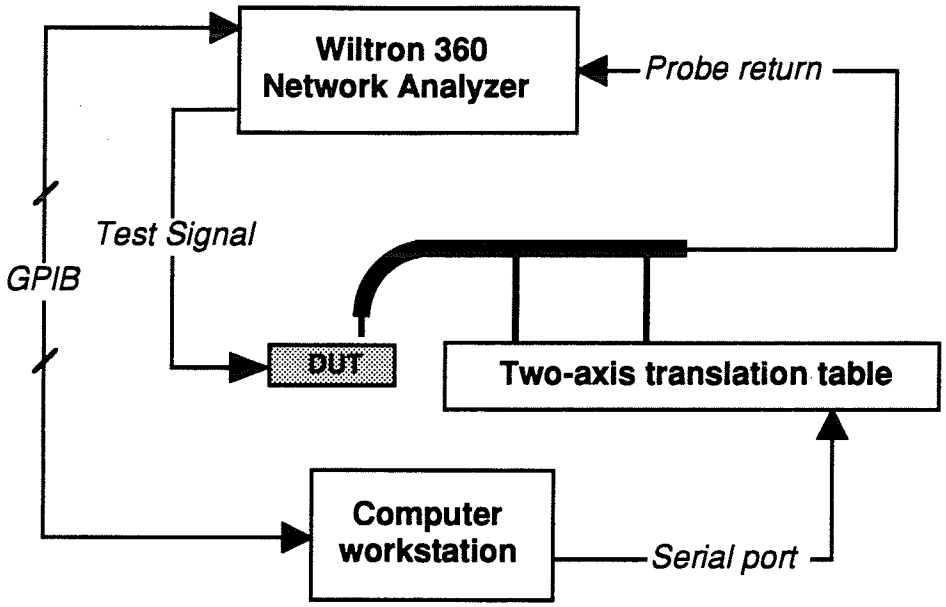


Figure 4.1. Block diagram of measurement system.

Fig. 4.2 is a picture of the coaxial probe scanning a cavity resonator antenna (see chapter 7 for results). The white coaxial cable connects the probe to the network analyzer shown in the background. This cable must be flexible to minimize any torque exerted on the probe.

Fig. 4.3a is a picture of of the apparatus required for μm-resolution scans. On the left-hand side is the DC motor driven table while on the right-hand side we see the CPW transmission line feed. When using coaxial probes whose dimensions inhibit direct connection to a SMA connector some ingenuity is required. In Fig. 4.3a the coax ($D_o$=0.013" and $D_i$=0.0031") is soldered directly to a larger coax ($D_o$=0.0865" and $D_i$=0.0201") which inturn directly mates with a SMA connector. For slightly larger coax it is possible to use an intermediary microstrip transmission line to construct a coax-microstrip-SMA configuration. To investigate the effects of the discontinuities introduced to the transmission line, time domain measurements can be performed. Fig. 4.3b shows all the major components required for the experiment.

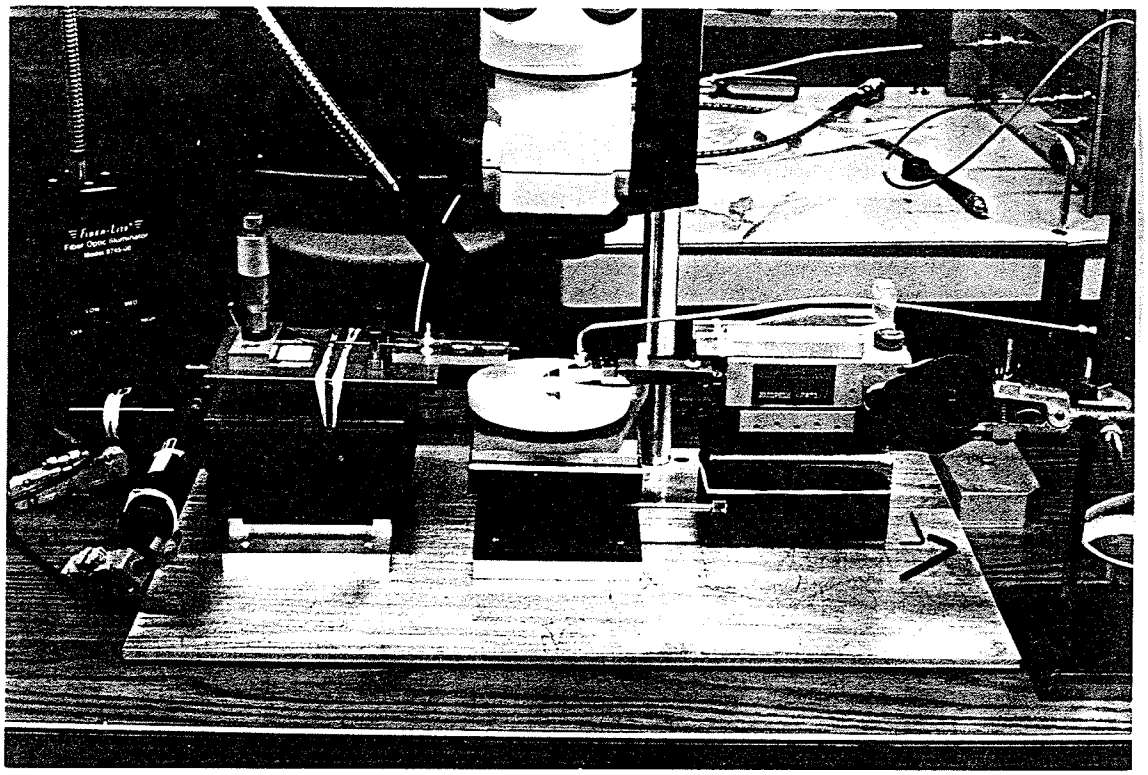

Figure 4.2. Plotter mounted with coaxial probe for mm resolution scans.

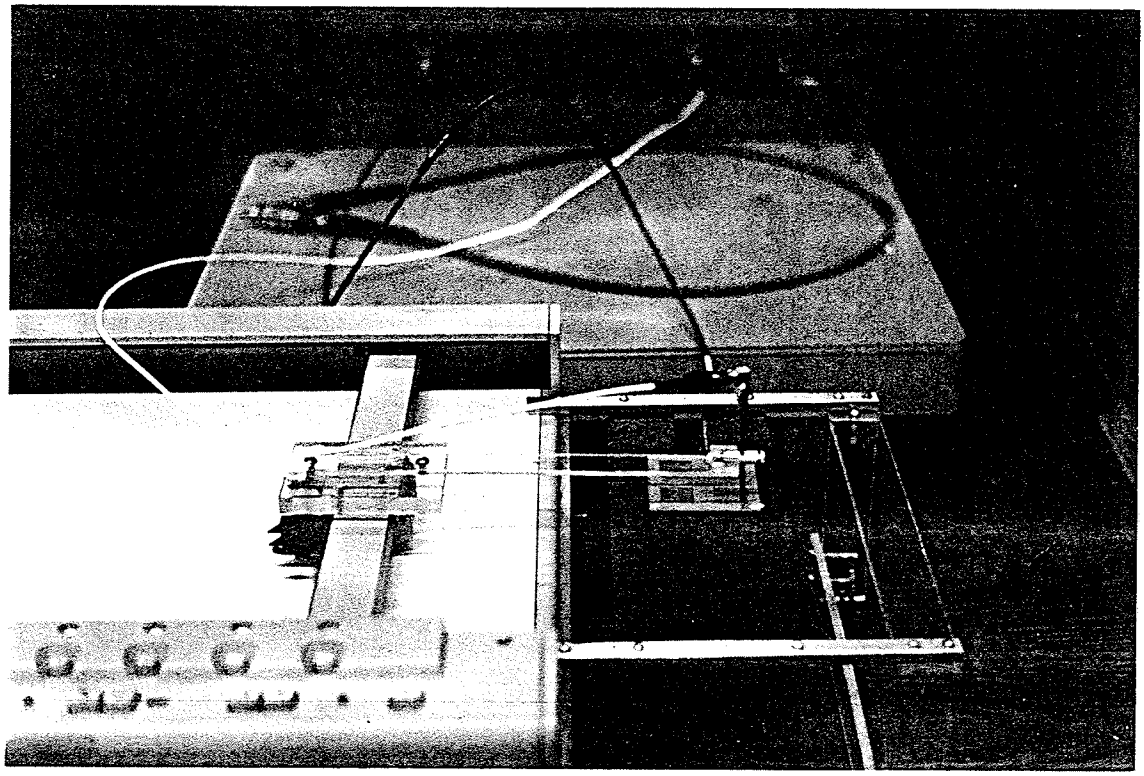

Figure 4.3a. Close up of DC motors used to scan μm circuits.

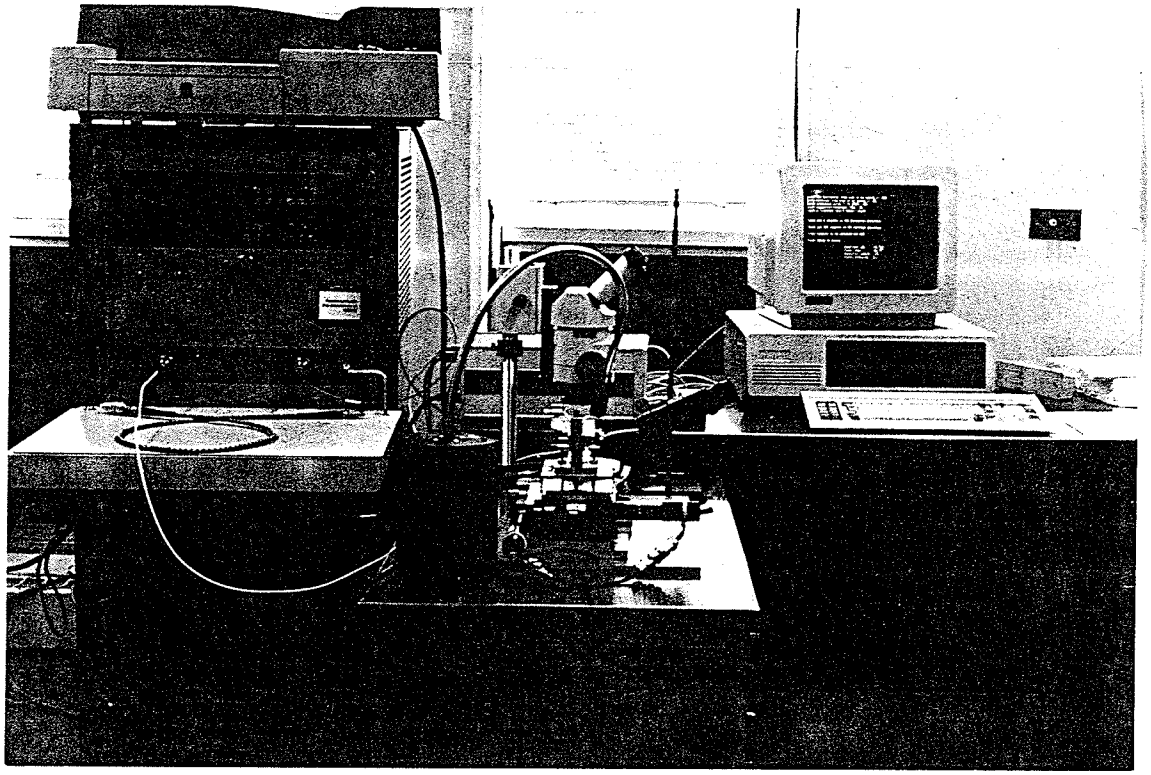

Figure 4.3b. Picture of apparatus required for automated data acquisition system.

## 4.2 Software Development

A series of programs have been developed for controlling probe maneuvering and data acquisition. This second generation of software is greatly improved over the first generation [17] which is not GPIB compatible and provided only magnitude data. The current software makes full use of the GPIB interface which allows for two way communication between the computer and network analyzer. All features of the network analyzer can be remotely controlled by the computer thereby increasing the flexibility and functionality of the data acquisitions system. The programs in the EMDAP (ElectroMagnetic Data Acquisition Program) library were written in Turbo Pascal on an IBM computer. A summary of the capabilities of each program is provided in table 4.1.

The non-GPIB compatibility column refers to whether or not the program is backwards compatible with systems requiring independent analog to digital converters such as the Dash-16 multifunction card. For more information on such a system the reader is referred to [17].

Table 4.1. Summary of software capabilities.

| | Compatibility | | Scans | | Resolution | | Multi-frequency |
|---|---|---|---|---|---|---|---|
| Program | GPIB | non-GPIB | 1D | 2D | mm | μm | |
| EMDAP1D | ✓ | ✓ | ✓ | | ✓ | ✓ | |
| EMDAP1DMF | ✓ | | ✓ | | ✓ | ✓ | ✓ |
| EMDAP2D | ✓ | ✓ | | ✓ | ✓ | ✓ | |

The EMDAP1DMF program is capable of collecting S-parameter data for multiple frequencies in a single scan. The test frequencies are specified by the user to be a sweep of frequencies at $\Delta f$ intervals or by simply entering the desired values. Note that this feature is not offered on non-GPIB systems. All software defaults to $S_{21}$ magnitude and phase readings. Other S-parameter measurements can be obtained by a simple software modification.

Incorporated into the the EMDAP software are the following features:

1) User definable start and end scan points.
2) User specified sampling intervals (mm or μm range).
3) Calibration procedure (non-GPIB systems only).
4) Automatic statistics and data filing (format compatible with Rplot and MBplot graphics software).

Software documentation is provided in appendix A. The hardware configuration is specified in appendix B.

# Chapter 5

## Dispersion and Impedance Analysis of Open-Microstrip

Transmission structures which are planar in nature are desirable for implementation in microwave integrated circuits (MIC's). The most popular type of planar transmission structure is microstrip. For higher frequencies coplanar waveguide is often used to reduce dimensions and coupling. Fabrication of the circuits can be done with the standard photolithography or photoetching techniques. Other attractive features of open-microstrip include the ability to add lumped (passive or active) elements, lightweight, conformable, simple transition to coax, and can be fabricated in MIC-hybrid or MMIC technologies. The work discussed in this chapter will concentrate on microstrip structures, but the general technique and analysis methods can be equally applied to coplanar structures.

Since microstrip is an open structure it is evident that the propagation of waves is supported by an inhomogeneous (air-dielectric) medium [23]. As a result microstrip cannot support a pure transverse electric magnetic (TEM, no electric or magnetic field component in the direction of propagation) mode. A proof that microstrip cannot support a pure TEM mode can be done by applying the appropriate boundary conditions to Maxwell's equation to show that both an electric and magnetic field component exist in the direction of propagation. Continuity of the tangential magnetic field component at the air$|_a$-dielectric$|_d$ interface shown in Fig. 5.1 requires that

$$\frac{j}{\omega\mu_o}\left(\frac{\partial E_z}{\partial y}-\frac{\partial E_y}{\partial z}\right)\Bigg|_d = \frac{j}{\omega\mu_o}\left(\frac{\partial E_z}{\partial y}-\frac{\partial E_y}{\partial z}\right)\Bigg|_a \tag{5.1}$$

which has been derived from obtaining the $H_x$ component of

$$\overline{H}=\frac{j}{\omega\mu}\left(\nabla\times\overline{E}\right). \tag{5.2}$$

The dielectric is assumed to be a perfect insulator ($\sigma$=0) with a relative permeability of $\mu_r$=1. By enforcing the continuity of the normal electric flux density at the interface (5.1) can be rewritten as

$$\left.\frac{\partial E_z}{\partial y}\right|_a - \left.\frac{\partial E_z}{\partial y}\right|_d = (\varepsilon_r - 1)\left.\frac{\partial E_y}{\partial z}\right|_d \tag{5.3}$$

Since $\varepsilon_r \neq 1$ and $E_y \neq 0$, the left hand side of (5.3) should be a non-zero quantity which can only be true if $E_z \neq 0$. Similarly, it can be shown that $H_z \neq 0$ by applying the boundary conditions that both the tangential electric field and normal magnetic flux density be continuous at the air-dielectric interface. Hence, for Maxwell's equations to hold for microstrip both the $H_z$ and $E_z$ field components must exist and a TEM mode cannot. These field components exist solely due to the fringing field components $E_x$ and $H_x$ at the air-dielectric interface. In addition, microstrip cannot support pure TM or TE waves. Essentially, the hybrid modes in microstrip are considered to be a superposition of both TM and TE waves.

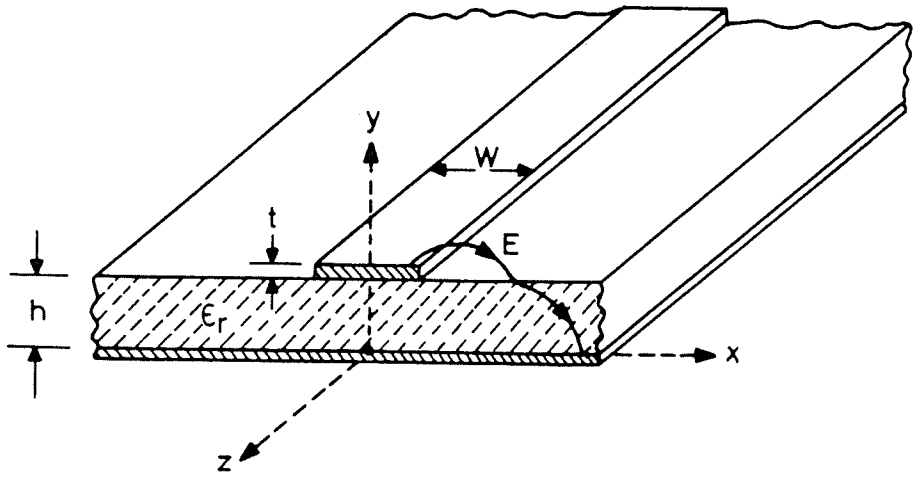


Figure 5.1. Microstrip configuration [23].

Wide spread use of microstrip has made the accurate characterization of microstrip parameters increasingly important. Several researchers have implemented both approximate and rigorous numerical techniques to calculate microstrip line characteristic impedances and phase velocities as a function of frequency (see Ref. [24] for an overview of several of these techniques). For typical structures while the phase velocity decreases

with an increase in frequency, the characteristic impedance increases. Though the physical phenomena actually responsible for this behavior in microstrip remains vague [25] it is often explained in terms of fringing fields. The approximate electric fringing fields shown in Fig. 5.2 indicate a hypothetical collimation of the fields beneath the microstrip line with frequency. Hence, an increase in the effective permittivity $\varepsilon_{re}$ (accounts for the wave propagating within an inhomogeneous medium) and corresponding decrease in the phase velocity. The increase in the characteristic impedance is a result of the apparent decrease of the lines effective width. Figure 5.3 outlines the three major groups of microstrip analysis for determining such parameters.

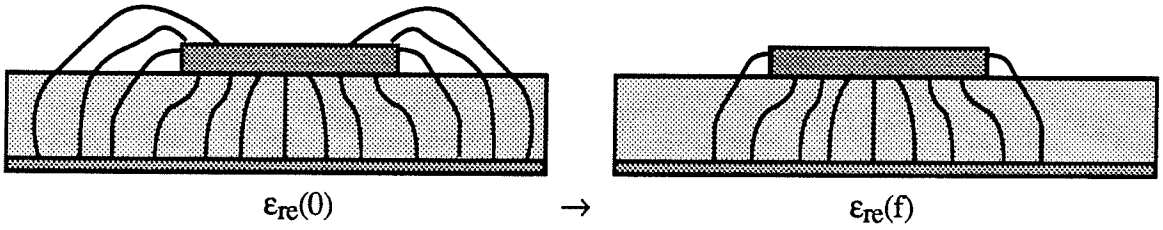


Figure 5.2. Fringing fields as a function of frequency.

The quasi-static approach assumes that the mode of propagation is pure TEM. This assumption is based on the fringing components at the air-dielectric interface being negligible when compared to the main field components within the dielectric. The microstrip characteristics are then derived from formulas which relate the electrostatic capacitances of the line with and without the dielectric substrate present. This analysis has proven to be adequate for frequencies where the strip width and substrate thickness are a small fraction of the guided wavelength.

The dispersion models account for the non-TEM nature of microstrip. This is done by determining the parameters of the model experimentally or theoretically and deriving a closed-form expression which correlates with the results. One of the drawbacks of this method is that generating the experimental results gives rise to a certain degree of uncertainty due to experimental error. In addition, the closed-form expression derived from the original set of data is an approximation in itself.

A full wave analysis is the most rigorous and time consuming of the 3 groups.

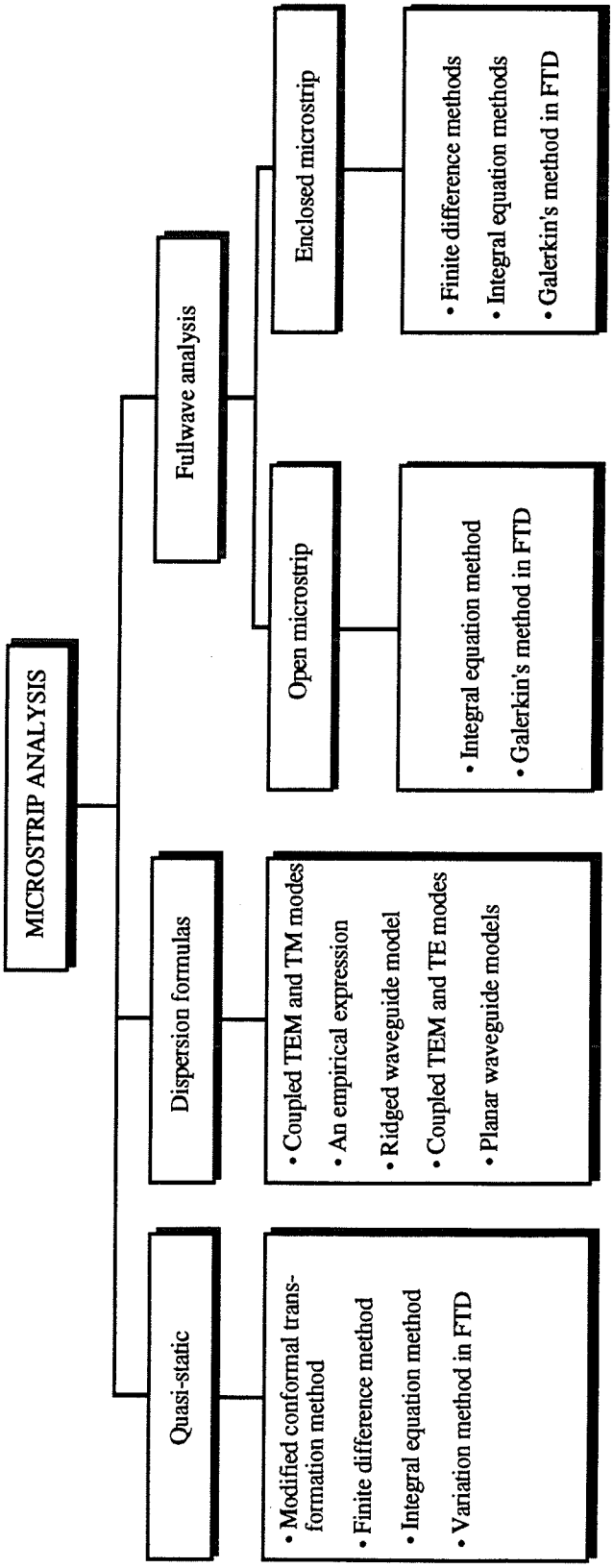


Figure 5.3. Various methods of microstrip analysis [23].

When confronted with using either a rigorous numerical technique (fullwave analysis) or an approximate solution (dispersion or quasi-static models) the microwave circuit designer must choose between involved and time consuming computer algorithms or relatively simple closed form expressions with limited ranges of validity and degrees of uncertainty. In all cases though reliable experimental data is required to verify the numerical approach or to determine the limitations of an approximate expression. Extraction of experimental data however, is expensive and time consuming while only limited experimental results are available in the literature for comparison with the various microstrip dispersion models. The next section describes the evolution of dispersion formulas $\varepsilon_{re}(f)$, with a discussion of $\varepsilon_{re}(0)$ formulas following in section 5.2.1.

## 5.1 Evolution of Dispersion Formulas

The development and constant improvement of closed-form dispersion formulas has been ongoing since the 1960's. Empirical relations were traditionally developed based on experimental, theoretical or a combination of both studies. The degree of accuracy claimed by the authors who derived these empirical relations is in doubt. One of the earliest formulas based on the results of both numerical and experimental studies was by Schneider [26] (see references within [26] for other early attempts at modeling dispersion). His formula was derived such that the following criteria was satisfied

a) The normalized phase velocity, $v_p$ (the ratio of the guided wavelength $\lambda_g$ to free-space wavelength $\lambda_o$) is a monotonically decreasing function of frequency.

b) $v_p$ and its first order derivative at f=0 are given by

$$v_p\Big|_{f=0} = \frac{1}{\sqrt{\varepsilon_{re}(0)}} \qquad \text{and} \qquad \frac{\partial v_p}{\partial f}\Big|_{f=0} = 0. \tag{5.4}$$

c) $v_p$ and its first order derivative for $f \to \infty$ are given by

$$v_p\Big|_{f\to\infty} = \frac{1}{\sqrt{\varepsilon_r}} \qquad \text{and} \qquad \frac{\partial v_p}{\partial f}\Big|_{f\to\infty} = 0. \tag{5.5}$$

d) The second derivative of $v_p$ is zero in the vicinity of the cut-off frequency ($f_c$) of the lowest order transverse electric ($TE_1$) surface wave mode propagating within a dielectric slab [27]

$$\left.\frac{\partial^2 v_p}{\partial f^2}\right|_{f=f_c} = 0 \qquad \text{where} \qquad f_c = \frac{3\times 10^8}{4h\sqrt{\varepsilon_r - 1}}. \tag{5.6}$$

Conditions (a) to (d) are satisfied by the equation

$$v_p = \frac{\lambda_g}{\lambda_o} = \frac{1}{\sqrt{\varepsilon_{re}(f)}} = \frac{1}{\sqrt{\varepsilon_r \varepsilon_{re}(0)}} \frac{\sqrt{\varepsilon_{re}(0)} f_n^2 + \sqrt{\varepsilon_r}}{f_n^2 + 1} \tag{5.7}$$

where the normalized frequency $f_n$ is defined as

$$f_n = \frac{f}{f_c} = \frac{4h\sqrt{\varepsilon_r - 1}}{\lambda_o}$$

with h being the height of the dielectric with relative permittivity $\varepsilon_r$ and $\lambda_o$ is the free-space wavelength. Computation of the static effective permittivity $\varepsilon_{re}(0)$ will be addressed in a subsequent section. Equation (5.7) was stated as having an error on the order of 3% when compared to various experimental and analytical results available at the time.

A year later Getsinger [28] introduced a new dispersion formula based on the dielectric-loaded ridged waveguide model. The Getsinger formula is

$$\varepsilon_{re}(f) = \varepsilon_r - \frac{\varepsilon_r - \varepsilon_{re}(0)}{1 + G\left(f/f_p\right)^2} \tag{5.8}$$

where

$$G = 0.6 + 0.009 Z_o$$
$$f_p = Z_o/(2\mu_o h).$$

$Z_o$ is the DC microstrip characteristic impedance and $\mu_o$ is the permeability of free space. From measurements of ring resonators on alumina (h=0.635 mm) Getsinger deduced the G-factor to be $G=0.6+0.009Z_o$.

As a result of a wide range of measurements on sapphire substrates Edwards and Owens [29] concluded that a new G-factor was required. Experimental results obtained from a linear resonator were curve fitted to determine the optimum G-factor to be

$$G = \sqrt{\frac{Z_o - 5}{60}} + 0.004Z_o . \tag{5.9a}$$

Hammersted and Jansen [30] were next to modify G as

$$G = \frac{\pi^2}{12}\frac{\varepsilon_r - 1}{\varepsilon_{re}(0)}\sqrt{\frac{Z_o}{60}} . \tag{5.9b}$$

Yet another modification to G was by Pramanick and Bhartia [25] who defined G as

$$G=\varepsilon_{re}(0)/\varepsilon_r . \tag{5.9c}$$

They also include a brief background discussion on previously derived dispersion formulas in their report.

Besides the aforementioned researchers there have been many others who have made contributions to the development and improvement of closed form dispersion formulas. In particular Yamashita [31], Kobayashi [32], and Kirschning-Jansen [33] are worth noting.

## 5.2 Summary of Dispersion Formulas

A set of dispersion formulas is now included for reference. The following list of formulas was adapted from Atwater [24] along with two additional formulas. In these expressions $\varepsilon_{re}(0)$ is the quasi-static value of $\varepsilon_{re}(f)$, $\varepsilon_r$ is the substrate relative dielectric constant, h is substrate height, w is the microstrip line width, $Z_0$ is the static characteristic impedance, $\mu_0$ is the permeability of free space, f is the frequency, and c the velocity of light. The conductor is assumed to have zero thickness. Calculation of $Z_0$ and $\varepsilon_{re}(0)$ are covered in section 5.2.1. The list is in chronological order:

1) M. V. Schneider, 1972 [26]:

$$\varepsilon_{re}(f) = \varepsilon_{re}(0)\left[\frac{1+f_n^2}{1+Kf_n^2}\right]^2 \tag{5.10}$$

where

$$K = \sqrt{\varepsilon_{re}(0)/\varepsilon_r}$$
$$f_n = (4hf/c)\sqrt{\varepsilon_r - 1}$$

2) W. J. Getsinger, 1973 [28]:

$$\varepsilon_{re}(f) = \varepsilon_{re}(0)\frac{1+Kf_n^2}{1+Gf_n^2} \tag{5.11}$$

where

$$G = 0.6 + 0.009Z_o$$
$$K = G \cdot \varepsilon_r / \varepsilon_{re}(0)$$
$$f_n = 2\mu_o hf / Z_o$$

3) Edwards and Owens, 1976 [29]:

$$\varepsilon_{re}(f) = \varepsilon_{re}(0)\frac{1+Kf_n^2}{1+Gf_n^2} \tag{5.12}$$

where

$$G = \sqrt{\frac{Z_o - 5}{60}} + 0.004Z_o$$
$$K = G \cdot \varepsilon_r / \varepsilon_{re}(0)$$
$$f_n = 2\mu_o hf / Z_o$$

4) E. Yamashita *et al.*, 1979 [31]:

$$\varepsilon_{re}(f) = \varepsilon_{re}(0)\left[\frac{1+Kf_n^{1.5}}{1+f_n^{1.5}}\right]^2 \tag{5.13}$$

where

$$K = \sqrt{\varepsilon_r / \varepsilon_{re}(0)}$$
$$f_n = \left(4^{1/3} hf/c\right)\sqrt{\varepsilon_r - 1}\left\{\frac{1}{2} + \left[1 + 2\log_{10}\left(1 + \frac{w}{h}\right)\right]^2\right\}$$

5) Hammarstad-Jensen, 1980 [30]:

$$\varepsilon_{re}(f) = \varepsilon_{re}(0)\frac{1+Kf_n^2}{1+Gf_n^2} \tag{5.14}$$

where

$$G = \frac{\pi^2}{12}\frac{\varepsilon_r - 1}{\varepsilon_{re}(0)}\sqrt{\frac{Z_o}{60}}$$
$$K = G \cdot \varepsilon_r / \varepsilon_{re}(0)$$
$$f_n = 2\mu_o h f / Z_o$$

6) Kirschning-Jansen, 1982 [33]:

$$\varepsilon_{re}(f) = \varepsilon_{re}(0)\frac{1+KP}{1+P} \tag{5.15}$$

where

$$K = \varepsilon_r / \varepsilon_{re}(0)$$
$$P = P_1 P_2 \left[(0.1844 + P_3 P_4)10F_4\right]^{1.5763}$$
$$P_1 = 0.27488 + \left[0.6315 + 0.525/(1+0.157F_4)^{20}\right]\cdot\left(\frac{w}{h}\right) - 0.065683\exp(-8.7513\,w/h)$$
$$P_2 = 0.33622\left[1 - \exp(-0.03442\varepsilon_r)\right]$$
$$P_3 = 0.0363\exp(-4.6\,w/h)\left\{1 - \exp\left[-(F_4/3.87)^{4.97}\right]\right\}$$
$$P_4 = 1 + 2.751\left\{1 - \exp\left[-(\varepsilon_r/15.916)^8\right]\right\}$$
$$F_4 = f \cdot h \qquad \text{in units of GHz - cm}$$

7) M. Kobayashi, 1982 [34]:

$$\varepsilon_{re}(f) = \varepsilon_{re}(0)\left[\frac{1+f_n^2}{1+Kf_n^2}\right]^2 \tag{5.16}$$

where

$$K = \sqrt{\varepsilon_{re}(0)/\varepsilon_r}$$
$$f_n = (2\pi h f/c)(1 + w/h)\sqrt{\varepsilon_r - \varepsilon_{re}(0)}/D$$
$$D = \mathrm{Tan}^{-1}\left(\varepsilon_r\sqrt{\frac{\varepsilon_{re}(0)-1}{\varepsilon_r - \varepsilon_{re}(0)}}\right)$$

8) Pramanick-Bhartia, 1983 [25]:

$$\varepsilon_{re}(f) = \varepsilon_{re}(0)\frac{1+f_n^2}{1+Kf_n^2} \tag{5.17}$$

where

$$K = \varepsilon_{re}(0)/\varepsilon_r$$
$$f_n = 2\mu_o hf/Z_o$$

9) M. Kobayashi, 1988 [32]:

$$\varepsilon_{re}(f) = \varepsilon_r - \frac{\varepsilon_r - \varepsilon_{re}(0)}{1+(f/f_{n1})^m} \tag{5.18}$$

where

$$f_{n1} = \frac{f_{n2}}{0.75+\left(0.75-\frac{0.332}{\varepsilon_r^{1.73}}\right)\frac{w}{h}}$$

$$f_{n2} = \frac{cTan^{-1}\left\{\varepsilon_r\sqrt{\frac{\varepsilon_{re}(0)-1}{\varepsilon_r-\varepsilon_{re}(0)}}\right\}}{2\pi h\sqrt{\varepsilon_r-\varepsilon_{re}(0)}}$$

and

$$m = m_o m_c \quad ; m \le 2.32$$

$$m_o = 1+\frac{1}{1+\sqrt{w/h}}+0.32\left(\frac{1}{1+\sqrt{w/h}}\right)^3$$

$$m_c = \begin{cases} 1+\frac{1.4}{1+w/h}\left\{0.15-0.235\exp\left(\frac{-0.45f}{f_{n1}}\right)\right\} & ; w/h \le 0.7 \\ 1 & ; w/h \ge 0.7 \end{cases}$$

Atwater [24] has tested all of the formulas except (5.12) and (5.18) relative to a collection of 120 measured values obtained from the literature. He found the root mean square (RMS) deviation of the predicted from the measured values to range from 2.3% [33] to 4.1% [26]. The formula developed by Kobayashi [32] is believed to be the most

accurate as he claims an accuracy better than 0.6% in the range $0.1<w\leq 10$, $1<\varepsilon_r\leq 128$, and any $h/\lambda_o$ when compared to a rigorous numerical solution [35].

### 5.2.1 Calculating $\varepsilon_{re}(0)$ and $Z_o$

In order to calculate $\varepsilon_{re}(f)$ using equations (5.10) to (5.18) the static effective permittivity $\varepsilon_{re}(0)$ must be calculated. Assuming that the conductor thickness is zero it is possible to evaluate $\varepsilon_{re}(0)$ with the following [23].

$$\varepsilon_{re}(0) = \frac{\varepsilon_r + 1}{2} + \frac{\varepsilon_r - 1}{2} \cdot F(w/h) \tag{5.19}$$

where

$$F(w/h) = \begin{cases} (1+12\,h/w) + 0.04(1-w/h)^2 & ;w/h \leq 1 \\ (1+12\,h/w)^{-1/2} & ;w/h \geq 1 \end{cases}$$

The characteristic impedance $Z_o$ can be computed from

$$Z_o = \begin{cases} \dfrac{60}{\sqrt{\varepsilon_{re}(0)}} \ln\left(\dfrac{8h}{w} + \dfrac{w}{4h}\right) & ;w/h \leq 1 \\ \dfrac{120\pi}{\sqrt{\varepsilon_{re}(0)}\left[\dfrac{w}{h} + 1.393 + 0.667 \ln\left(\dfrac{w}{h} + 1.444\right)\right]^{-1}} & ;w/h \geq 1 \end{cases} \tag{5.20}$$

with a maximum relative error in $\varepsilon_{re}(0)$ and $Z_o$ of less than 2%. Alternatively, Kobayashi [36] has produced table 5.1 using a Green's function technique. Obtaining the effective filling fraction $q_w$ from table 5.1, the effective relative permittivity is obtained from

$$\varepsilon_{re}(0) = 1 + q_w(\varepsilon_r - 1). \tag{5.21}$$

The characteristic impedance is given by

$$Z_o = \frac{\sqrt{\mu_o/\varepsilon_o}}{C_o/\varepsilon_o \sqrt{\varepsilon_{re}(0)}} \tag{5.22}$$

where $C_o/\varepsilon_o$ is the microstrip line capacitance per unit length without the dielectric ($\varepsilon_r=1$) and is given in table 5.1. Values not directly available in table 5.1 can be determined to a high degree of accuracy from interpolation. The parameters can also be computed from an

approximate formula [37]. The accuracy using this method is claimed to be much less than 1% for $\varepsilon_{re}(0)$ and $Z_o$.

Table 5.1. Line capacitance per unit length $C_o/\varepsilon_0$ and effective filling fraction $q_w$ of microstrip with isotropic substrate [36].

| $\varepsilon_1^*$ / w/h | $C_o/\varepsilon_0$ | Effective filling fraction $q_w$ | | | | | | |
|---|---|---|---|---|---|---|---|---|
| | 1 | 1.01 | 1.5 | 2 | 4 | 8 | 16 | 128 |
| 0.01 | 0.939969 | 0.551680 | 0.547367 | 0.544902 | 0.540740 | 0.538629* | 0.537441* | 0.536800# |
| 0.04 | 1.18587 | 0.565312 | 0.560106 | 0.557151 | 0.552236 | 0.549502 | 0.547960 | 0.546771* |
| 0.10 | 1.43375 | 0.578900 | 0.573016 | 0.569632 | 0.563975 | 0.560825 | 0.559150 | 0.557641* |
| 0.20 | 1.70270 | 0.593607 | 0.587092 | 0.583321 | 0.576983 | 0.573437 | 0.571548 | 0.569699 |
| 0.40 | 2.09393 | 0.614680 | 0.607485 | 0.603295 | 0.596207 | 0.592215 | 0.590082 | 0.587837 |
| 0.70 | 2.56365 | 0.638960 | 0.631299 | 0.626811 | 0.619174 | 0.614845 | 0.612523 | 0.610393 |
| 1.00 | 2.97991 | 0.659094 | 0.651269 | 0.646668 | 0.638808 | 0.634334 | 0.631929 | 0.629708 |
| 2.00 | 4.23158 | 0.710090 | 0.702537 | 0.698071 | 0.690398 | 0.686004 | 0.683634 | 0.681456 |
| 4.00 | 6.52698 | 0.772544 | 0.766173 | 0.762402 | 0.755913 | 0.752192 | 0.750183 | 0.748329 |
| 7.00 | 9.79686 | 0.823842 | 0.818821 | 0.815854 | 0.810758 | 0.807840 | 0.806266 | 0.804816 |
| 10.00 | 12.9814 | 0.854113 | 0.849977 | 0.847538 | 0.843356 | 0.840967 | 0.839679 | 0.838494 |
| 20.00 | 23.3628 | 0.903768 | 0.901149 | 0.899611 | 0.896985 | 0.895491 | 0.894687 | 0.893950 |
| 40.00 | 43.7668 | 0.939854 | 0.938327 | 0.937433 | 0.935914 | 0.935054 | 0.934591 | 0.934168 |
| 100.00 | 104.323 | 0.969596 | 0.968909 | 0.968082 | 0.967830 | 0.967447 | 0.967242 | 0.967055 |

$\varepsilon_{1x}^* = \varepsilon_{1y}^* = \varepsilon_1^*$, $\varepsilon_{2x}^* = \varepsilon_{2y}^* = 1$, m = 40, N = 50(N = 1, 100, 600 for $\varepsilon_1^*$ = 1, 16, 128, respectively), Y = 3(Y = 1 for # and Y = 2 for *),

$q_w = (\varepsilon_{eff}^*-1)/(\varepsilon_1^*-1)$, $\varepsilon_{eff}^* = (C/\varepsilon_0)/(C_0/\varepsilon_0)$

For cases in which the conductor thickness is small (t/h≤0.005), the agreement between theoretical and experimental results is excellent [38]. However, there are many instances where the conductor thickness must be taken into account. A set of design equations which are accurate to within 2% for $Z_o$ and $\sqrt{\varepsilon_{re}(0)}$ for the parameters t/h≤0.2, 0.1≤w/h≤20, and $\varepsilon_r$≤16 are available. The closed form expressions for $\varepsilon_{re}(0)$ and $Z_o$ are given in [39] as

$$\varepsilon_{re}(0) = \begin{cases} \dfrac{\varepsilon_r+1}{2} + \dfrac{\varepsilon_r-1}{2}\left[\left(1+\dfrac{12}{w/h}\right)^{-1/2} + 0.04\left(1-\dfrac{w}{h}\right)^2\right] - \dfrac{\varepsilon_r-1}{4.6}\dfrac{t/h}{\sqrt{w/h}} & ;w/h \le 1 \\ \dfrac{\varepsilon_r+1}{2} + \dfrac{\varepsilon_r-1}{2}\left(1+\dfrac{12}{w/h}\right)^{-1/2} - \dfrac{\varepsilon_r-1}{4.6}\dfrac{t/h}{\sqrt{w/h}} & ;w/h \ge 1 \end{cases} \tag{5.23}$$

$$Z_o = \begin{cases} \dfrac{60}{\sqrt{\varepsilon_{re}(0)}} \ln\left(\dfrac{8h}{w_e} + \dfrac{w_e}{4h}\right) & ;w/h \le 1 \\ \dfrac{120\pi}{\sqrt{\varepsilon_{re}(0)}}\left[\dfrac{w_e}{h} + 1.393 + 0.667\ln\left(\dfrac{w_e}{h}+1.444\right)\right]^{-1} & ;w/h \ge 1 \end{cases} \tag{5.24}$$

where

$$\frac{w_e}{h} = \begin{cases} \frac{w}{h} + \frac{1.25}{\pi}\frac{t}{h}\left(1 + \ln\frac{4\pi w}{t}\right) & ; w/h \le \frac{1}{2\pi} \\ \frac{w}{h} + \frac{1.25}{\pi}\frac{t}{h}\left(1 + \ln\frac{2h}{t}\right) & ; w/h \ge \frac{1}{2\pi} \end{cases}$$

It is evident from (5.23) that $\varepsilon_{re}(0)$ decreases as a result of an increase in the conductor thickness t. This phenomena can be explained by the fraction of total energy propagating in the air increasing with t.

The change in $Z_0$ is influenced by two factors. First we consider that fringing fields from the edges would tend to increase the effective width of the transmission line. This in effect will increase the capacitance of the line and thereby attempt to decrease $Z_0$ since $Z_0=\sqrt{L/C}$. The second factor is the decrease in $\varepsilon_{re}(0)$ which attempts to increase $Z_0$. The net result turns out to be a decrease in $Z_0$ with t/h. This has been confirmed by both theoretical analysis and experimental measurements (see Ref. [39] and references therein).

To illustrate the diversity of the dispersion formulas (5.10) through (5.18) a sample graph is provided in Fig. 5.4. The parameters are w/h=1, h=0.125", $Z_0$=47.8, t=0, and $\varepsilon_r$=10.5. Figure 5.5 shows the effect of dispersion for various w/h values and the change in wavelength.

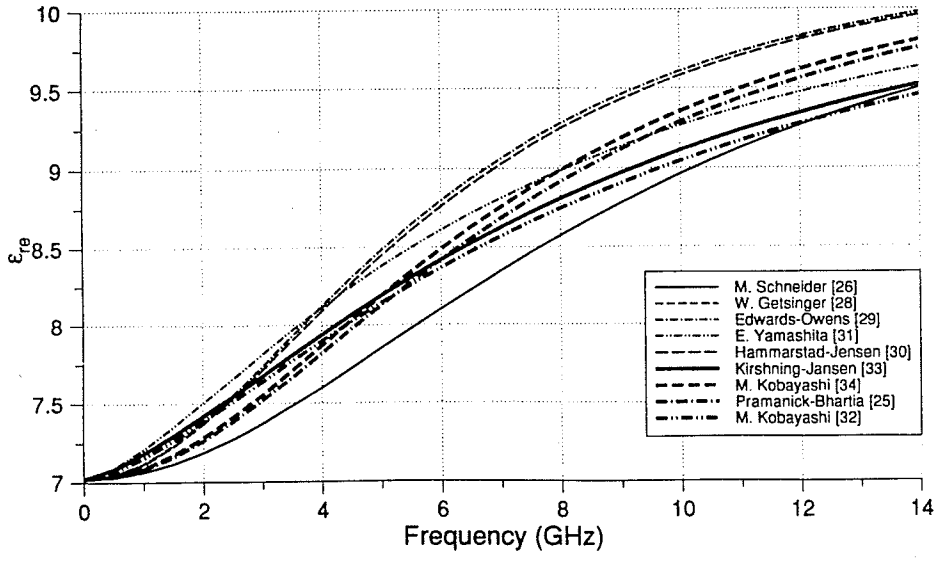


Figure 5.4. Example of dispersion curves with $\varepsilon_{re}(0)$ calculated using table 5.1 and $Z_0$ from (5.22).

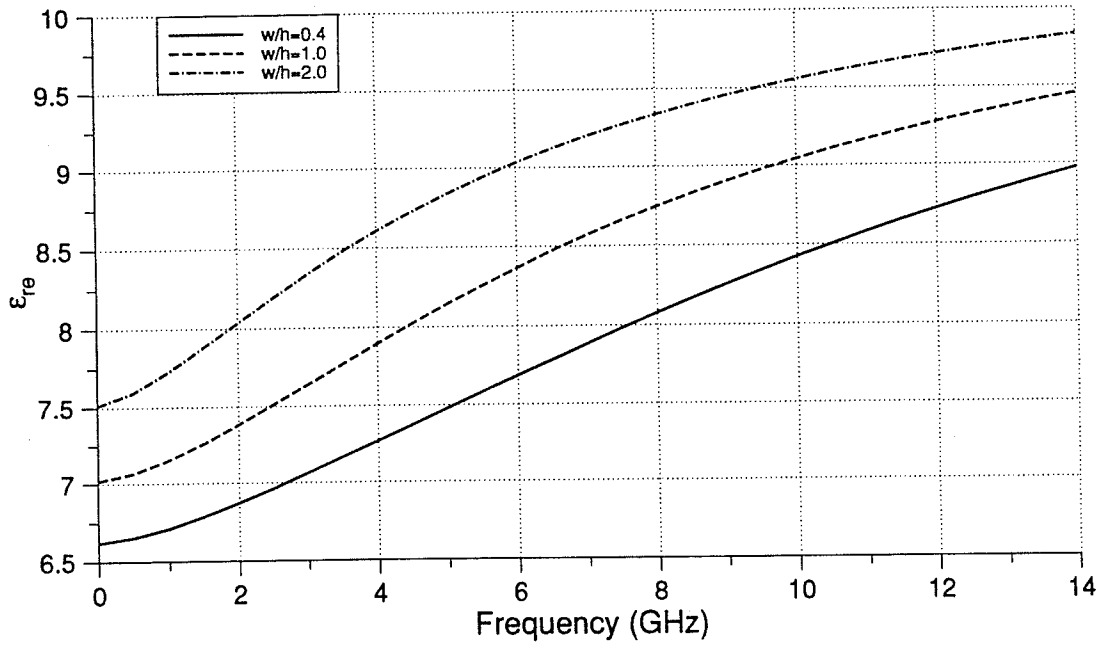


Figure 5.5a. Dispersion formula [32] calculated for 3 different w/h values.

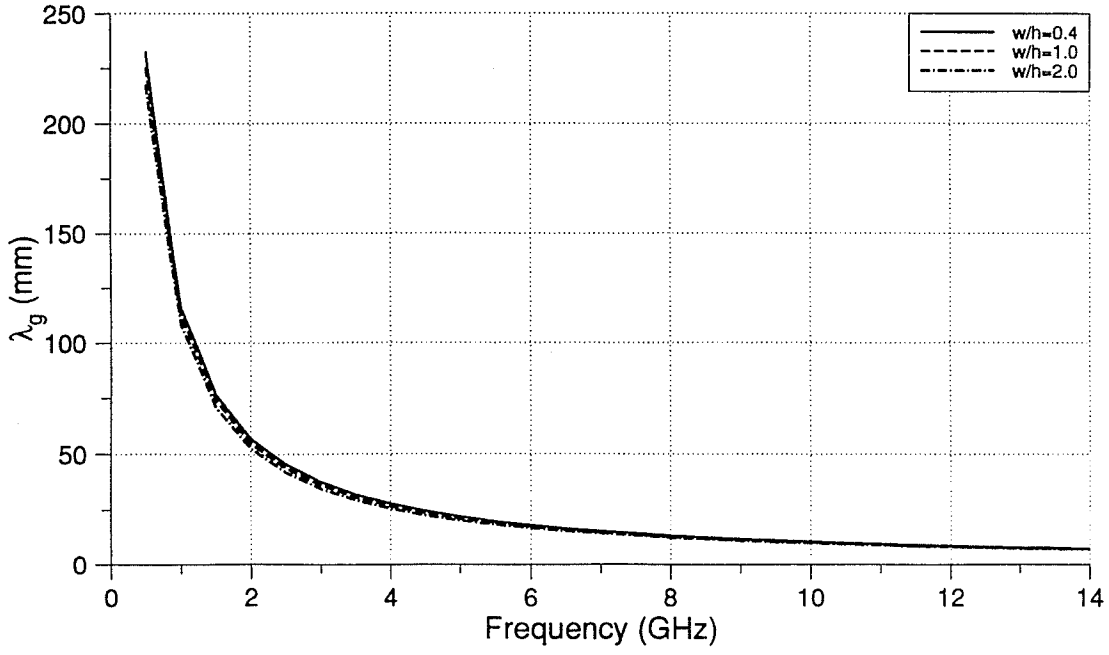


Figure 5.5b. Calculated wavelength calculated for 3 different w/h values.

## 5.3 Dispersion Properties of Higher Order Modes

Discussion up to this point has been focused on the dispersion characteristics of the quasi-TEM mode in open microstrip. However, there are instances where the propagation of higher order discrete modes may be of concern to the designer. Conventional theoretical analysis does not account for the propagation of higher order hybrid modes.

It has been shown that the higher order modes of open-microstrip can be approximated by a planar waveguide model [40]. In Fig. 5.6 the microstrip line has been replaced by an approximate equivalent model. The model consists of a parallel plate waveguide of width $w_e(f)$ and and height h. The waveguide is bound by ideal electric walls at the top and bottom and magnetic walls on the sides. The waveguide dielectric is assumed to have an effective permittivity $\varepsilon_{re*}(f)$ (analogous to the quasi-TEM $\varepsilon_{re}(f)$). While the frequency dependant $\varepsilon_{re*}$ describes the influence of the dispersion on the phase velocity, the frequency dependant effective width $w_e$ describes the influence on the characteristic impedance.

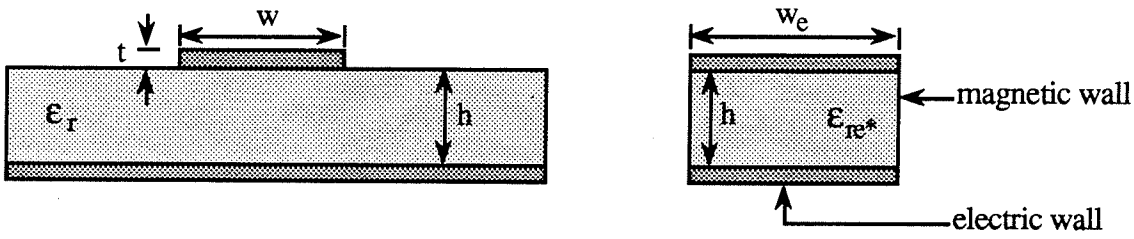


Figure 5.6 Planar waveguide model [40].

An empirical relation which gives the effective strip width as a function of frequency is given in [40] as

$$w_e(f) = w + \frac{w_e(0) - w}{1 + f/f_g} \tag{5.25}$$

where

$$f_g = c/2w\sqrt{\varepsilon_r}$$

$w_e(0)$ = effective width calculated from quasi - static analysis

$$= 120\pi h \Big/ \left(Z_0\sqrt{\varepsilon_{re*}(0)}\right)$$

and $Z_0$ is calculated using one of the previously mentioned formulas. The cutoff frequency of the mth higher order mode can be calculated from

$$f_c(m) = \frac{mc}{2w_e(f)\sqrt{\varepsilon_{re*}(f)}}. \tag{5.26}$$

The guided wavelength as illustrated in Fig. 5.7 is then obtained from

$$\lambda_{HE_m} = \frac{\lambda_0}{\sqrt{\varepsilon_{re*}(f)}\sqrt{1-[f_c(m)/f]^2}}. \tag{5.27}$$

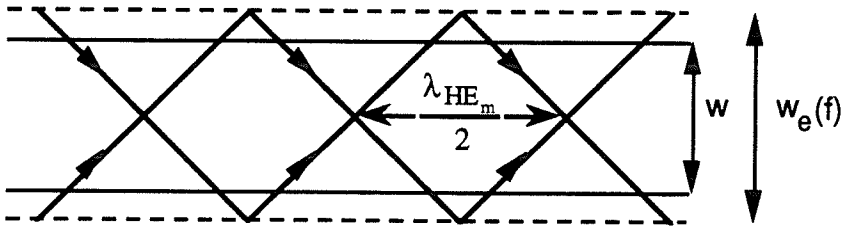


Figure 5.7. Guided wavelength diagram taking into account $w_e(f)$.

Using the frequency dependant width given by (5.25), it can be shown that the influence of the frequency dependant $\varepsilon_{re*}(f)$ on the transmission line characteristics is small. Therefore the numerical effort required to compute $\varepsilon_{re*}(f)$ can be avoided by using the simple approximation of $\varepsilon_{re*}(f)=\varepsilon_r$ as a first order approximation. This is predominantly a result of the higher order modes being concentrated within the dielectric and assuming negligible fringing fields.

As an example Fig. 5.8 is a plot of the squared normalized wave number of the fundamental and first two higher order modes (quasi-TEM or $HE_0$, $HE_1$, and $HE_2$) for a microstrip line with w=30 mm, h=1/16", $\varepsilon_r$=2.5, and $Z_0$=11 Ω. To obtain the cutoff frequencies for $HE_1$ and $HE_2$ (5.25) was substituted into (5.26) and an iterating procedure [41] was used to solve for $f_c$.

To obtain an insight on the characteristics of the modes in microstrip, the approximate electric field distribution of the dominant and the first two higher order modes are shown in Fig. 5.9a. The longitudinal current distributions are shown in Fig. 5.9b.

Experimental data was obtained for a wide microstrip line (w=30 mm, h=1/16", $\varepsilon_r$=2.5, and $Z_o$=11 Ω) at frequencies of 2.5, 4.5, 8.5 GHz. As can be seen in Fig 5.8 these frequencies are below $HE_1$ cutoff, above $HE_1$ cutoff but below $HE_2$ cutoff, and above $HE_2$ cutoff, respectively. A coaxial probe with $D_o$=0.0865" and tip length t=1.5 mm was used for all measurements. Two sets of measurements were taken with the source at the plane of symmetry and then slightly off the plane of symmetry. With the feed slightly off the plane of symmetry it is possible to excite the $HE_1$ mode. The reason being that the current is zero along the plane of symmetry (Fig. 5.9b).

The experimental results of the 2D scans are given in Figs. 5.10a,b. Two cross sections of the data in Figs. 5.10b are given in Figs. 5.11a,b which are indicative of the quasi-TEM and $HE_1$ modes. Inspection of the experimental results shows that the measurement drops off rapidly when the probe scans beyond edge of the conductor. This is due to the electric field being highly tangential (see Fig. 5.1) to the center conductor of the probe.

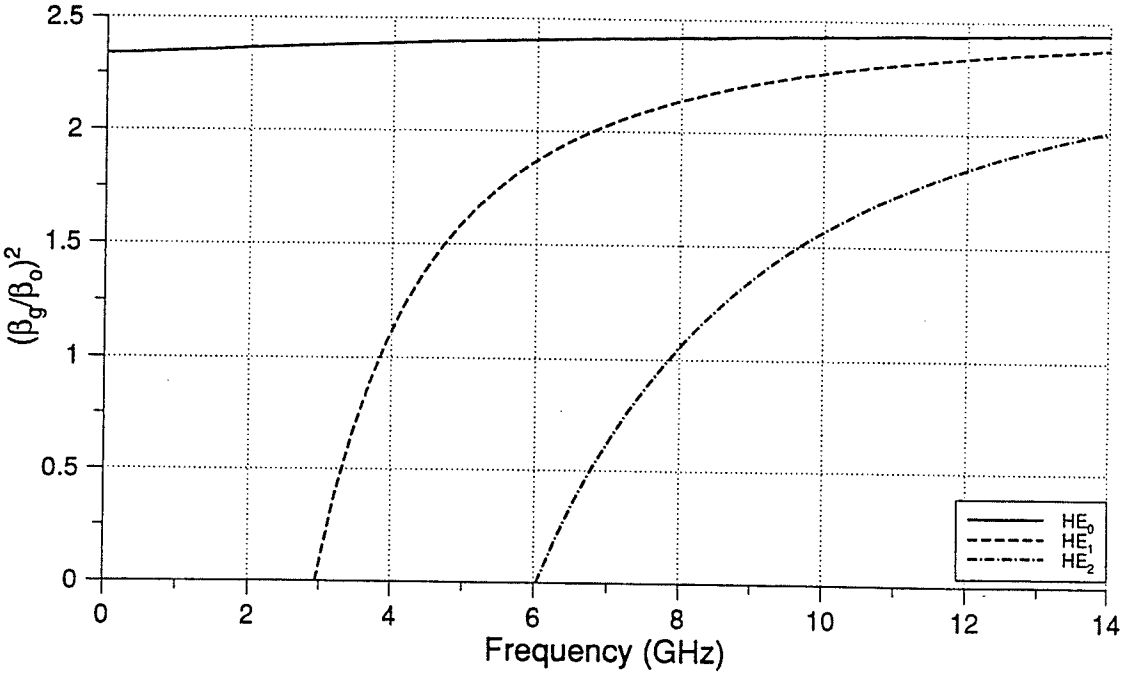


Figure 5.8. Dispersion characteristics of first 2 higher order modes. Quasi-TEM dispersion curve calculated using [32].

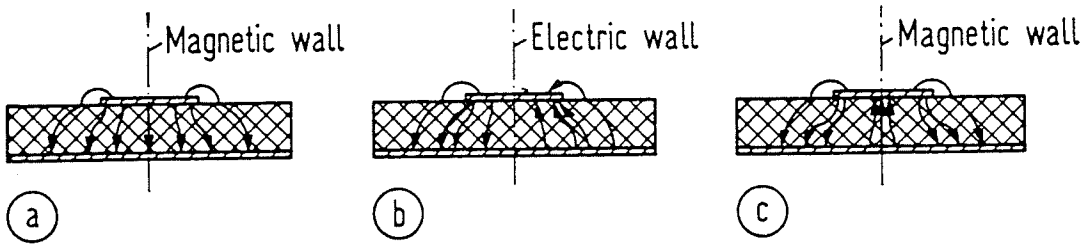


Figure 5.9a. Approximate electric field distribution of the lowest and the first two higher-order modes on a microstrip line; (a) $HE_0$ or quasi-TEM, (b) $HE_1$ mode, (c) $HE_2$ mode [42].

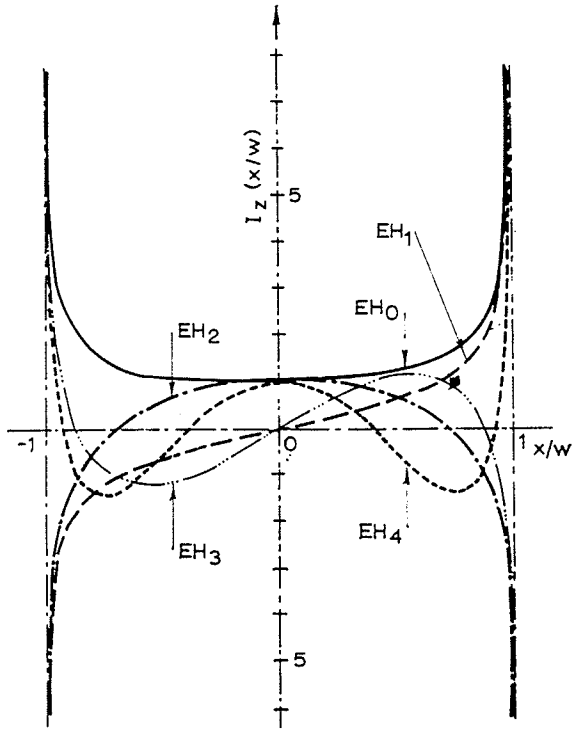


Figure 5.9b. Longitudinal current distribution functions for the $HE_0$, $HE_1$, $HE_2$, $HE_3$, and $HE_4$ modes [43].

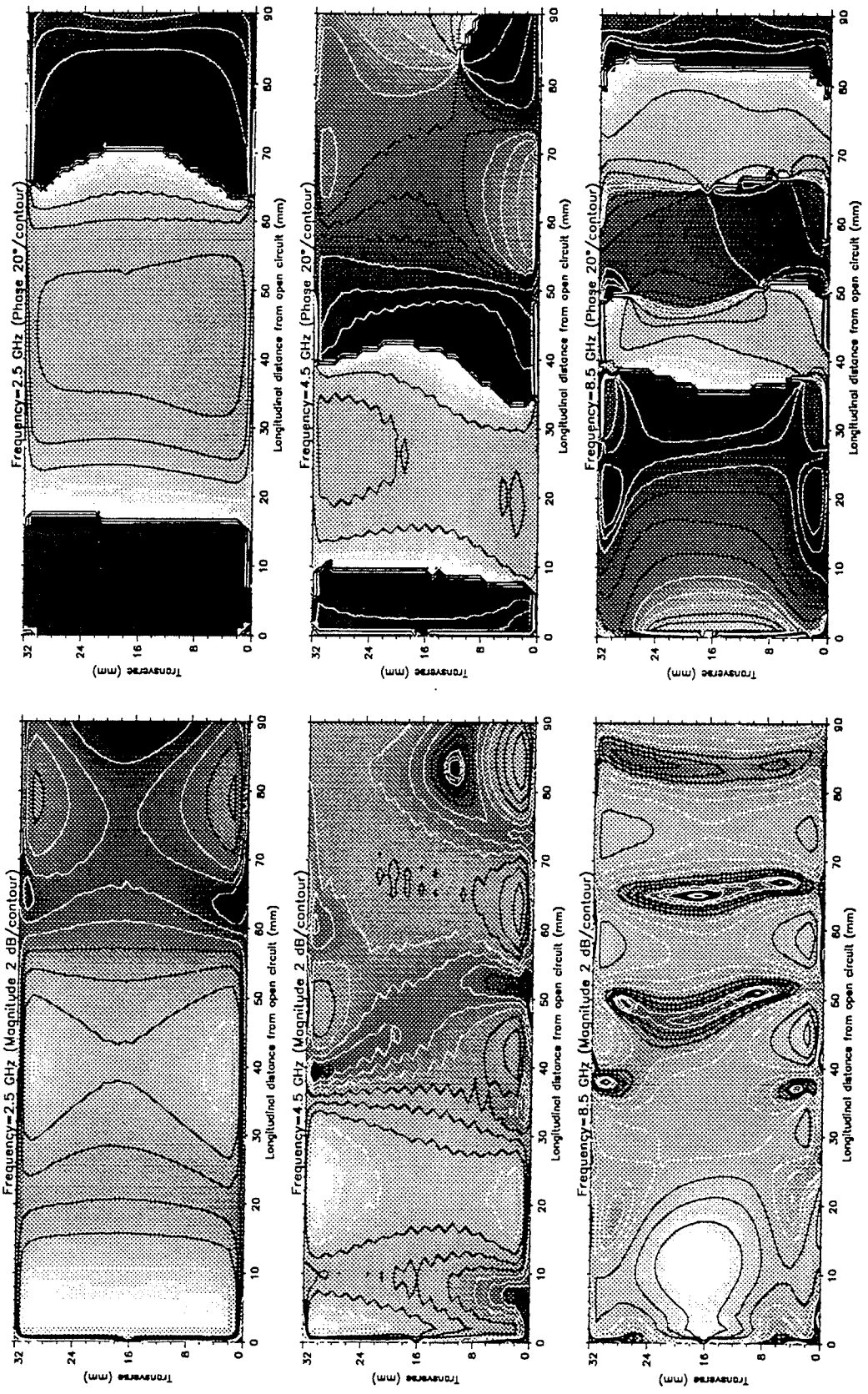


Figure 5.10a. Magnitude and phase variation of the charge distribution on a wide microstrip line at 2.5, 4.5, and 8.5 GHz. Source located at the plane of symmetry.

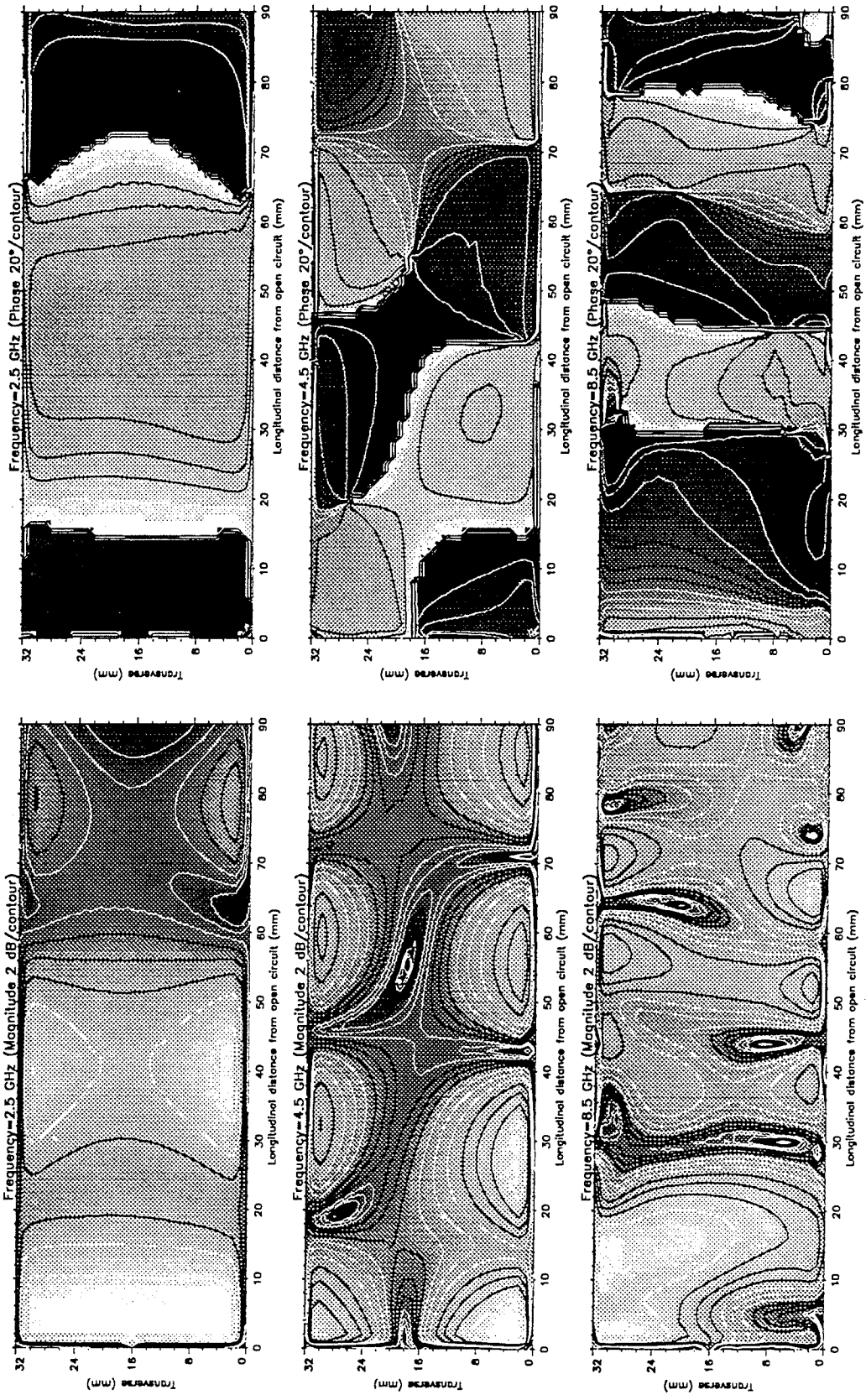


Figure 5.10b. Magnitude and phase variation of the charge distribution on a wide microstrip line at 2.5, 4.5, and 8.5 GHz. Source located off the plane of symmetry.

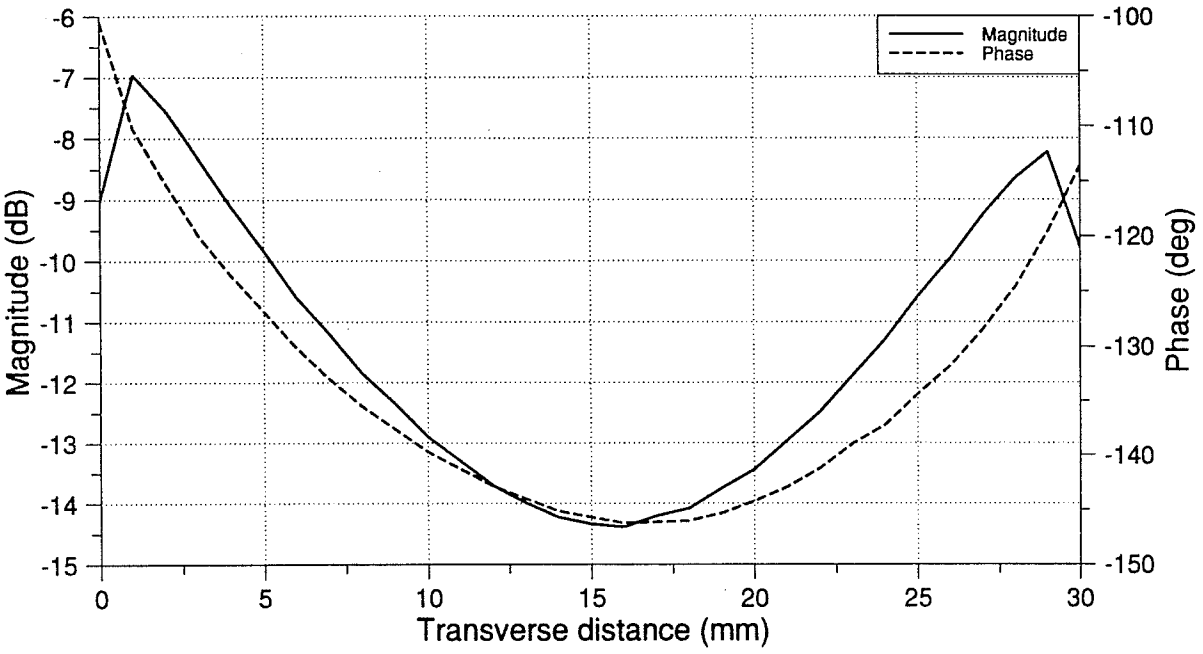


Figure 5.11a. Transverse scan of the wide microstrip line at f=2.5 GHz at a distance of 80 mm from the open circuit indicating the quasi-TEM mode. Off center feed case.

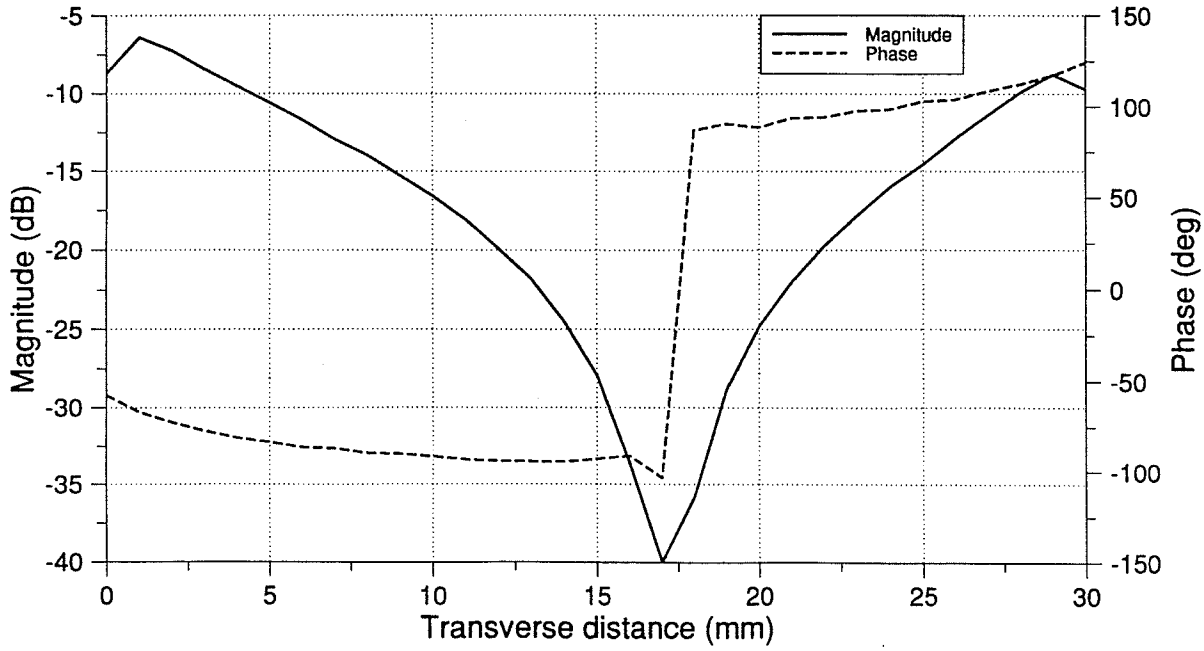


Figure 5.11b. Transverse scan of the wide microstrip line at f=4.5 GHz at a distance of 55 mm from the open circuit indicating the $HE_1$ mode. Off center feed case.

# Chapter 6

## Experimental Methods for Determining the Dispersion Characteristics of Open-Microstrip

Though the advancement of numerical techniques is continuously ongoing, the development of alternative experimental techniques for dispersion measurements has received little attention. This is becoming especially important in MMIC technology where dimensions are small and non-invasive coupling to the substrate is difficult. A summary of currently available dispersion measurement techniques for obtaining the effective permittivity $\varepsilon_{re}$ is provided in Fig. 6.1.

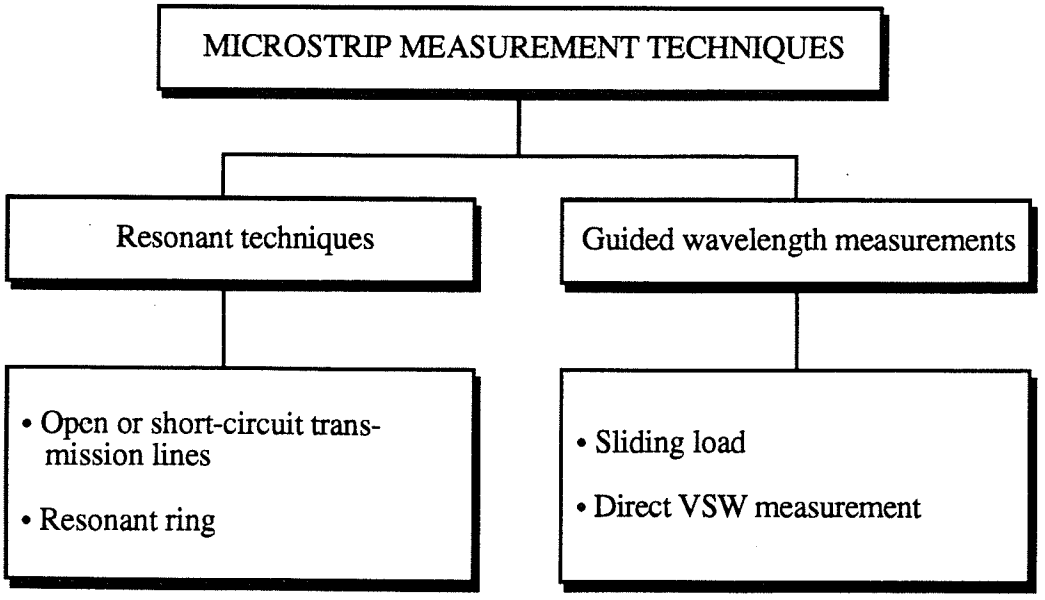


Figure 6.1. Various dispersion measurement techniques.

Typical experimental methods utilize resonant structures such as open and short-circuited transmission lines [44] or gap coupled ring resonators [45] to measure dispersion properties. The former of these methods suffers from frequency dependent effects at the open or short terminations of the transmission line. While the ring resonator eliminates this problem a large diameter ring maybe necessary to reduce mutual coupling and radiation effects. Resonant techniques determine dispersion characteristics at a set of discrete frequencies. In contrast to resonant techniques, a sliding load method [42] has been used to measure the wavelength on the microstrip line directly. This is accomplished by sliding some type of load, such as a surface absorber, along the transmission line and measuring the variation of the input reflection coefficient, which is $\lambda/2$ periodic. With this technique, the applied load must remain consistent as its position is varied along the length of the line under test.

The alternative method presented in this chapter for measuring dispersion is through the direct measurement of the voltage standing wave on an unmatched microstrip transmission line [46]. With this technique, the VSW on an unmatched transmission line is determined by scanning a near field probe along the microstrip transmission line [16]. The guided wavelength and thus $\varepsilon_{re}(f)$ is obtained by measuring the distance between successive voltage minimums in which a 180° phase shift occurs. This method is non-invasive and transmission line termination effects do not effect the calculated $\varepsilon_{re}(f)$. In addition, the existence of higher order discrete modes can be directly determined. The excitation of such modes is often due to circuit discontinuities.

## 6.1 Experimental Test Cases

Several test cases will be measured and compared with the existing theoretical dispersion formulas presented in chapter 5. The substrate utilized for the experiment was RT/duriod 6010 with relative permittivity $\varepsilon_r$=10.2±0.25, dielectric height h=0.075" ±0.004", and copper thickness t=0.0028"±10% (substrate A). Another substrate of the same series and tolerances with parameters $\varepsilon_r$=10.5, h=0.125", and t=0.0007" (substrate B) was also tested.

For experimental testing three transmission lines and a ring resonator were fabricated on substrate A. The three lines were 150 mm long with widths of 1.0, 1.8, and 4.55 mm corresponding to $Z_o$=61.4, 48.3, and 29.0 Ω, respectively. Spacing between the lines and the edge of the substrate was roughly 30 mm. The length of the lines were chosen such

that at the lowest test frequency they were at least $\lambda/2$ long. The ring resonator fabricated had a line width of 1.8 mm and mean radius of 36.1 mm. On substrate B a 150 mm long line of width 2.8 mm (50.2 Ω) and a ring resonator of the same width with a mean radius of 36.1 mm were fabricated. The spacing from the edge of the substrate to the transmission line was roughly 30 mm. The circuit layout is shown in Fig. 6.2.

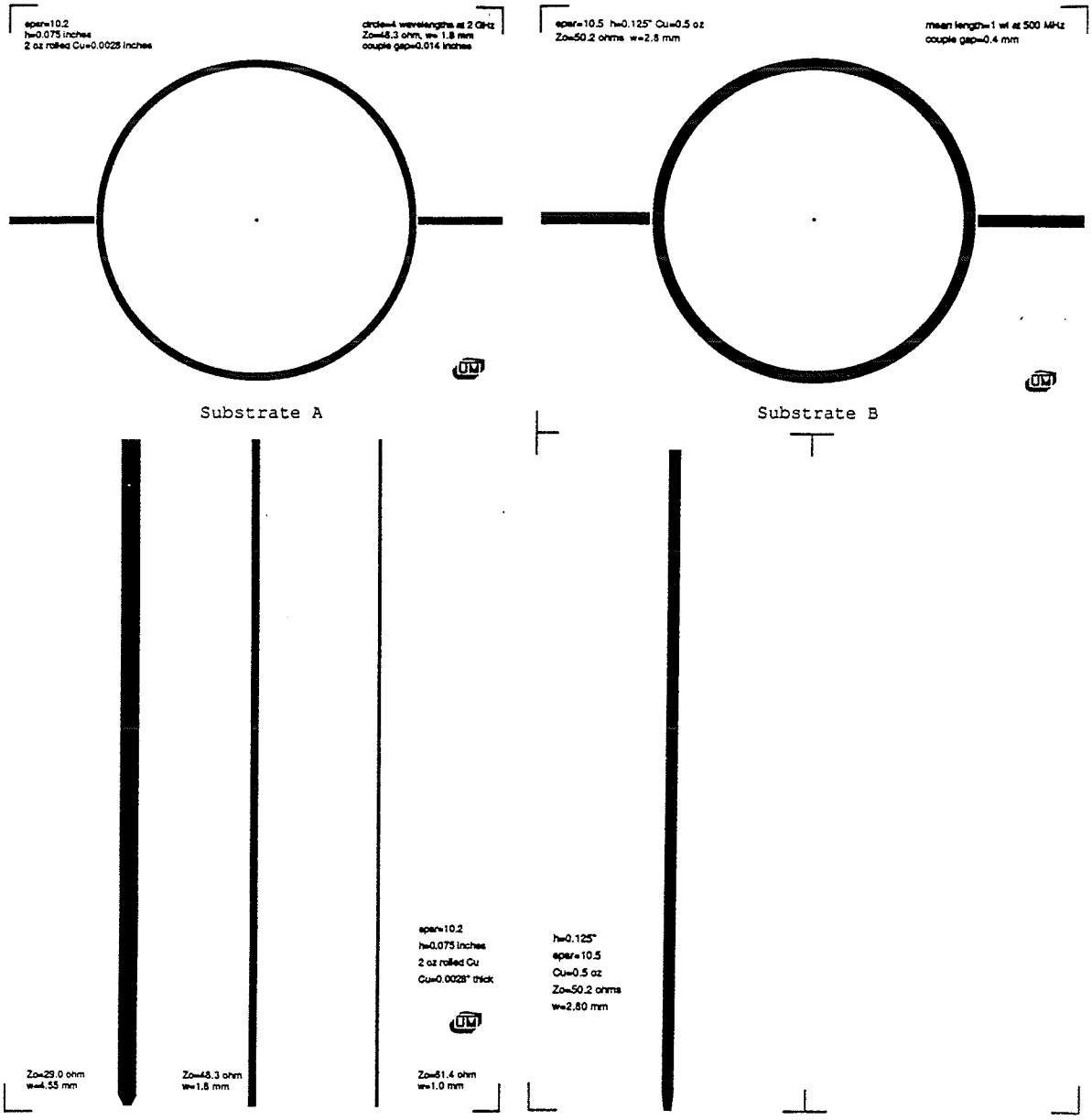


Figure 6.2. Test circuit layout.

## 6.2 Dispersion Measurement Techniques

### 6.2.1 Direct VSW Measurement

For the direct VSW measurement technique, the transmission line under test was chosen arbitrarily to be open circuited. In the case of substrate A, adjacent lines were short circuited using a shorting plane of copper tape to avoid mutual coupling effects. The coaxial probe was scanned along the length of the line with transmission coefficient measurements taken every 0.5 mm. Sampling at every 0.5 mm ensured that the VSW was sampled at no less than $\lambda/15$ intervals throughout the frequency range of interest. An example of a typical VSW measurement is shown in Fig. 6.3.

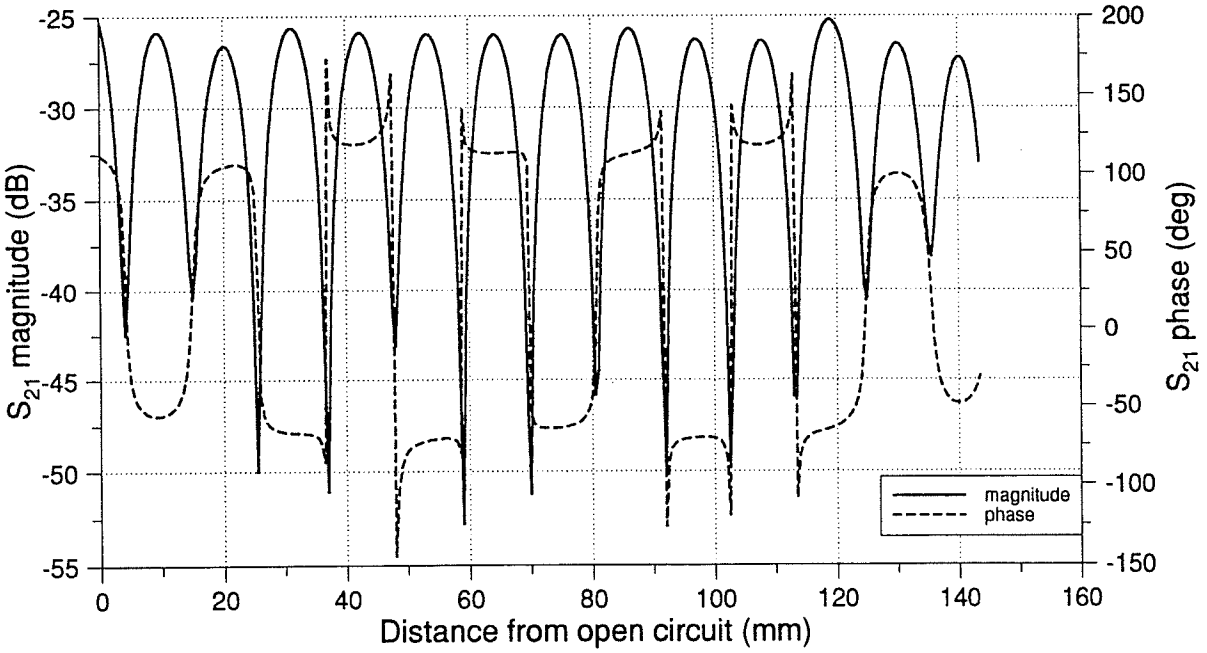


Figure 6.3 Sample VSW measurement on an open circuit 48.3 Ω line at 5 GHz.

At a selected test frequency the effective relative permittivity is given by

$$\varepsilon_{re}(f) = \left( \frac{c}{f \cdot \lambda_{ave}} \right)^2 \tag{6.1}$$

where c is the speed of light, f is the frequency, and $\lambda_{ave}$ is obtained from an average of the measured $\lambda/2$ values.

### 6.2.2 Sliding Load

The sliding load technique involves measuring the input reflection coefficient of the transmission line while a load is scanned along the length of the line. In Figs. 6.4a,b the sliding load is represented by $Z_{sl}$ and the line termination impedance by $Z_t$. The input impedance of a lossless transmission line of characteristic impedance $Z_o$ terminated in an impedance $Z_t$ is given by

$$Z_{in} = Z_o\left(\frac{Z_t + jZ_o \tan\beta z}{Z_o + jZ_t \tan\beta z}\right) \tag{6.2}$$

where z is the distance from the load $Z_t$ and $\beta=2\pi/\lambda$. Using (6.2) it is relatively simple to show that for lossless lines, the input impedance $Z_{in}$ for case (a) and (b) in Fig. 6.4 are the same. For lossy lines the magnitude and phase of $Z_{in}$ are still periodic by $\lambda/2$. The attainable accuracy is a function of the absorbing material and the dimensions of the microstrip line as well as the consistency of the load as it is positioned along the line.

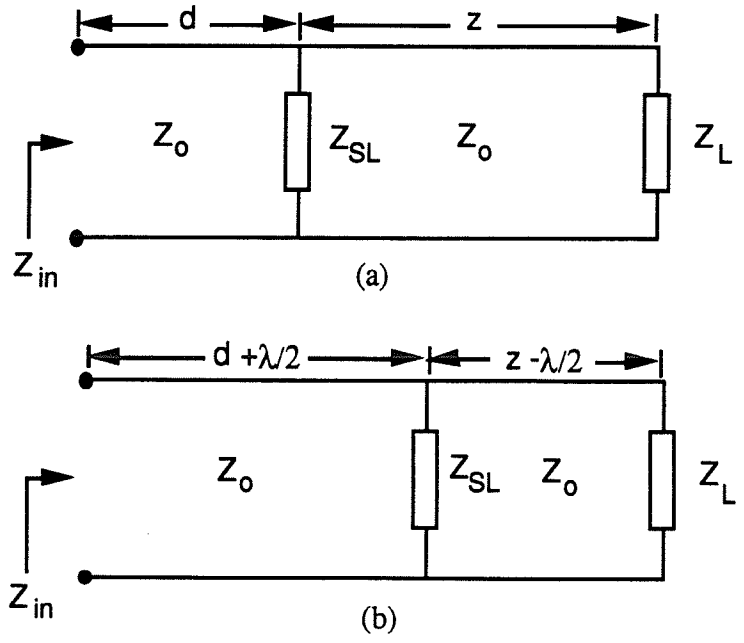


Figure 6.4. Periodic input impedance of (a) the sliding load on a transmission line. (b) The sliding load moved a distance $\lambda/2$.

For this experiment an open circuit metallic probe which made contact with the center of the test line was used as the load with $S_{11}$ measurements taken every 0.5 mm. A typical result of the measured input reflection coefficient is shown in Fig. 6.5. For a consistent

load on a lossless transmission line, the measured input reflection coefficient should repeat at $\lambda/2$ intervals. Equation (6.1) can then used to obtain $\varepsilon_{re}(f)$.

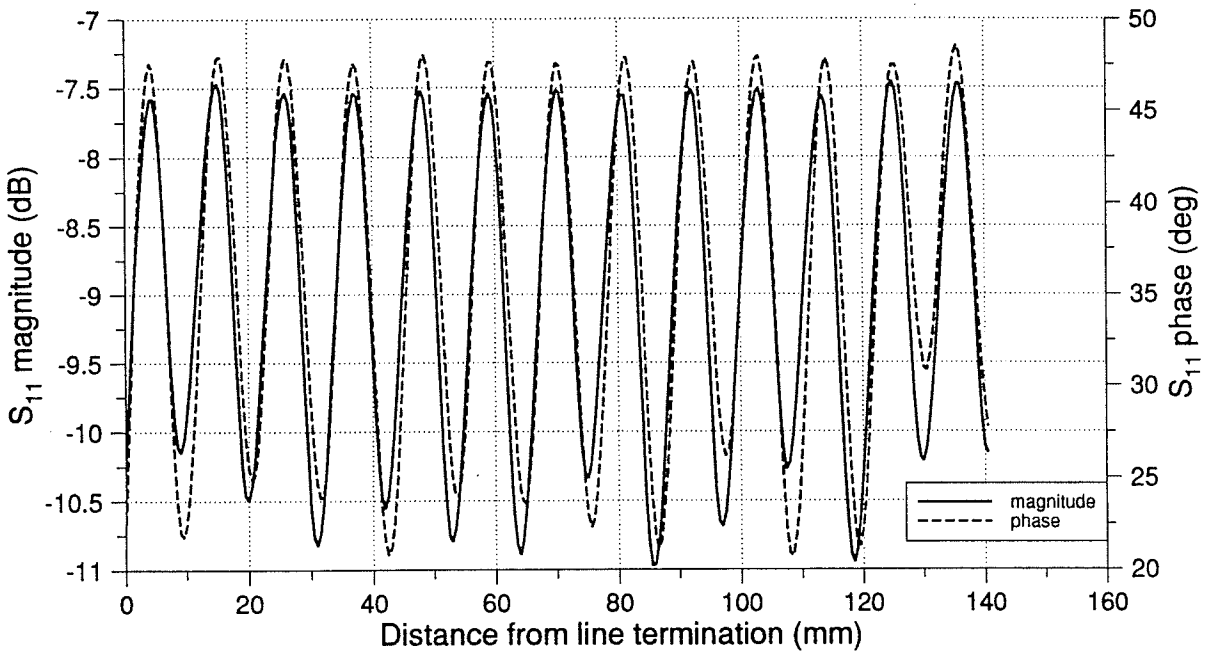


Figure 6.5. $S_{11}$ measurement on an open circuit 48.3 Ω line with a metallic sliding load at 5 GHz.

### 6.2.3 Ring Resonator

The motivation for using a ring resonator for dispersion measurements was to eliminate end effects from either open or short-circuit terminations used in other resonant mode techniques. They have been implemented in a wide variety of applications including both MIC's and MMIC's [47]. Troughton [45] states that the ring should be at least 5 wavelengths long at the frequency of interest in order to avoid the effects of mutual inductance. In addition, the ratio of the line width to the outer radius should be much less than one to ensure that the resonant frequencies are not displaced [48]. Excitation of the ring resonator was achieved by gap coupling (see Fig. 6.6) two microstrip lines at opposite sides of the ring. Ideally the gap should be chosen such that the ring resonator is unloaded and the ring modes are not perturbed.

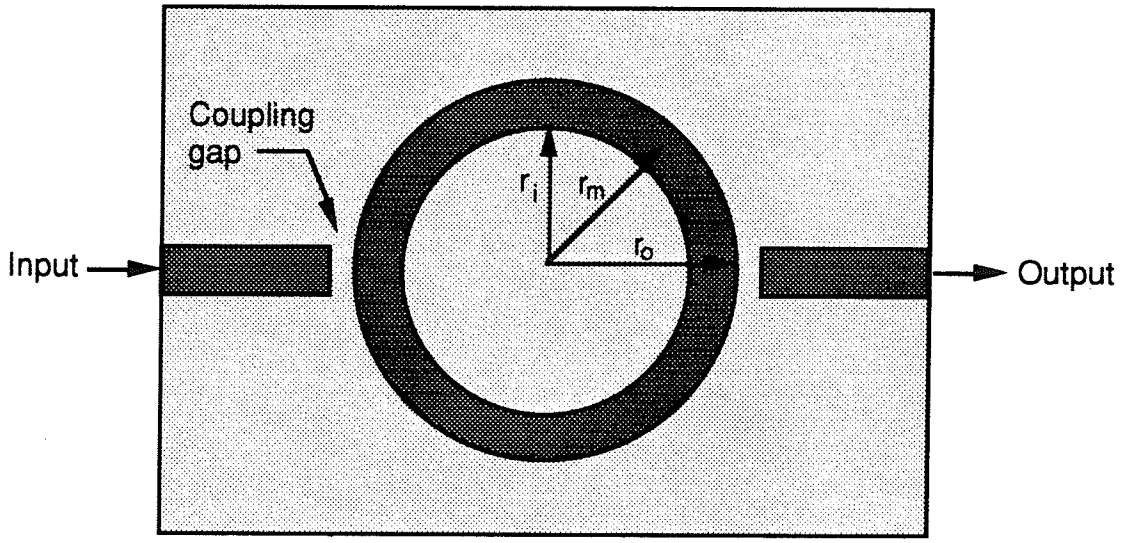


Figure 6.6. Microstrip ring resonator with gap coupled input/output arms.

Although ring resonators overcome the difficulties associated with open and short circuit terminations other problems may arise when measurements on either very high or low impedance lines are required. It has been noted in [29] that difficulties associated with 1) curvature effects, 2) frequency pulling due to coupling problems, and 3) the manufacture and physical measurement of high-tolerance thin rings may arise. This may not be feasible in MMIC technology with specialized substrates.

A ring resonator with $Z_0$ approximately equal to 50 Ω was designed on each of the substrates A and B. Both of the ring resonators fabricated had a mean radius $r_m$ of 36.1 mm ensuring that the $w/r_0$ ratio was negligible. Corresponding to the mean circumference, both rings are fundamentally resonant at roughly 500 MHz (mean electrical length=$\lambda_g$). An approximation of the first order resonance is sufficient as the actual value is measured accurately on a network analyzer. Subsequent resonances occur at an integral number of wavelengths. At any resonance the wavelength is obtained by dividing the mean circumference by the harmonic number.

The coupling gaps for the rings were chosen arbitrarily small (<1 mm) with loading effects not considered. Due to errors in the etching process the coupling gaps of ring A were not to specifications. However, the coupling gaps on ring B were produced as specified to 0.4 mm. Typically, the gap widths should be increased so that the unloaded ring structure is measured. To limit the gap coupling loading effect, $Q$ factor measurements are used to determine the gap which yields the unloaded $Q$ factor [49].

Resonant frequencies were measured experimentally on a Wiltron 360 network analyzer. The transmission coefficient of the two port device was measured over a broad range of frequencies with a resolution of 1 MHz. The resonant frequencies are clearly indicated by the sharp peaks of Figs. 6.7a,b. For ring A the range of measurable frequencies was found to be 0.504 to 10.647 GHz, while for ring B the range was from 0.493 to 8.057 GHz. Beyond 8.057 and 10.647 GHz for the respective resonators the transmission peaks are indeterminate. According to Troughton [45] measurements of $\varepsilon_{re}$ should be taken at frequencies greater than 2.5 GHz for both rings A and B.

The bandwidth of this measurement technique is limited by mutual coupling effects at the low end while at the upper end connector discontinuities and/or the propagation of higher order modes are the major limitations. Using the planar waveguide model described earlier, it can be shown that the cutoff frequency for the $HE_1$ mode is 12.9 GHz for ring A and 7.92 GHz for ring B.

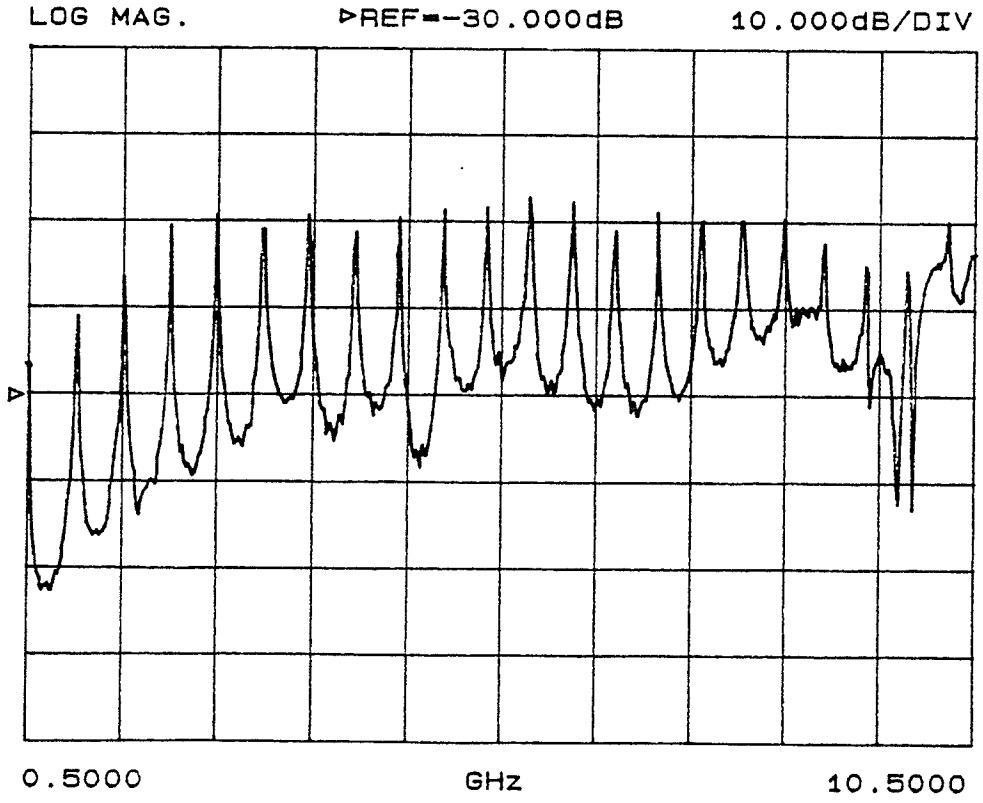


Figure 6.7a. Measured resonant frequencies of ring resonator A.

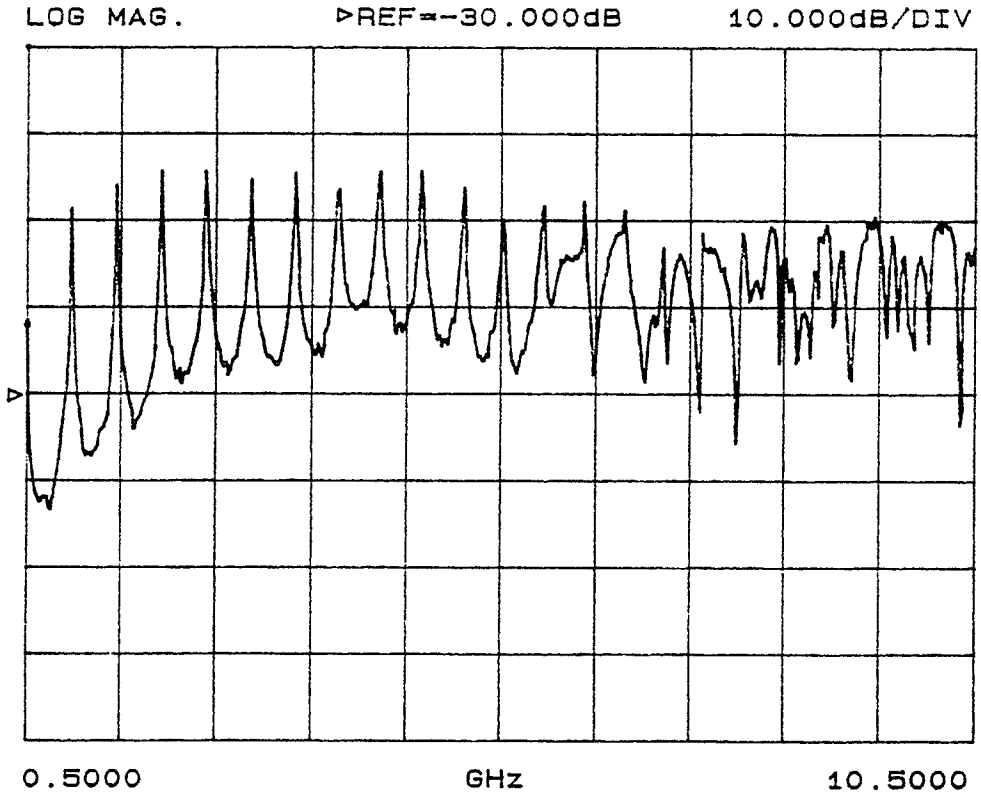


Figure 6.7b. Measured resonant frequencies of ring resonator B.

## 6.3 Experimental Results

For reference, a few closed-form dispersion expressions [31],[25],[32],[33] have been plotted for the four test lines with results of $\varepsilon_{re}(f)$ given in Figs. 6.8a,b,c,d. Though these formulas are based on the assumption that t=0, they have been implemented here with $\varepsilon_{re}(0)$ altered to account for t/h=0.04 on substrate A. To accomplish this, Garg and Bahl's [39] formula was used and predicts a decrease in $Z_o$ with t/h and and is considered accurate to within 4% for $\varepsilon_{re}(0)$ (subject to $0 \le t/h \le 0.2$, $0.1 \le w/h \le 20$, and $\varepsilon_r \le 16$). Kobayashi [32] claims to have the highest degree of accuracy (better than 0.6% for $0.1 < w/h \le 10$, $1 < \varepsilon_r \le 128$, and any $h/\lambda_o$) when compared to a rigorous numerical solution [35]. This formula is used for comparison with experimental results. The effective filling fraction formula for $\varepsilon_{re}(0)$ described by Kobayashi [36],[37] was not implemented since there is no specific method to account for a finite t/h ratio.

The results of the various experimental techniques are shown in Figs. 6.9a,b,c,d along with Kobayashi's [32] empirical formula. The two additional curves are the upper and lower bounding limits based on the manufacturers tolerances. It is worth noting that the

entire curve may be shifted up or down 4.6% based the accuracy of $\varepsilon_{re}(0)$ and the chosen dispersion formula. In spite of such uncertainties we define the error of measure $R_E^2$ given by

$$R_E^2 = \sum_{i=1}^{n}\left[\frac{(\varepsilon_{re}(f)\text{calc}_i - \varepsilon_{re}(f)\text{meas}_i)}{\varepsilon_{re}(f)\text{meas}_i}\right]^2 \tag{6.3}$$

for n test frequencies where the RMS error per measurement is

$$E_{rms} = \sqrt{\frac{R_E^2}{n}} \tag{6.4}$$

with $\varepsilon_{re}(f)$calc obtained from [32] and $\varepsilon_{re}(0)$ from [39] using the manufacturers nominal substrate parameters. The $\varepsilon_{re}(f)$meas results are obtained using either the sliding load, ring resonator, or direct VSW measurement technique. The results are tabulated in table 6.1.

Table 6.1. RMS error for various experimental techniques relative to [32] with nominal substrate parameters.

| $Z_o$ (Ω) | Measurement technique | n | $E_{rms}$ (%) |
|---|---|---|---|
| 29.0 (A) | VSW measurement | 24 | 2.07 |
| | Sliding load (magnitude) | 21 | 2.03 |
| | Sliding load (phase) | 11 | 1.92 |
| 48.3 (A) | VSW measurement | 25 | 2.30 |
| | Sliding load (magnitude) | 25 | 2.18 |
| | Sliding load (phase) | 16 | 1.41 |
| | Ring resonator | 23 | 0.85 |
| 61.4 (A) | VSW measurement | 27 | 2.64 |
| | Sliding load (magnitude) | 30 | 3.66 |
| | Sliding load (phase) | 25 | 2.02 |
| 50.2 (B) | VSW measurement | 18 | 2.54 |
| | Sliding load (magnitude) | 18 | 2.16 |
| | Sliding load (phase) | 13 | 1.62 |
| | Ring resonator | 18 | 1.28 |

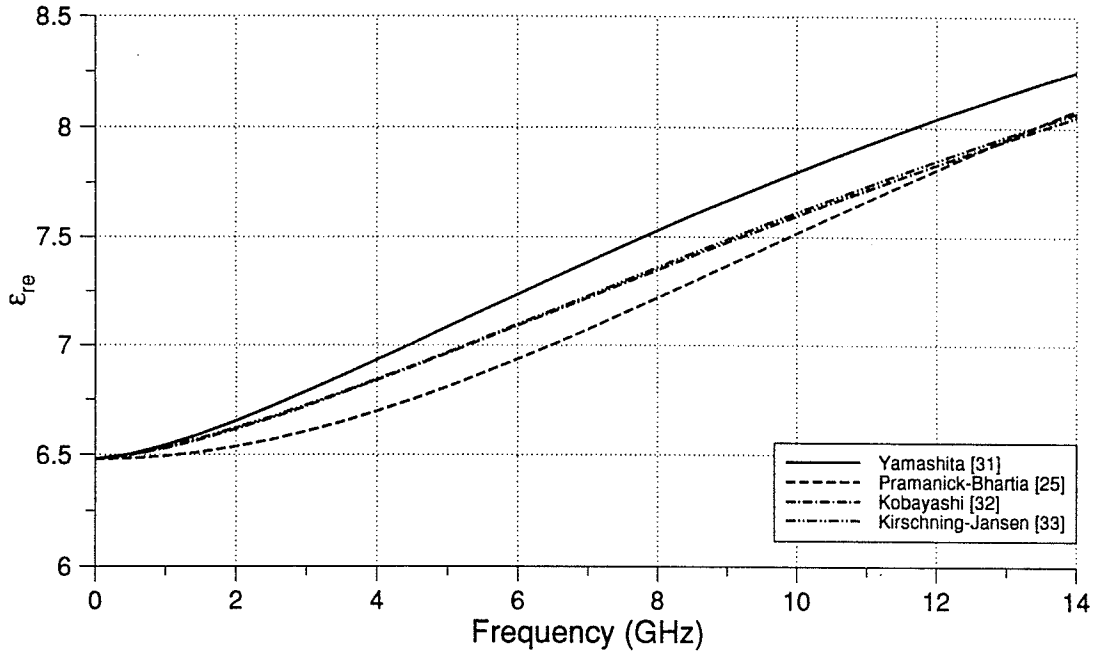


Figure 6.8a. Sample of closed form dispersion formulas applied to the 61.4 Ω test line on substrate A.

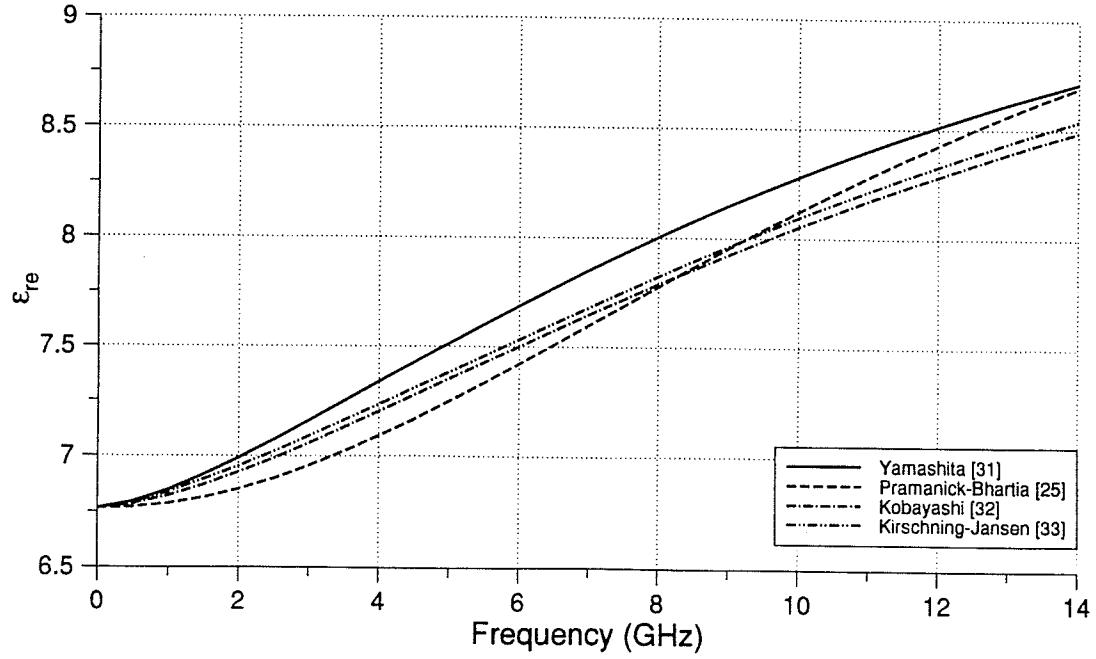


Figure 6.8b. Sample of closed form dispersion formulas applied to the 48.3 Ω test line on substrate A.

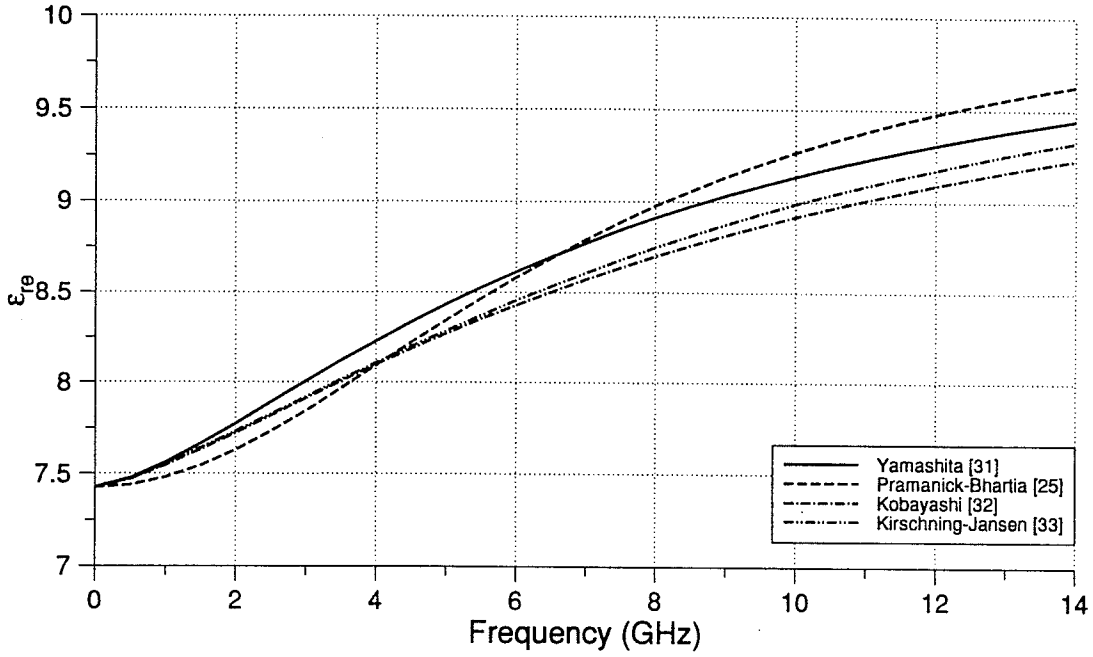


Figure 6.8c. Sample of closed form dispersion formulas applied to the 29.0 Ω test line on substrate A.

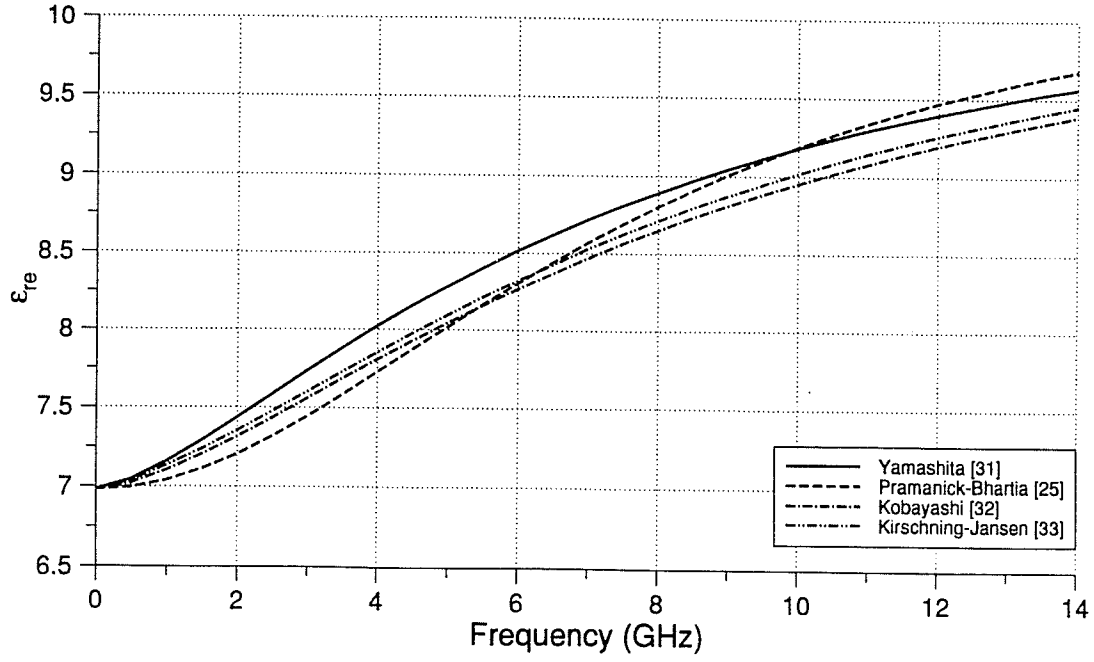


Figure 6.8d. Sample of closed form dispersion formulas applied to the 50.2 Ω test line on substrate B.

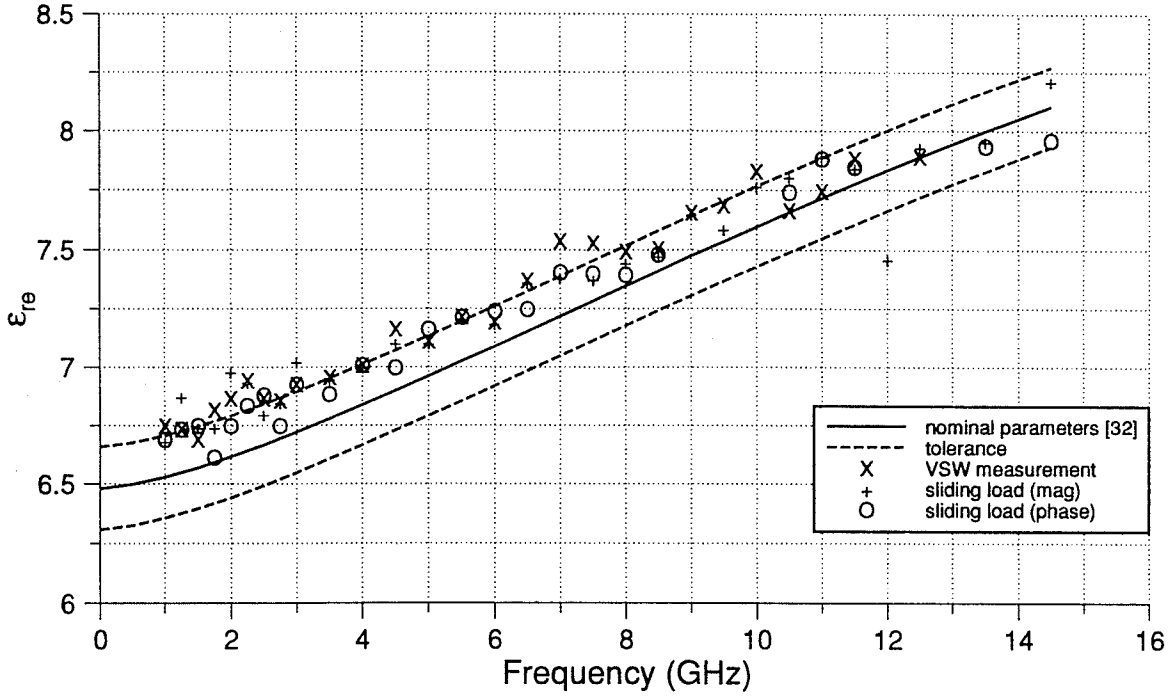


Figure 6.9a. Experimental results for the 61.4 Ω test line on substrate A with [32] for comparison. Tolerance curves based on manufactures specs.

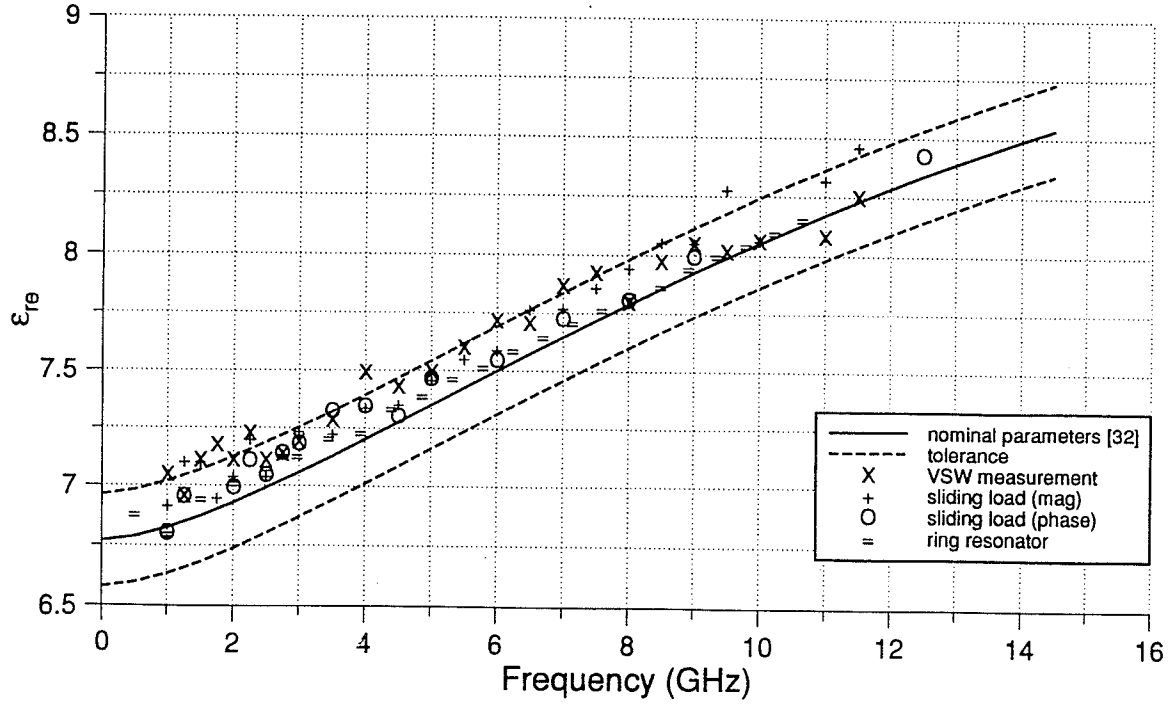


Figure 6.9b. Experimental results for the 48.3 Ω test line on substrate A with [32] for comparison. Tolerance curves based on manufactures specs.

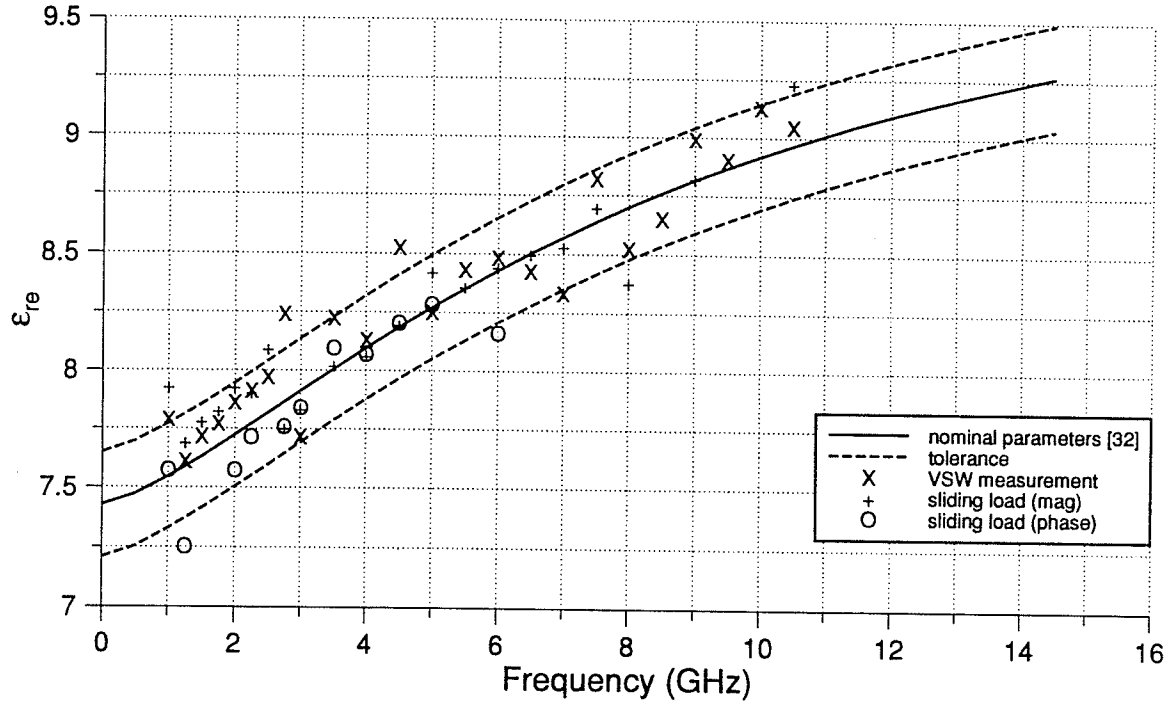


Figure 6.9c. Experimental results for the 29.0 Ω test line on substrate A with [32] for comparison. Tolerance curves based on manufactures specs.

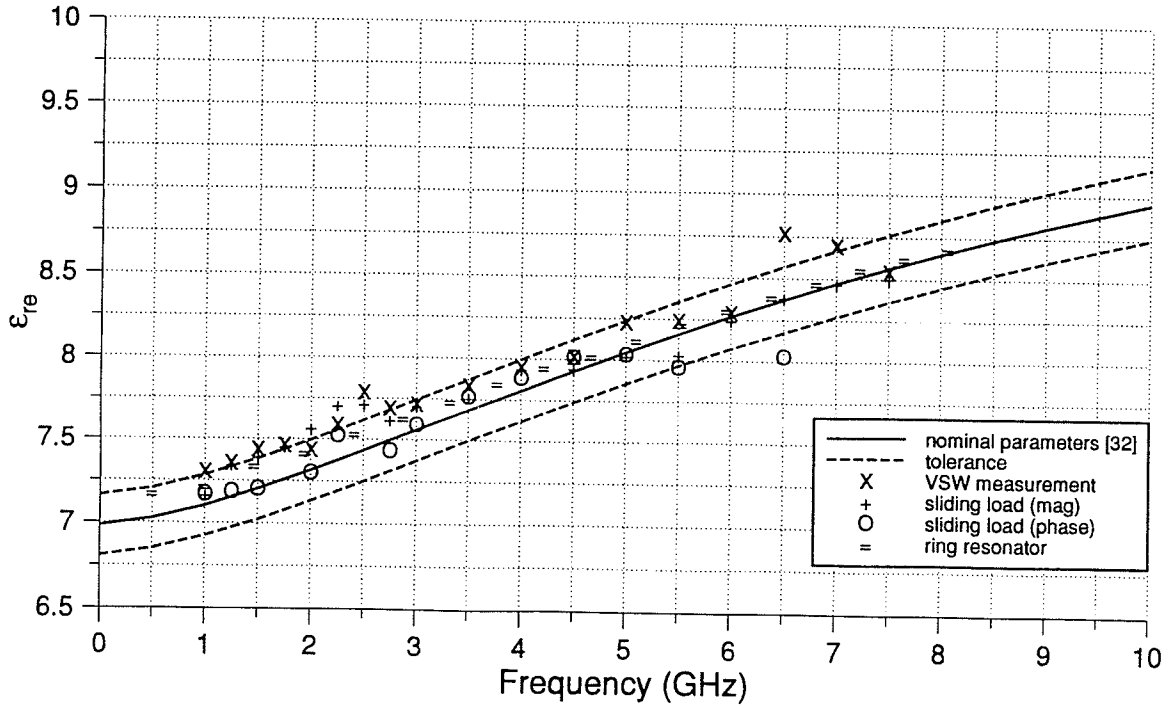


Figure 6.9d. Experimental results for the 50.2 Ω test line on substrate B with [32] for comparison. Tolerance curves based on manufactures specs.

The VSW measurement technique results in Figs. 6.9a,b,c,d were obtained by finding the distance between two successive voltage minimums where a 180° phase shift occurs. The capacitive loading of the probe was measured to be at most 2% on $S_{11}$ measurements of the transmission line and typically on the order of 1%. Figure 6.10 is a plot of the measured input reflection coefficient of a transmission line as the probe is scanned along the center of the line. This effect can be reduced by using a smaller diameter coax with a high surface impedance outer conductor. For the sliding load technique the magnitude and phase results are considered separately though this need not be the case. One limitation of guided wavelength measurement techniques is the excitation of higher order modes at higher frequencies which can perturb the VSW on the line.

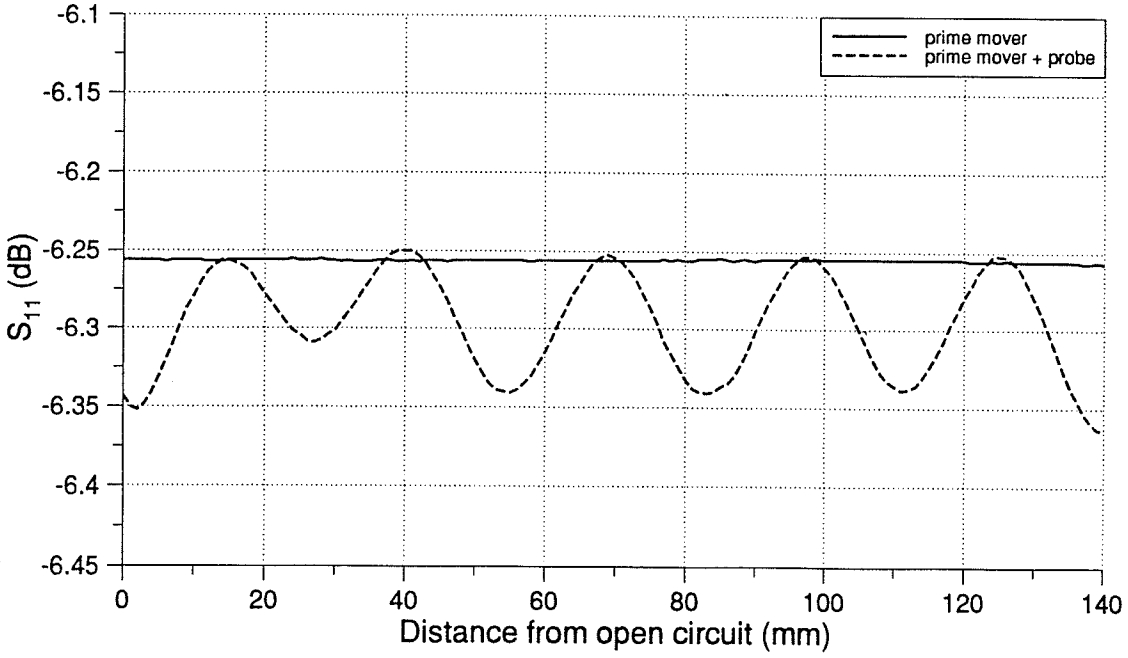


Figure 6.10. $S_{11}$ measurement with and without the probe being scanned along the length of the 48.3 Ω line at 2 GHz.

In Figs. 6.9a,b the results are clustered around the upper tolerance curve while in Fig. 6.9c they are scattered about the nominal curve. This discrepancy may be in part due to the etching inaccuracy which left a noticeable ripple along the edge of the lines. This edge variation is expected to increase $\varepsilon_{re}(0)$ for the narrower lines to a greater degree than for the wider line. The ring resonator results are the most consistent but are limited to discrete frequencies. Measurements for f<2.5 GHz was not recommended [45] but did provide

quite adequate results. This may not be the case for a ring with a smaller $r_o/w$ ratio where mutual coupling may have a greater influence.

Until this point a comparison of the measured and calculated guided wavelength has not been discussed. Fig. 6.11 is a graph of the measured and calculated wavelengths versus frequency for the 50.2 Ω line on substrate B. Examination of $\lambda_g$ indicates excellent agreement between all methods. The discrepancies do not become apparent until this data is used to calculate $\varepsilon_{re}$ in (6.1). As the VSW technique relies on accurately measuring voltage minimums, the accuracy of determining $\varepsilon_{re}(f)$ as a function of $\lambda_g$ should be examined. In Fig. 6.12 the percent error in $\varepsilon_{re}$ is plotted versus the percent deviation of the measured wavelength with respect to the actual wavelength. Note that for wavelength deviations within the range of ±10% the expected error in $\varepsilon_{re}$ is roughly double, hence the discrepancy is more noticeable in the graphs of $\varepsilon_{re}(f)$. Minimizing the error in the measured wavelength can be done by using smaller sampling interval and/or a smaller probe with better spatial resolution.

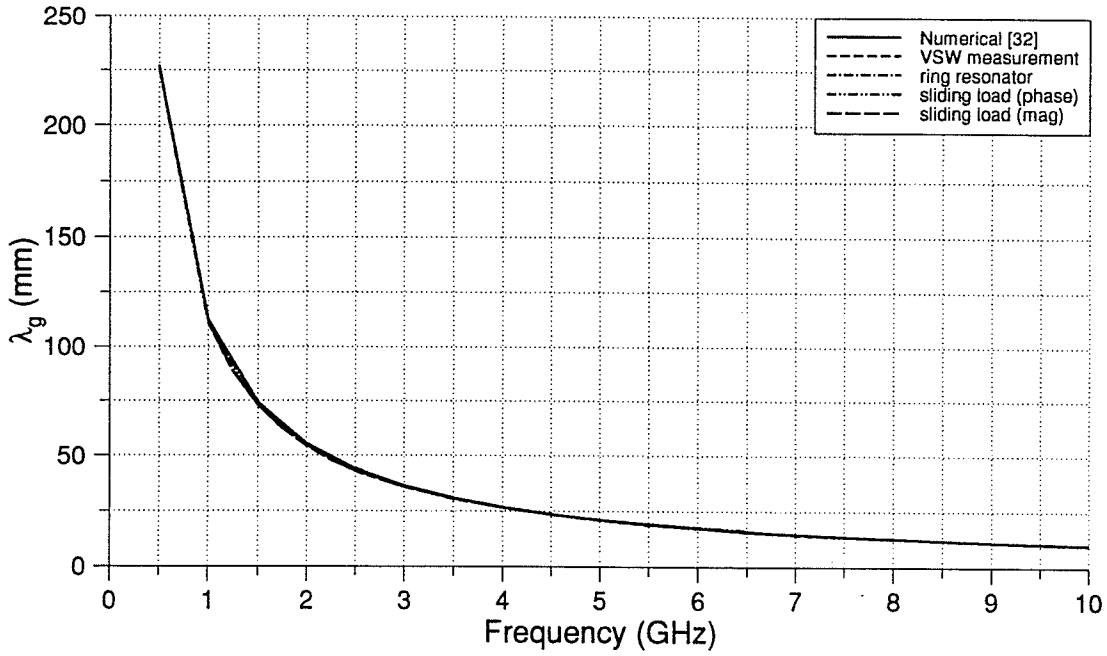


Figure 6.11. Guided wavelength versus frequency for 50.2 Ω line on substrate B.

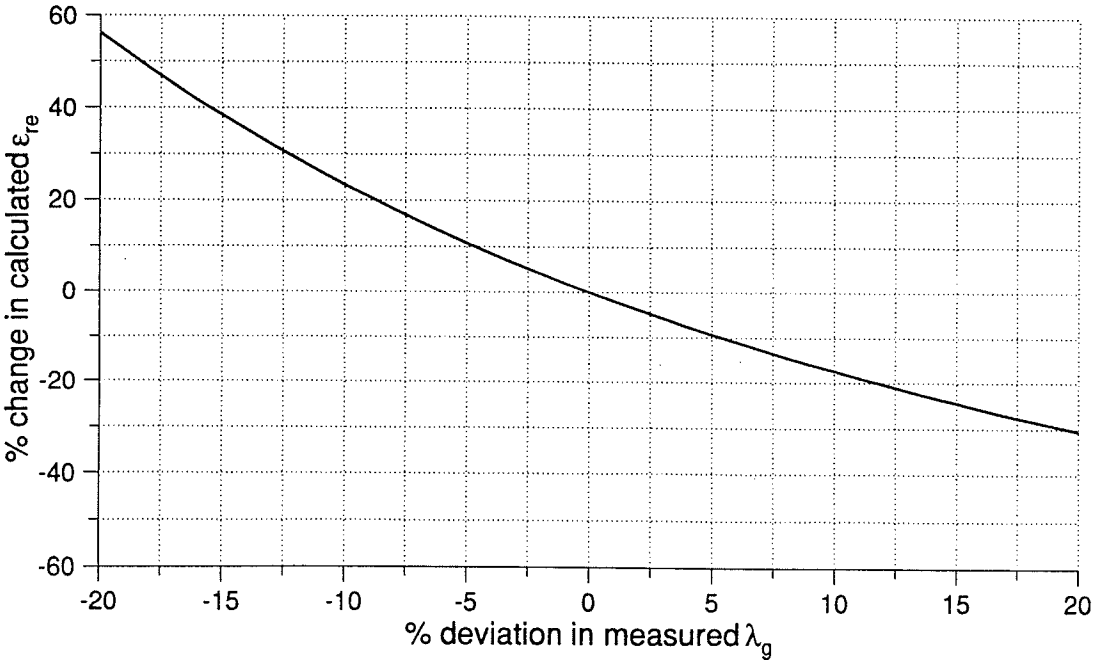


Figure 6.12. Expected error in $\varepsilon_{re}(f)$ due to the measurement error in the guided wavelength.

# Chapter 7

## High Frequency Circuit Testing

In this chapter experiments are performed on a wide variety of applications. To further expand on previous measurements [17],[18] which included modal analysis of resonant microstrip antennas, additional experiments have been performed. Tests on applications ranging from travelling wave antennas to coupled line filters have been analyzed to illustrate the value of the coaxial probe as a diagnostic tool. Some of the information provided by these tests is unavailable from conventional measurement techniques. Depending on the application the sampling interval may be in the mm to μm range. Typically 50 to 250 field data samples per observation point are taken to increase the signal to noise ratio.

### 7.1 Coaxial Monopole Probe

#### 7.1.1 Coplanar Waveguide

The use of coplanar waveguides (CPW) in microwave integrated circuits is very popular since it adds flexibility and improves the performance of some circuit functions at high frequencies. The CPW architecture allows for the mounting of lumped components in a shunt or series configuration, while eliminating the need for drilling holes or slots through the substrate.

An open circuit CPW on an alumina substrate ($\varepsilon_r$=9.8, s=210 μm, w=75 μm) was used for testing at an operating frequency of 22 GHz. The results of a transverse scan are shown in Fig. 7.1a along with the calculated magnitude and phase of the electric field in Fig. 7.1b. A coaxial probe with $D_o$=0.013", $D_i$=0.0031", and t=185 μm was used for the experiment. The height of the probe above the CPW was not calibrated. An average of

200 readings per observation point were taken along with a sampling interval of 10 μm. The results of a longitudinal scan of the CPW are shown in Fig. 7.2.

### 7.1.2 Travelling Wave Antenna

A microstrip traveling wave antenna under development [50] is shown in Fig. 7.3. A travelling wave antenna has been defined in [51] as, "An antenna for which the fields and currents that produce the antenna pattern may be represented by one or more travelling waves, usually in the same direction." To eliminate any reverse travelling waves the antenna is match terminated.

Since a straight microstrip line has minimal radiation due to its field distribution, discontinuities are introduced to enhance the radiation characteristics. The discontinuities in Fig. 7.3 are in the form of corners. The objective of this particular design was to achieve circular polarization. To achieve this the microstrip transmission line is shaped such that the radiated field components are equal in magnitude and 90° out of phase at the design frequency.

A coaxial probe ($D_O$=0.0865", $D_O$=0.0201", and tip length t=1.5 mm) was used to scan the antenna at 1 mm sampling intervals. The test frequency was 3.1 GHz and is labeled in the $S_{11}$ measurement of Fig. 7.4. This frequency was selected since corresponding radiation measurements were available. The results shown in Figs. 7.5a,b indicate the magnitude and in Fig. 7.5c the relative phase of the charge density on the travelling wave antenna. The variation of the magnitude in Figs. 7.5a,b indicates the effects of the bends along the structure and how well the antenna is matched to the source. The phase progression in Fig. 7.5c illustrates the phase shift necessary for circular polarization.

A program has been developed [52] which allows for digitized scan paths. Therefore, by digitizing points along the transmission line a custom scan path can be defined. This eliminates the need for two-dimensional scans on such structures. However, this program currently lacks GPIB compatibility.

### 7.1.3 GaAs Slot Antenna

A microstrip integrated slot antenna is under development [53] as a possible array element for a millimeter wave integrated phased array antenna. The slot is etched on a 100 μm thick GaAs wafer and fed by a coplanar transmission line. The wafer is backed with

foam and a microwave absorbing material to simulate free space on both sides (see Fig. 4.3a for experimental setup).

Measurements were taken in the slot region outlined in Fig. 7.6 using a coaxial probe ($D_o$=0.013", $D_i$=0.0031", and t=185 μm) and a sampling interval of 20 μm at 17.25 GHz. To get an indication of the match at various frequencies the voltage standing wave along the feed line was measured. The VSW's on the feed line at various frequencies are shown in Fig. 7.7. The results show the magnitude (Figs. 7.8a,b) and phase (Fig. 7.8c) progression around the slot.

### 7.1.4 Coupled Line Filter

A 5th order bandpass Chebychev microstrip coupled line filter has been fabricated [54] and is shown in Fig. 7.9. The resonant frequency of the structure occurs at 2.336 GHz where the effective length of each of the 6 coupled elements is λ/4. The 3 dB bandwidth was found to be 146 MHz from the $S_{21}$ measurement shown in Fig. 7.10. The filter was scanned at 2.31 GHz with a coaxial probe ($D_o$=0.0865", $D_i$=0.0201", and t=1.5 mm) at 2 mm sampling intervals. Since the filter is a two port device, one port was match terminated to eliminate reflections. In Fig. 7.11a,b the standing wave pattern on each element is clearly evident. In Fig. 7.11c the phase progression indicates that a 180° phase shift occurs across each coupling element.

### 7.1.5 Cavity Resonator Antenna

A unique cavity resonator antenna is currently being researched at the Communications Research Center in Ottawa for applications involving integrated active antennas [55]. The design shown in Figs. 7.12a,b relies on a resonant mode in a cylindrical cavity to excite the radiating elements via an electromagnetically coupled slot. In addition, the cavity itself is excited by an electromagnetically coupled slot. the motivation for the intermediate cavity is to provide a heat sink for applications where thermal generation can be a major cause for concern. However, the tradeoff is bandwidth which is inherently limited for resonant structures.

The resonant frequency was found to be 6.368 GHz from the $S_{11}$ measurement shown in Fig. 7.13. The radiating elements were scanned at 6.363 GHz. A coaxial probe ($D_o$=0.0865", $D_i$=0.0201" and t=1.5 mm) was used for the experiment as shown previously in Fig. 4.2. Magnitude plots are provided in Figs. 14a,b and a phase plot in Fig. 14c. The measurement results help to verify that the antenna is linear polarized.

## 7.2 Double Loop Probe

### 7.2.1 Transmission Line Measurements

As an alternative to the monopole E-field probe mainly used for the measurements within this thesis, a simple double loop probe (see chapter 2 and [12],[13] for theory) shown in Fig. 7.15 was fabricated for preliminary testing. The probe design is such that the magnetic field generated by sources (such as neighboring lines) other than the printed line under test do not couple to the probe. Alternatively, printed lines directly under the probe couple efficiently with the probe, inducing currents which add constructively.

The loop was etched on a low permittivity ($\varepsilon_r$=2.5) 1/16" thick substrate and mounted on the end of a semi-rigid coax (refer to Fig. 7.15). An open circuit microstrip test line with parameters $\varepsilon_r$=10.2, w=0.8 mm, h=0.075" was scanned in a longitudinal and transverse manner at a frequency of 2 GHz. The results are shown in Figs. 7.16a,b. The constant decrease in the current standing wave maxima shown in Fig. 7.16a is due to the probe skewing slightly off center as the line was scanned. The dual side lobes are clearly displayed in Fig. 7.16b. The height of the probe above the substrate was not calibrated.

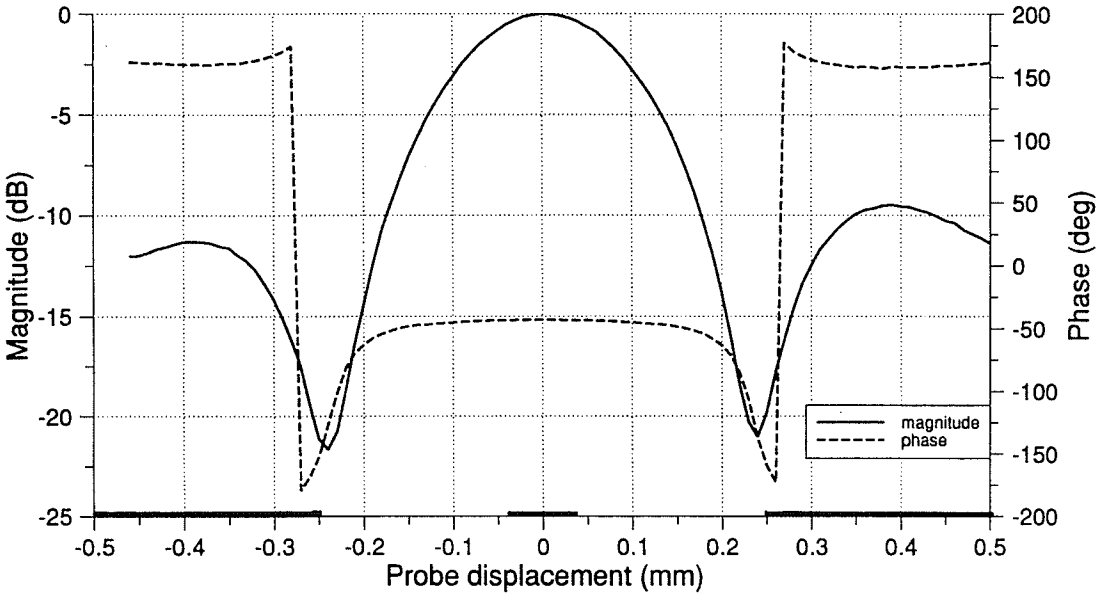


(a)

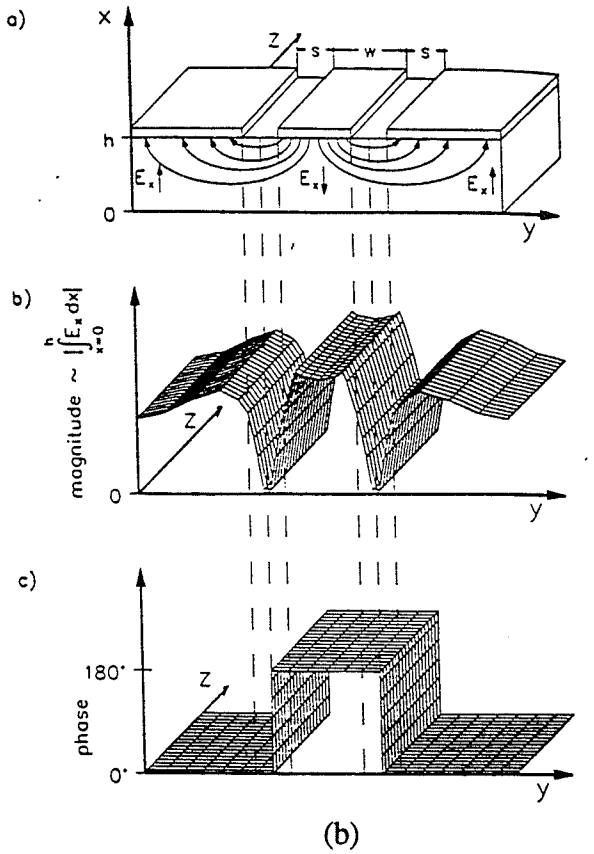


(b)

Figure 7.1. (a) Transverse scan of an open circuit CPW line at 22 GHz. (b) Calculated magnitude and phase of the voltage [7].

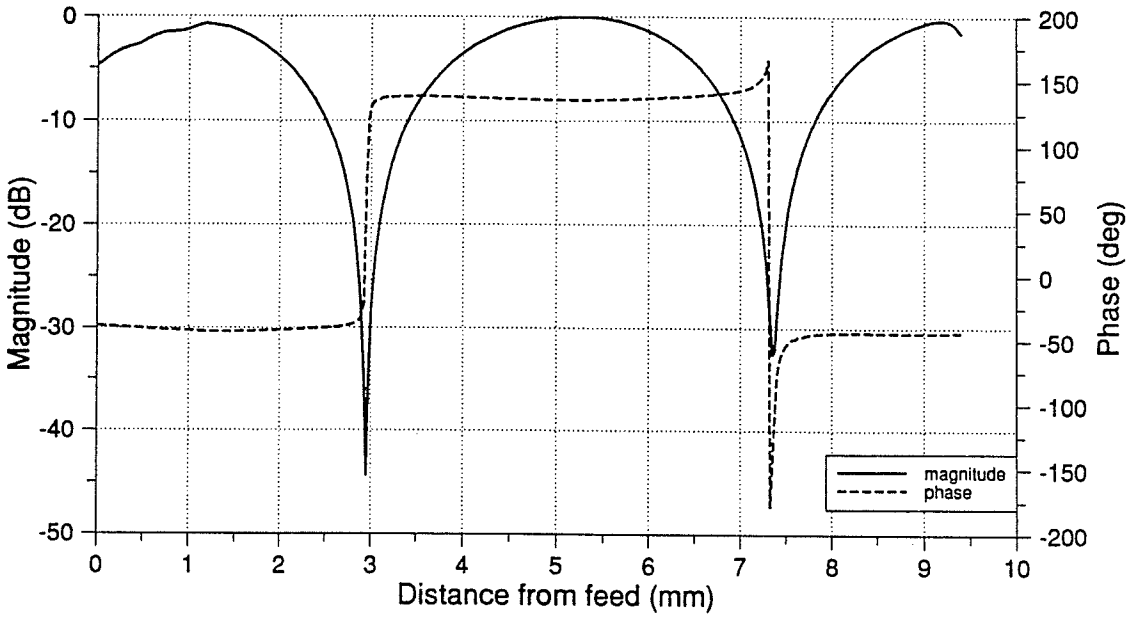


Figure 7.2. Longitudinal scan of an open circuit CPW line at 22 GHz.

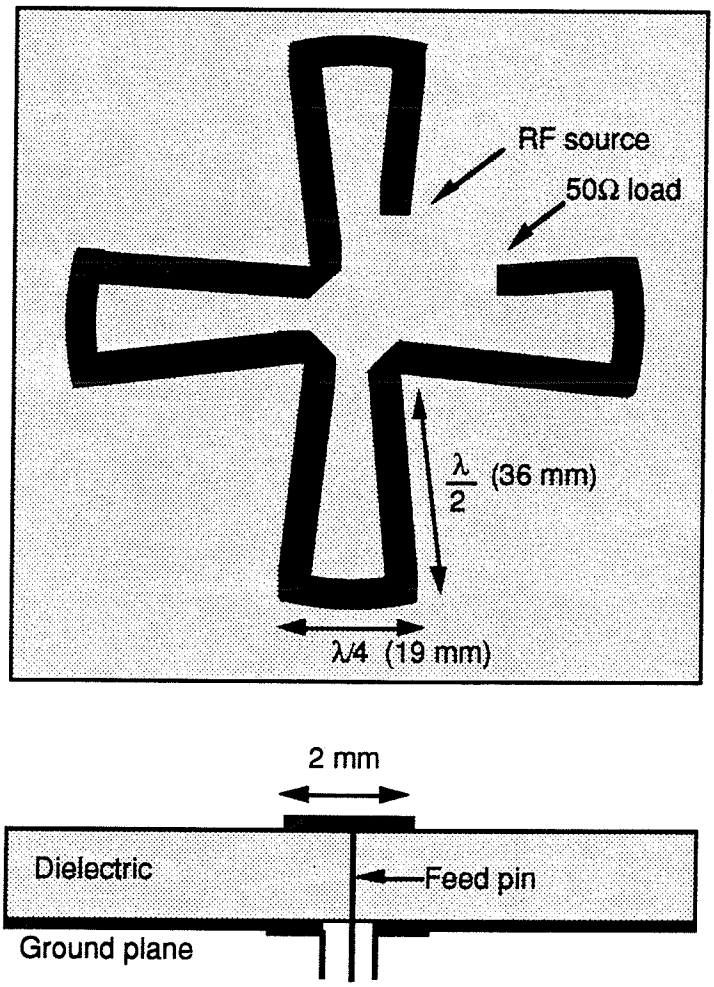


Figure 7.3. Sketch of a 4 arm microstrip travelling wave antenna [50].

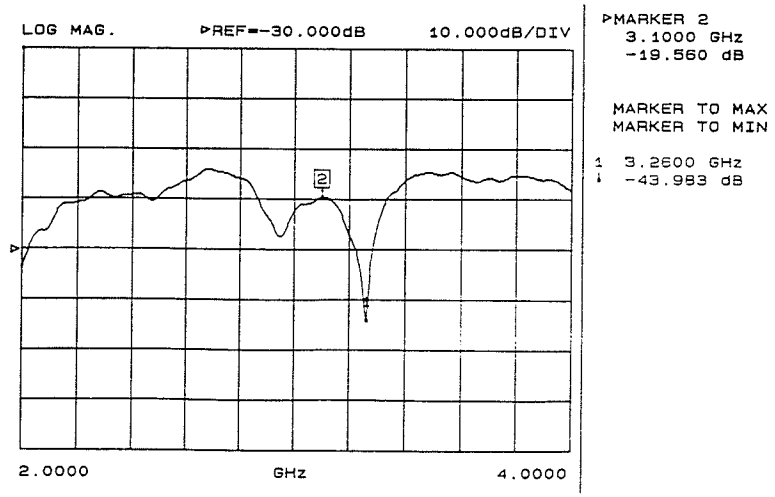


Figure 7.4. Calibrated $S_{11}$ measurement of travelling wave antenna with short arm match terminated.

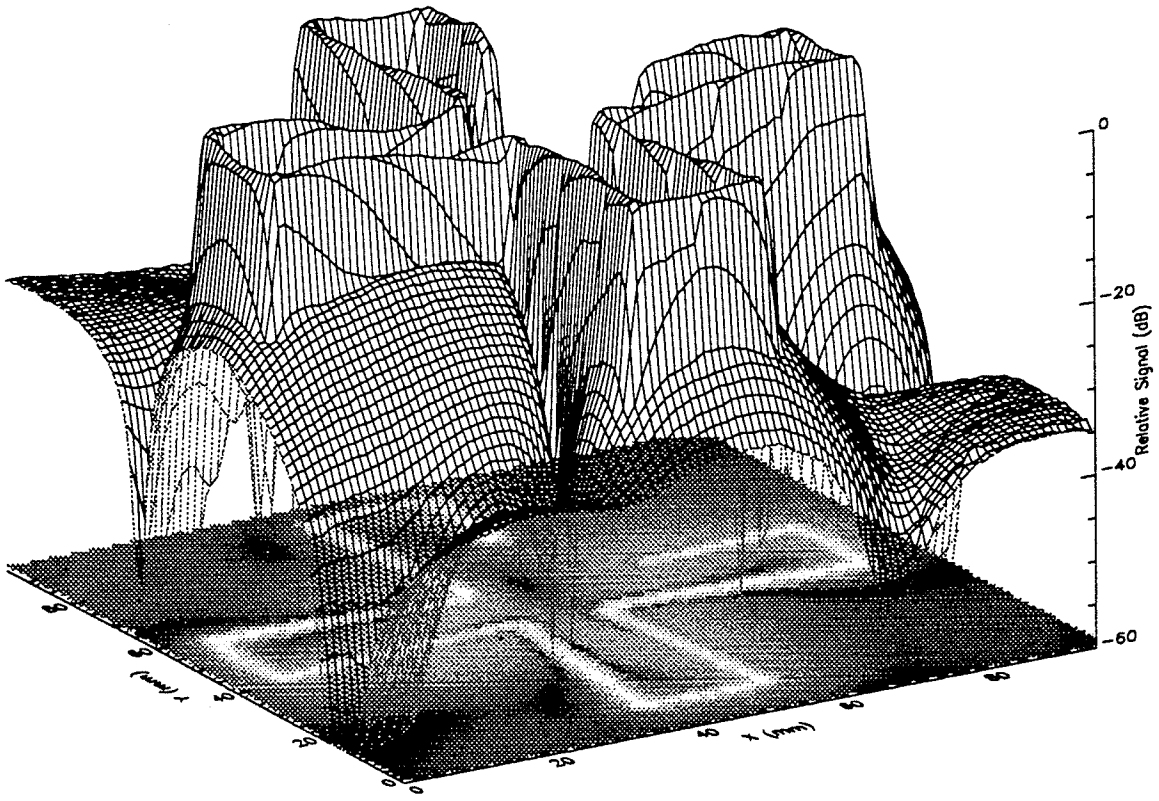


Figure 7.5a. Surface plot of the relative magnitude of the normal electric field component on the travelling wave antenna at 3.1 GHz.

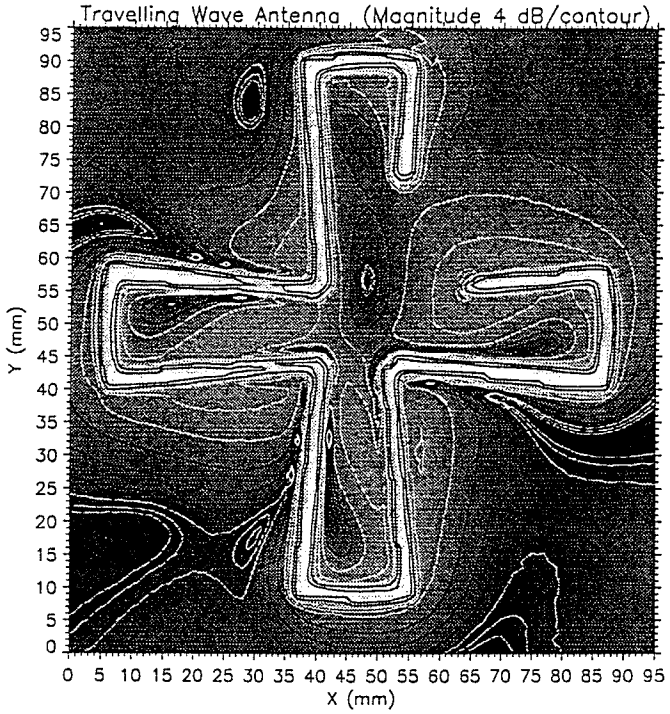


Figure 7.5b. Contour plot of the relative magnitude of the normal electric field component on the travelling wave antenna at 3.1 GHz.

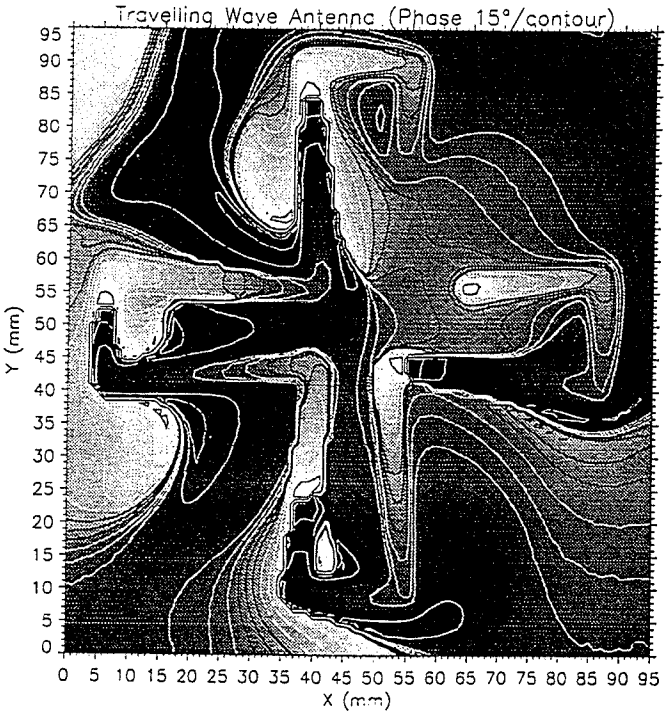


Figure 7.5c. Contour plot of the relative phase of the normal electric field component on the travelling wave antenna at 3.1 GHz.

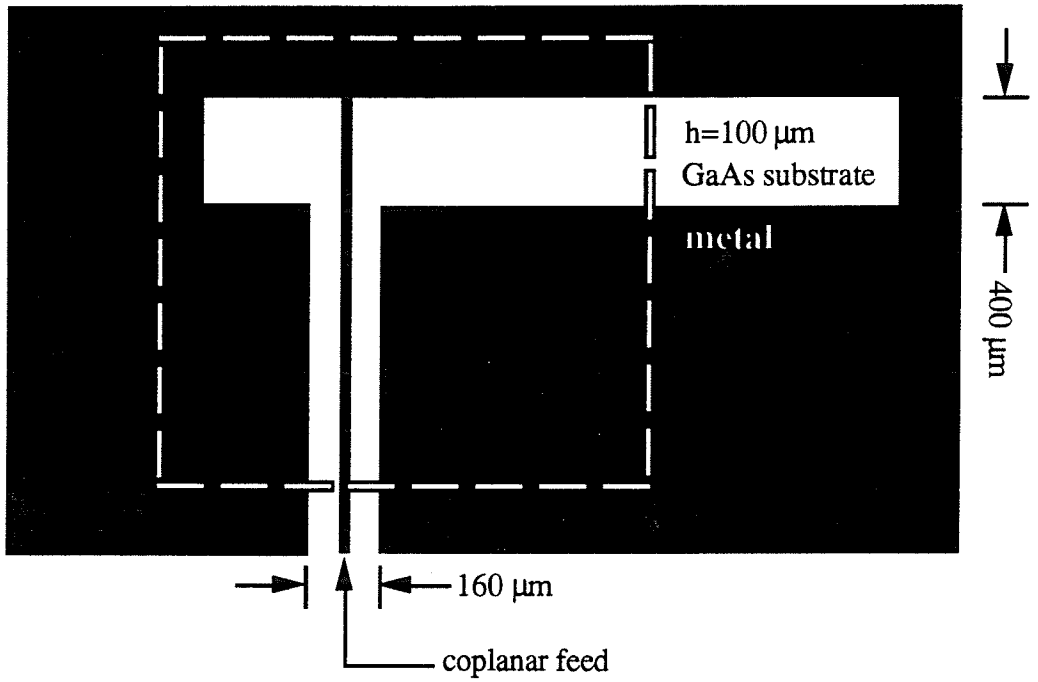


Figure 7.6. Sketch of the GaAs slot antenna and an outline of the area scanned.

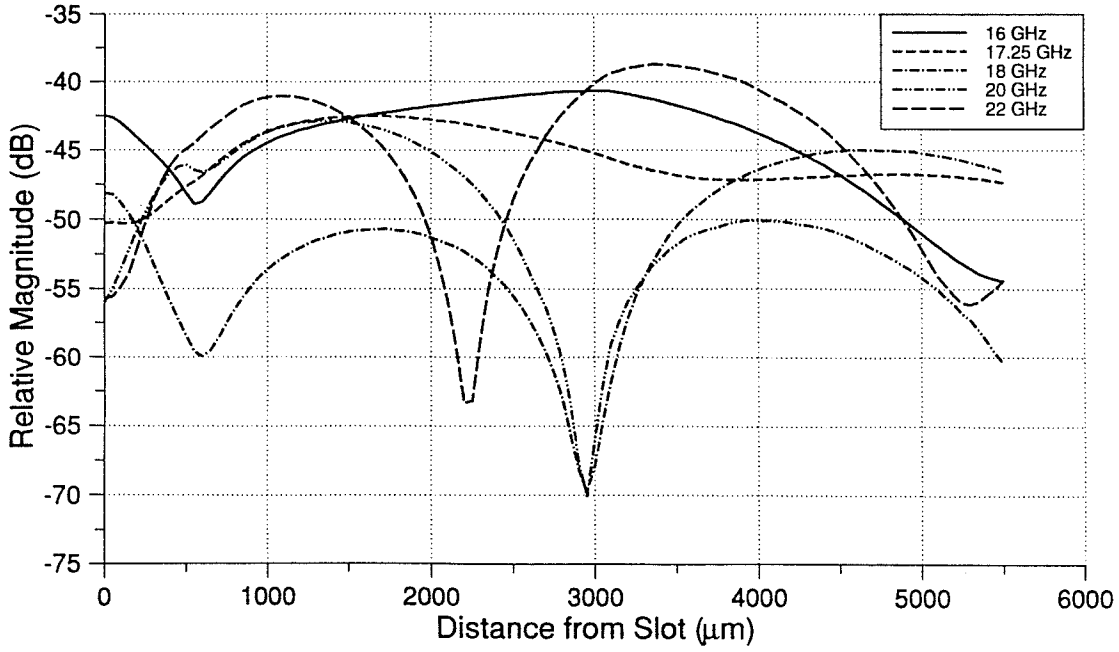


Figure 7.7. VSW on the coplanar feed line at various frequencies.

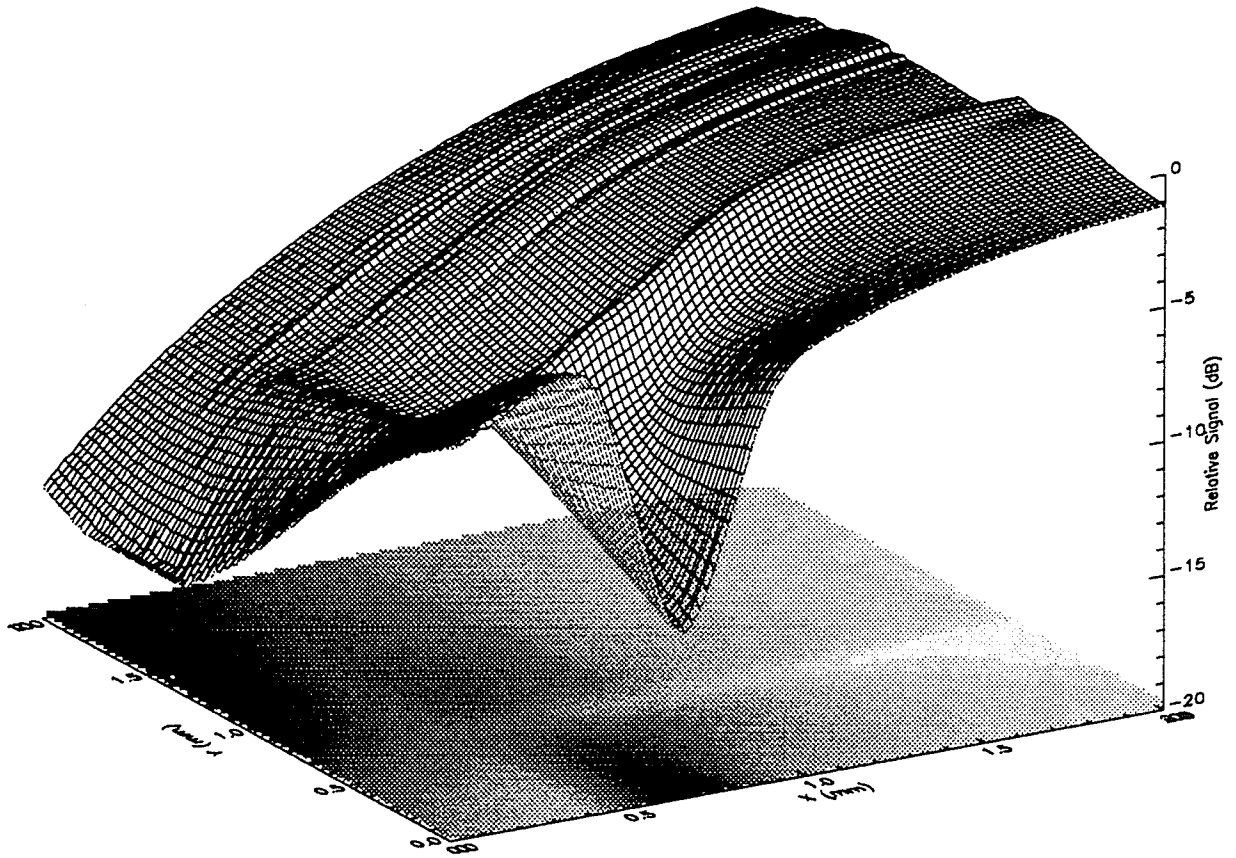


Figure 7.8a. Surface plot of the relative magnitude of the normal electric field component on the slot antenna at 17.25 GHz.

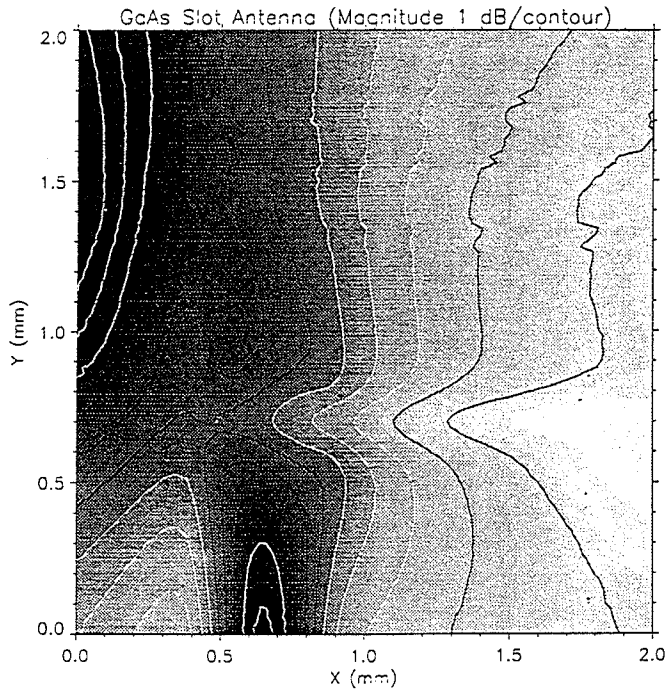


Figure 7.8b. Contour plot of the relative magnitude of the normal electric field component on the slot antenna at 17.25 GHz.

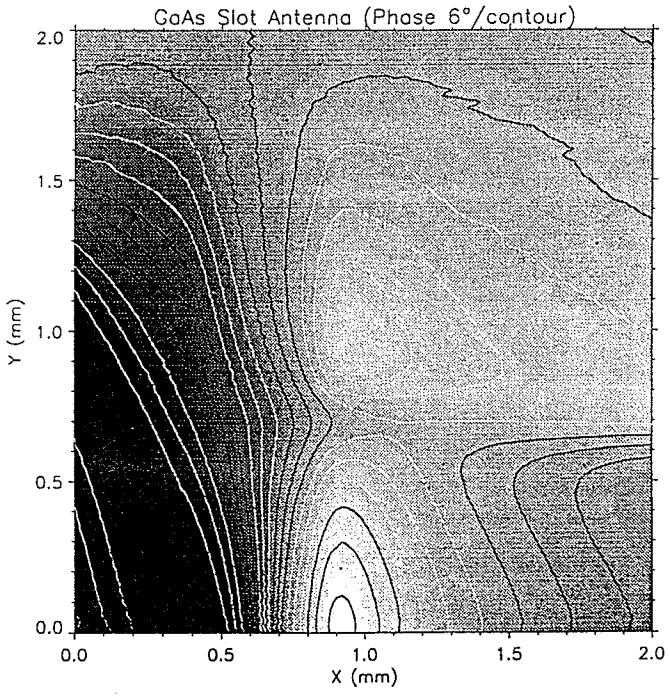


Figure 7.8c. Contour plot of the relative phase of the normal electric field component on the slot antenna at 17.25 GHz.

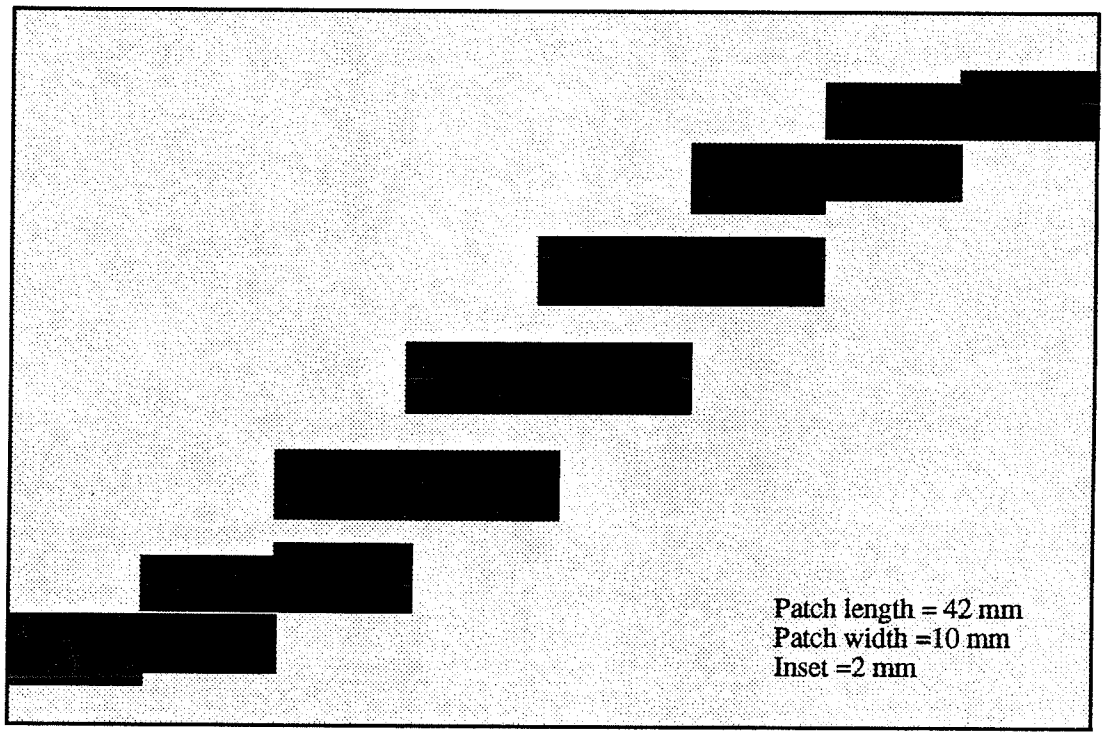


Figure 7.9. Fifth order bandpass Chebychev coupled line filter.

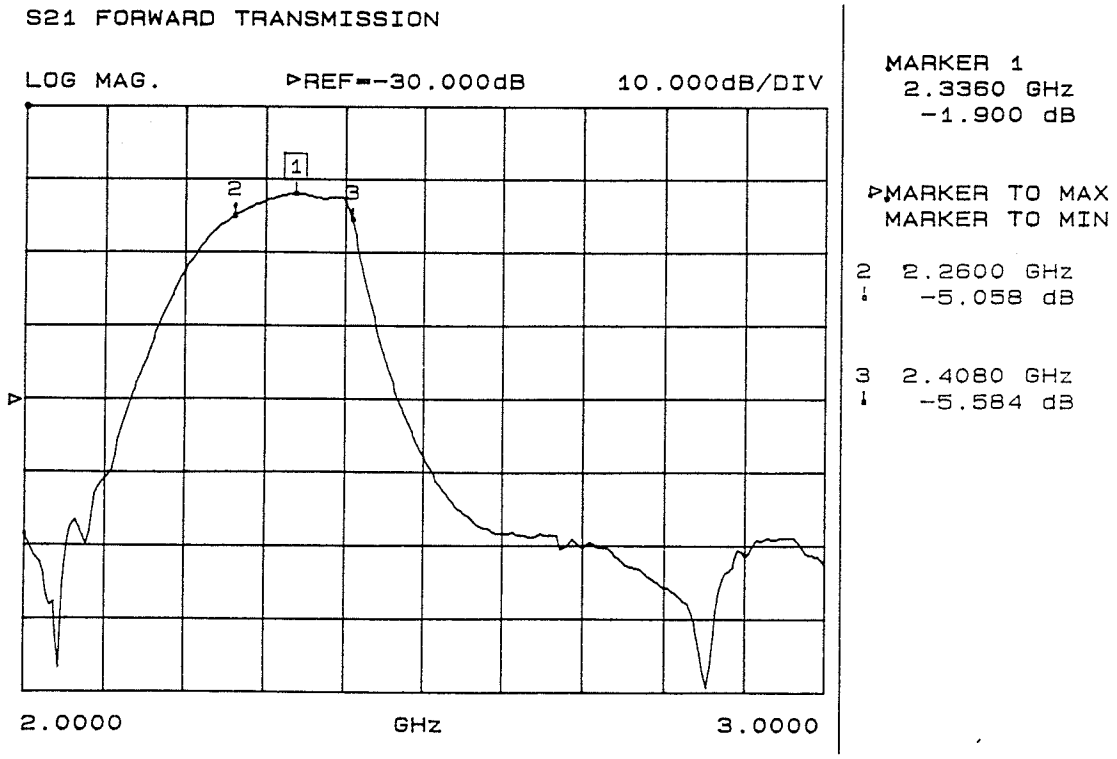


Figure 7.10. Calibrated $S_{21}$ measurement of bandpass filter.

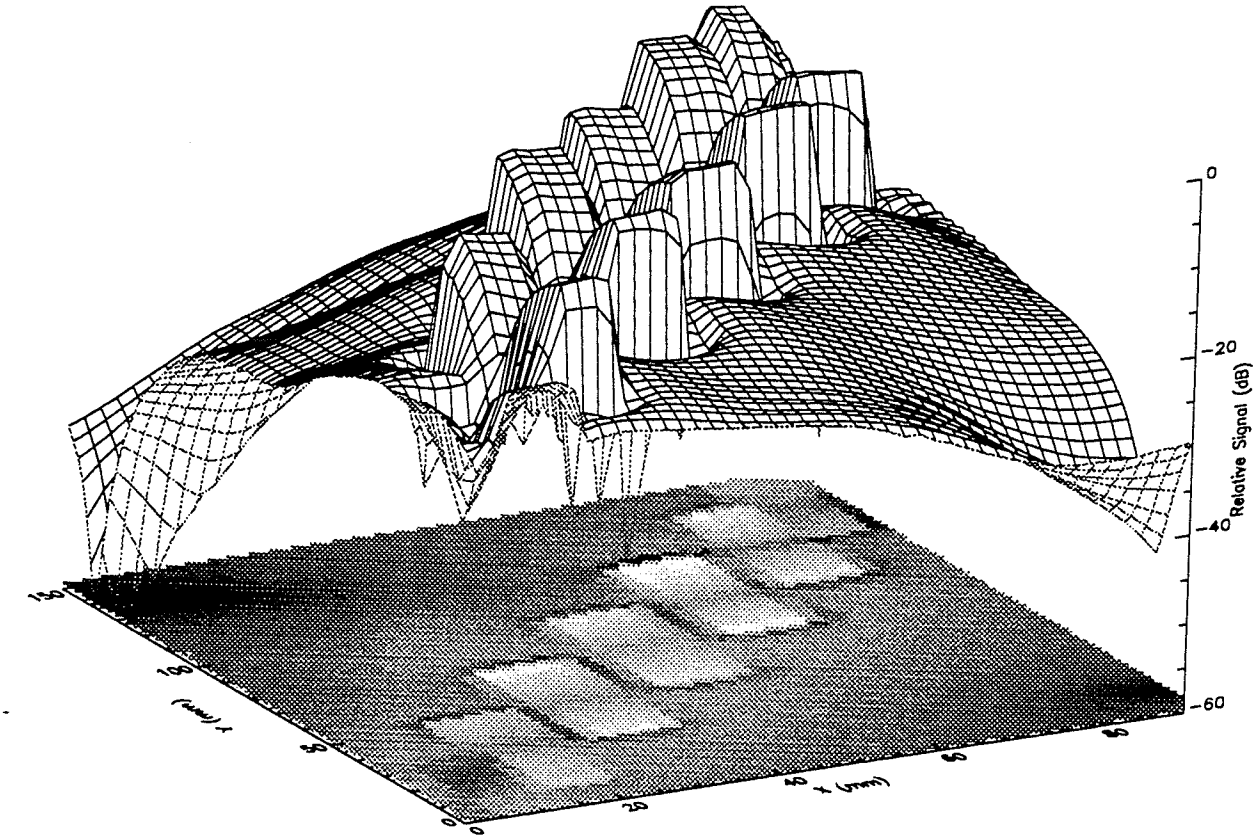


Figure 7.11a. Surface plot of the relative magnitude of the normal electric field component on the filter at 2.31 GHz.

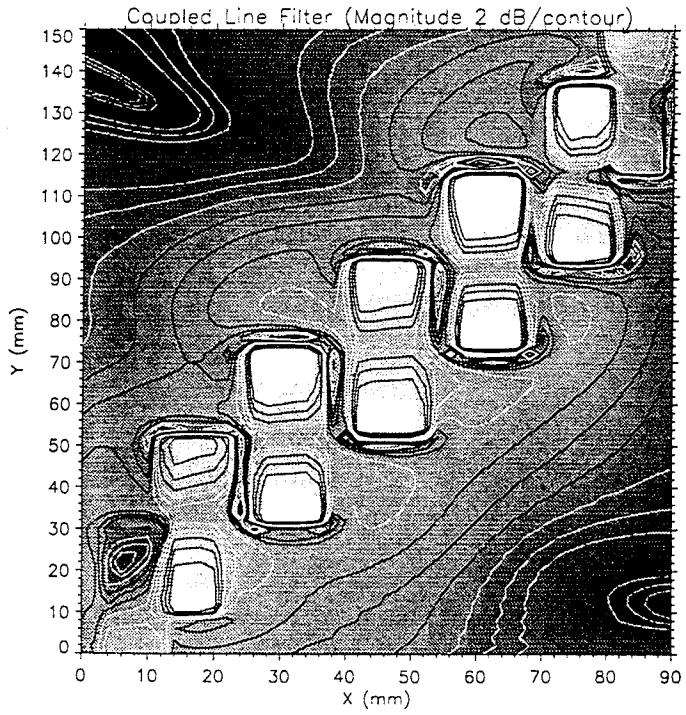


Figure 7.11b. Contour plot of the relative magnitude of the normal electric field component on the filter at 2.31 GHz.

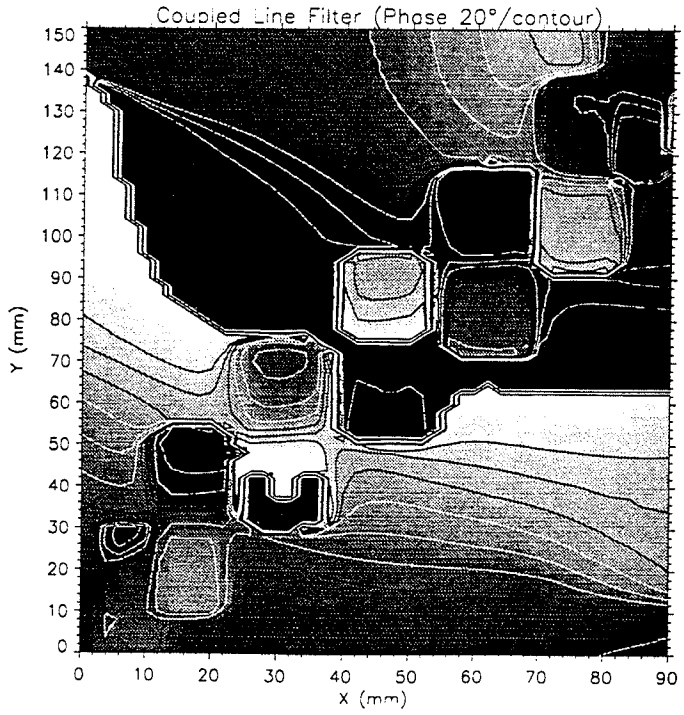


Figure 7.11c. Contour plot of the relative phase of the normal electric field component on the filter at 2.31 GHz.

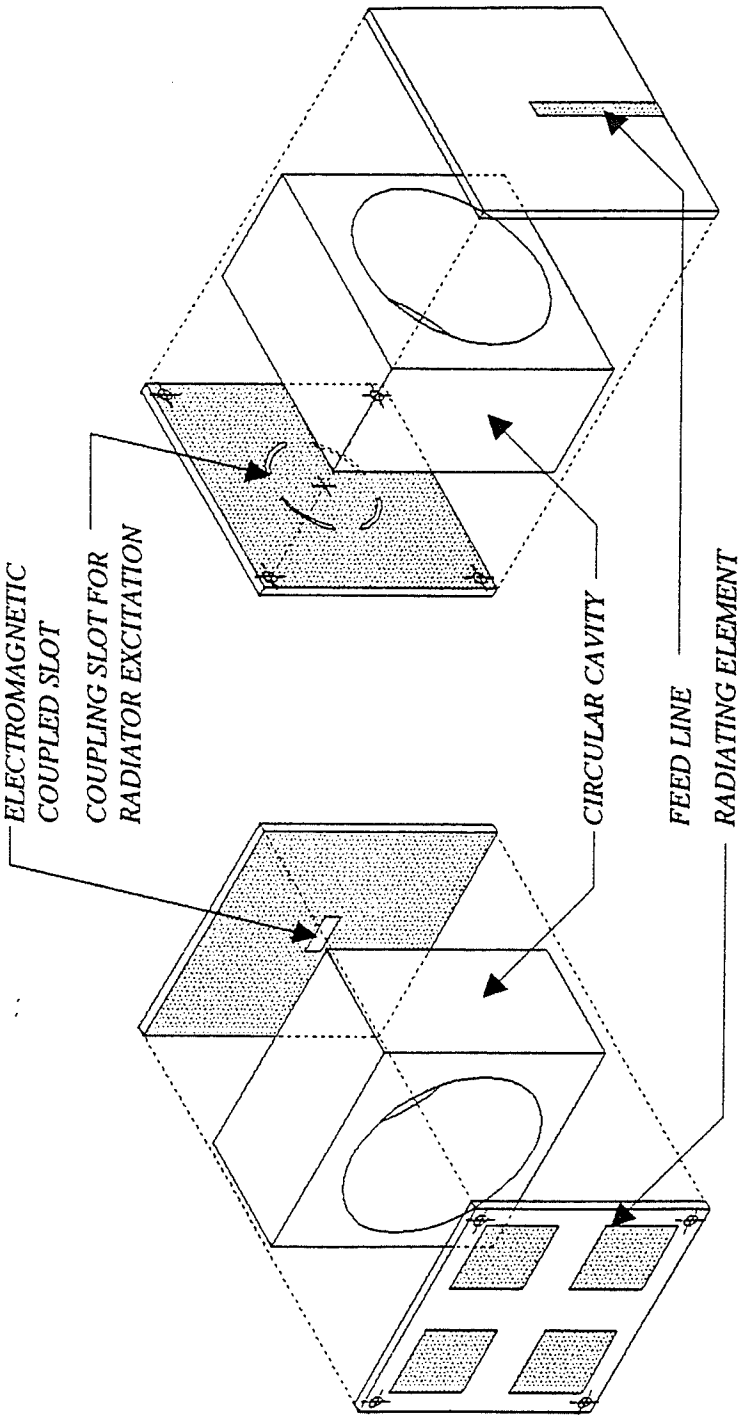


Figure 7.12a. Front and rear view of the cavity resonator antenna.

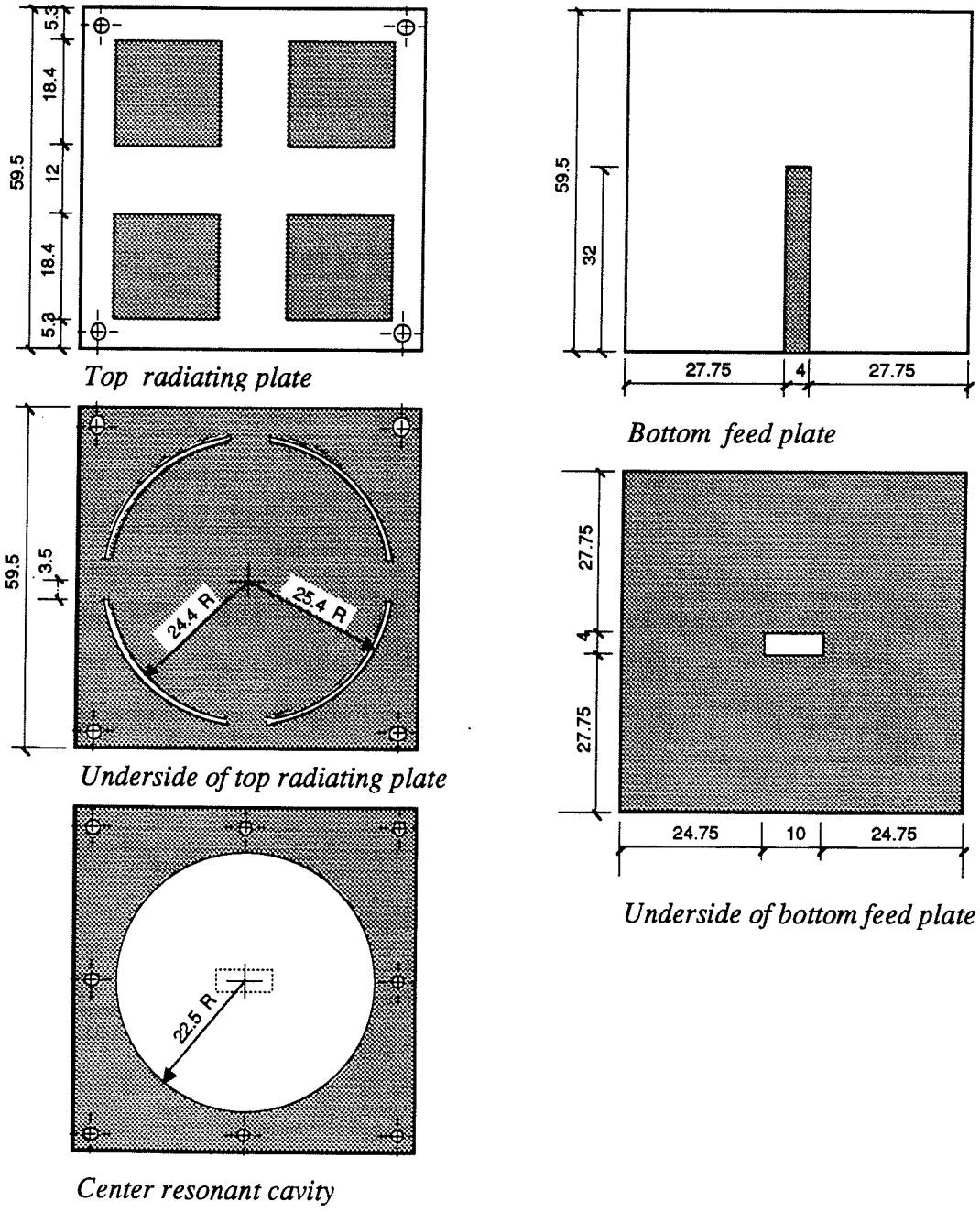


Figure 7.12b. Dimensions (mm) of the individual plates comprising the cavity resonator antenna. Shaded area is copper. Middle panel is 30 mm deep.

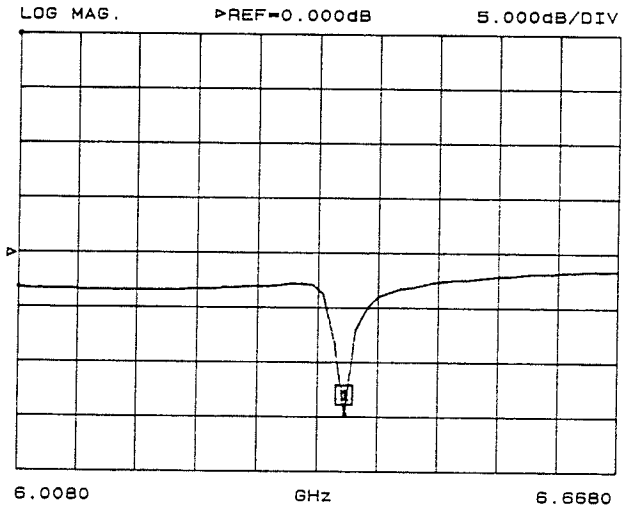


Figure 7.13. Calibrated $S_{11}$ measurement of the cavity resonator antenna.

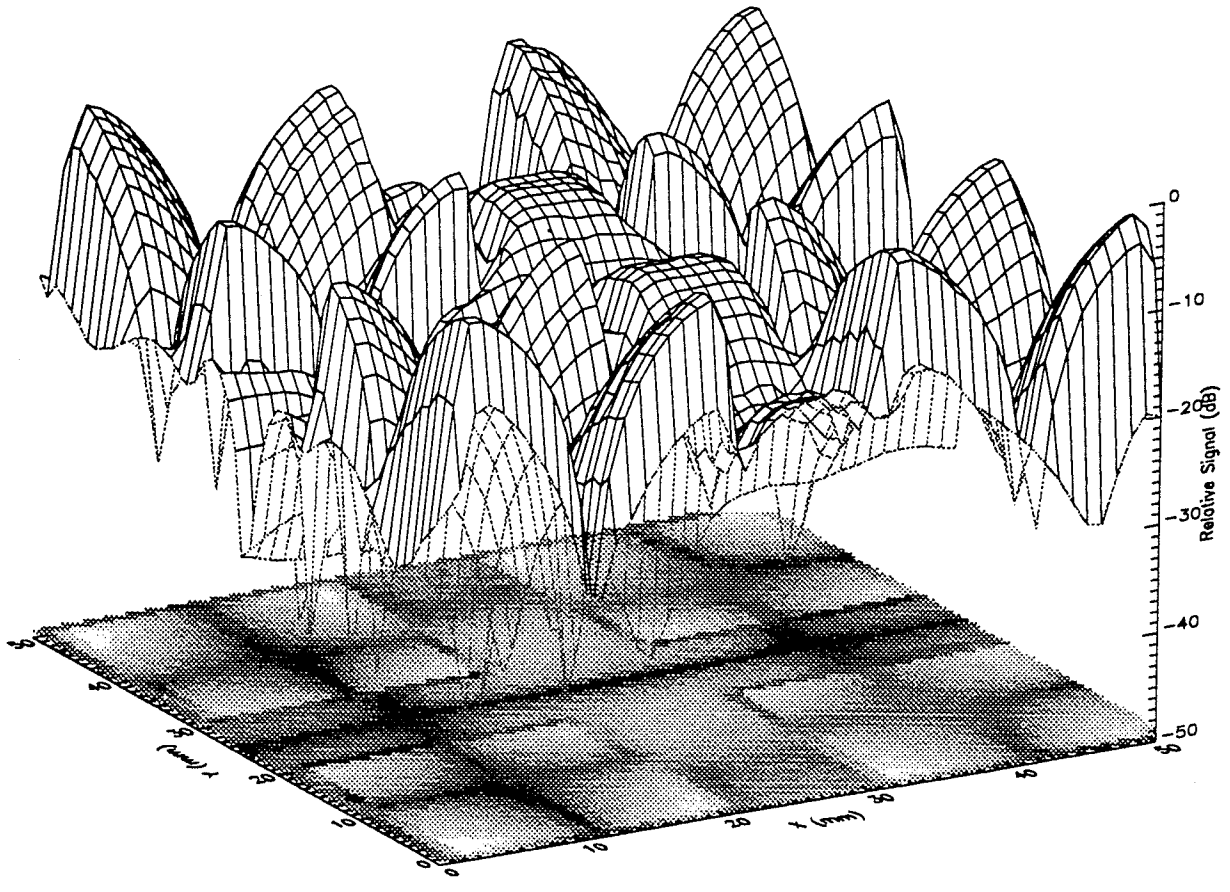


Figure 7.14a. Surface plot of the relative magnitude of the normal electric field component on the top plate of the cavity resonator antenna at 6.363 GHz.

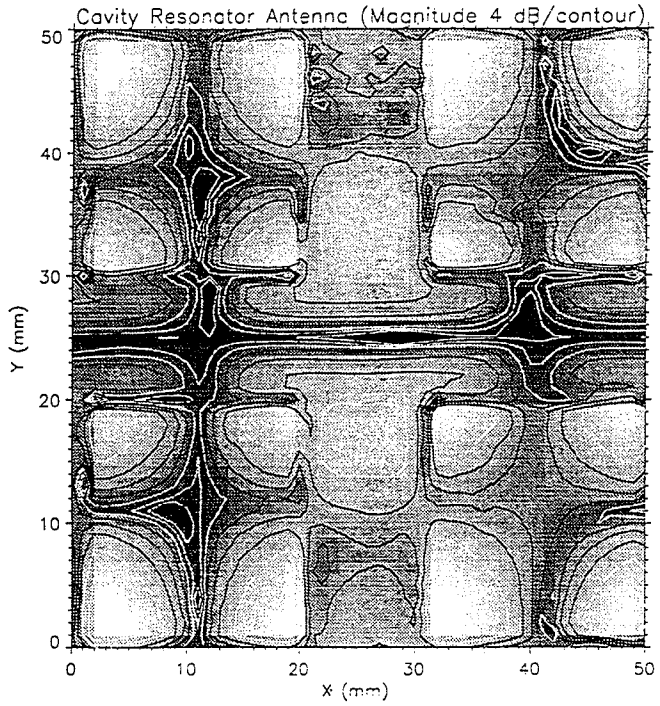


Figure 7.14b. Contour plot of the relative magnitude of the normal electric field component on the top plate of the cavity resonator antenna at 6.363 GHz.

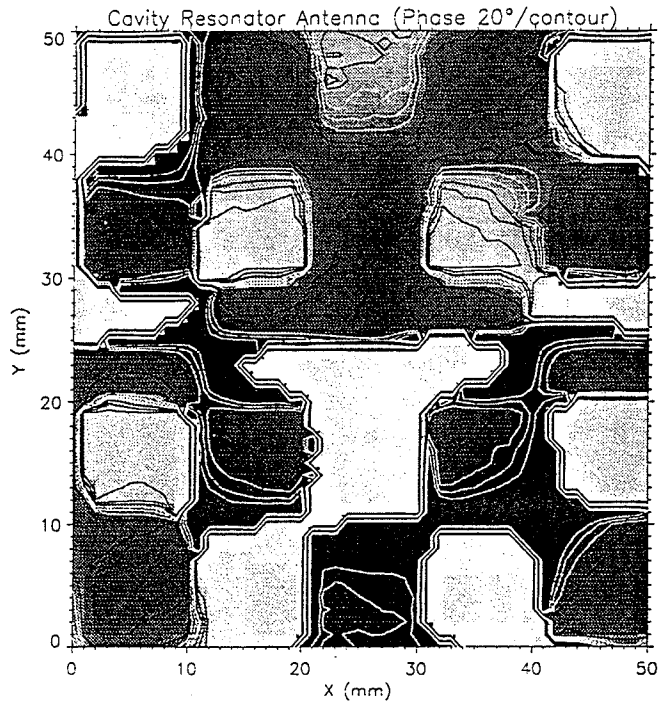


Figure 7.14c. Contour plot of the relative phase of the normal electric field component on the top plate of the cavity resonator antenna at 6.363 GHz.

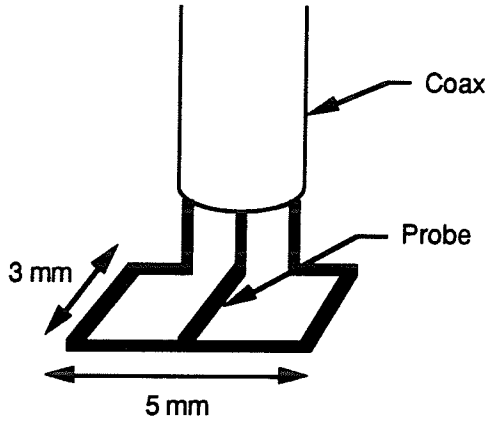


Figure 7.15. Double loop probe mounted on the end of a semi-rigid coax.

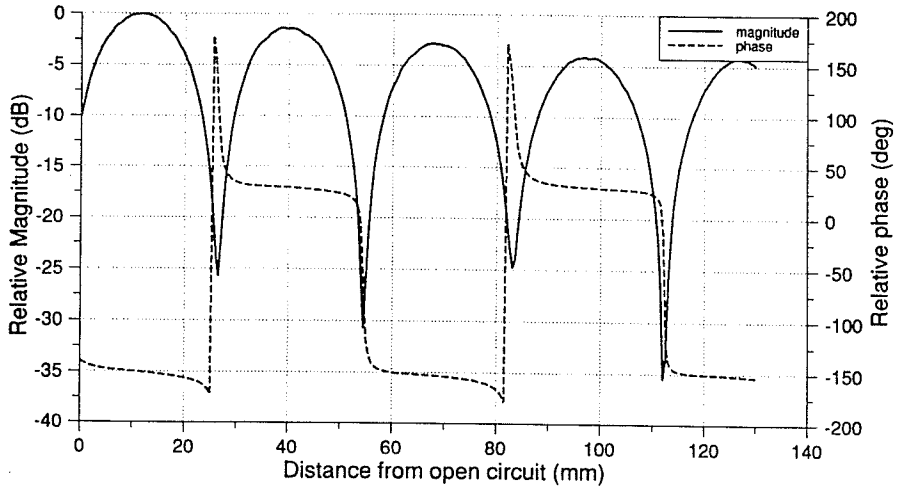


Figure 7.16a. CSW on an open circuit microstrip line at 2 GHz.

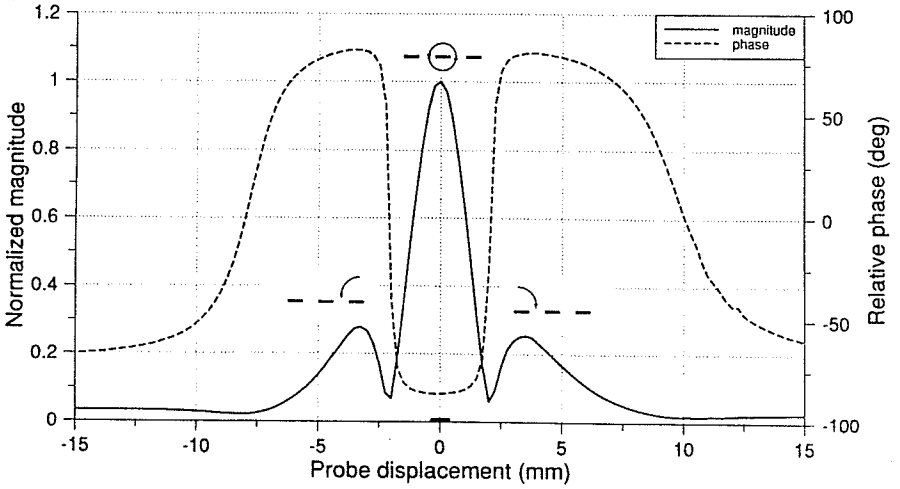


Figure 7.16b. Transverse scan of an open circuit microstrip line at 2 GHz.

# Chapter 8

## Conclusions

The application of electromagnetically coupled probes for microwave integrated circuit diagnostics has been investigated. Being non-contacting in nature such probes are much less likely to disturb the normal operation of the circuit being tested and are critical in the future development of non-invasive measurement systems.

The primary focus of this thesis was on the capacitively coupled monopole probe. Such probes are easily fabricated from standard semi-rigid coaxial cable in a variety of sizes. Currently, the smallest such coax commercially available has an outer diameter on the order of 200 μm. The smallest feature size which can be analyzed with such probes depends on a number factors. While the coax outer diameter is significant, the operation frequency and standing wave ratio on the device under test must also be taken into consideration. To quantify the resolution both an experimental and theoretical analysis on probes of various sizes and tip lengths is recommended. In order to examine integrated circuits where micron resolution is required further research is required into alternative probe designs [56].

One limitation of the monopole probe is the measurement error due to magnetic field coupling arising from the transverse magnetic field component. Typically the useable bandwidth is a function of the probe dimensions which must be a fraction of the wavelength in the medium being measured and the tolerable error arising from undesired inductive coupling.

The spatial resolution of the probe has been analyzed by numerically modeling a probe/transmission line structure. As a first order approximation a static analysis was performed. The appropriate integral equation was formulated and the Green's functions

derived. The formulation is general enough to model either microstrip or buried transmission lines. The integral equation was solved using using a method of moments solution with a subsectional pulse expansion basis for the charge distribution and a point testing basis. An approximation to the Green's function was derived in order to reduce computation time. Experimental results compared favorably with the theoretical analysis.

An alternative method for dispersion measurements has been presented. This method allows for the direct measurement of the magnitude and phase of the VSW on the line. An advantage of this technique is that the presence of higher order modes can be directly measured and their excitation at circuit discontinuities can be monitored. The maximum rms errors of the various experimental techniques were; sliding load magnitude 3.66%, VSW (combined magnitude and phase) 2.64%, sliding load (phase) 2.02%, and ring resonator 1.28% . The validity of these error calculations depends on the tolerances of the substrate, the t/h ratio, and the calculation of $\varepsilon_{re}(0)$ which all increase the uncertainty of the calculated values obtained from [32]. The VSW technique would yield better best results on a substrate where there is only one test line with sufficient substrate spacing to eliminate the effects of a finite ground plane. It is particularly useful for applications involving inhomogeneous dielectric substrates and/or passivated transmission lines for which formulas are unavailable or require significant modification. The error in the calculated $\varepsilon_{re}$ is roughly double the error in the measured guided wavelength obtained from either the sliding load or direct VSW measurement technique. Therefore, while good agreement may be observed in the guided wavelength results, this does not guarantee accurate results for $\varepsilon_{re}$.

A variety of applications including coplanar waveguides, coupled line filters, travelling wave, GaAs slot, and cavity resonator antennas have been analyzed at frequencies up to 22 GHz with the scanning near-field monopole probe. The results agreed with the established theory and provide some information unavailable from conventional measurement instruments. A double loop probe was fabricated for preliminary testing. The current standing wave on an open circuit microstrip line was measured with the loop probe.

The automated data acquisition system developed relied on the GPIB interface for information exchange between the measurement device and the computer. It is capable of driving two translation tables for mm and μm resolution applications. This combination has proven to be extremely versatile and flexible. It is recommended that a single software package be developed to incorporate both single and multi-frequency scans with the following options; (1) 1D scan, (2) 2D scan, and (3) a digitized scan path.

# Appendix A

## EMDAP Software Documentation

In order for all software options to function properly the hardware must be appropriately configured. Depending on the measurement system configuration either the GPIB (National Instruments PC II) or Dash-16 multifunction card must be installed.

### A.1 One Dimensional Scans

#### A.1.1 Single Frequency Scans

The EMDAP1D program used for 1D scans at a single operating frequency is compatible with both the HP7220C plotter and CTC-823 DC motor controller for mm and μm resolution respectively. The program is compatible with GPIB or Dash-16 operation.

Upon execution of the program the user will be prompted to specify a variety of parameters. The program proceeds with the data acquisition in the following manner:

1) User specifies hardware configuration.
2) User specifies either a horizontal or vertical scan.
3) User defines the start and stop points for the scan.
4) User specifies the filename, operating frequency, sampling interval, and averaging value.
5) Computer begins data acquisition.
6) Computer prompts user to enter notes for later reference.
7) Computer files data and statistics.

The file with the data and user entered comments will be appended with the extension .1D and is format compatible with the RPLOT software.

### A.1.2 Multi-Frequency Data Acquisition

The EMDAP1DMF program is used for obtaining experimental data for multiple frequencies in a single scan. This program eliminates the need for successive runs of the EMDAP1D program. The user has the option of specifying a list of frequencies or by entering a start frequency, delta frequency, and the number of test frequencies. To facilitate the multi-frequency option a GPIB network analyzer such as the Wiltron 360 is required. A tutorial on the operation of this software is provided in section A.3.

## A.2 Two Dimensional Scans

A 2D scan program called EMDAP2D has been developed. An algorithm has been developed to implement the zig-zag scan pattern as shown in Fig. A.1. The zig-zag pattern was chosen since it is the most time efficient.

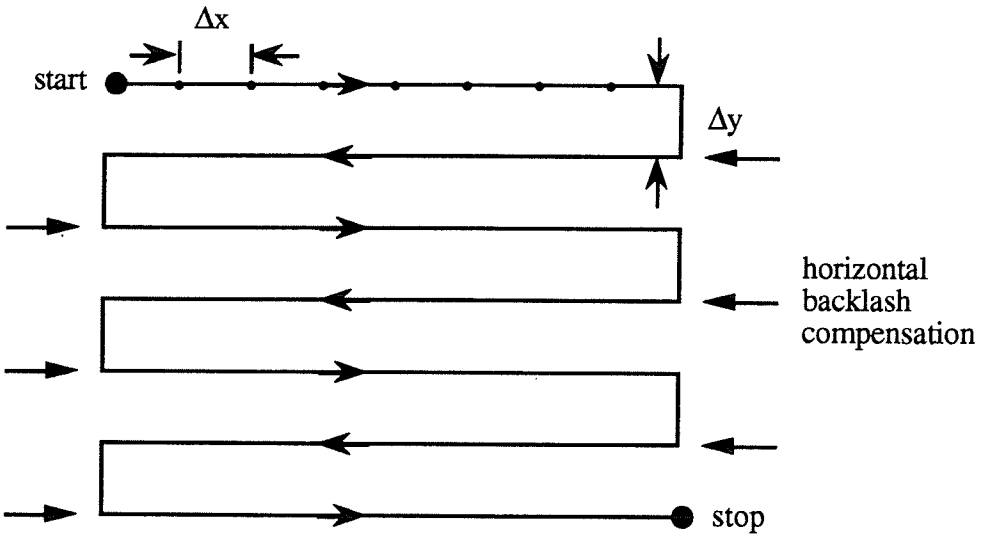


Figure A.1. Zig-zag scan pattern with horizontal backlash compensation.

For experiments which require sampling intervals on the order of microns, the CTC-823 DC motor controller is used. However, the backlash of the motors must be accounted for in the software. The backlash compensation as indicated in Fig. A.1 is asserted only in the horizontal direction as the vertical direction is unilateral. At the end of each horizontal scan the backlash compensation is invoked in the direction of the next scan to begin. A compensation of 10 μm has been incorporated into the software and can be easily changed if required. Upon returning to the start point to begin the data acquisition an initial backlash

compensation is undertaken in both the horizontal and vertical directions. The HP7220C plotter is assumed to be backlash free for sampling intervals in the mm to sub-mm range.

## A.3 EMDAP Tutorial

The following is a tutorial on how to use the EMDAP1DMF program. The software is self explanatory and can be used effectively and efficiently with limited training. The 1D and 2D programs operate in a very similar manner.

### A.3.1 Using EMDAP1DMF

As an example let's assume that we wish to scan a microstrip line using the plotter for manipulating the probe. Upon executing EMDAP1DMF a title page will appear and you will be prompted to select either the plotter or DC motors for operation. To select the plotter simple press the 'P' key.

### A.3.2 Defining the Scan Path

With the translation table chosen, the next step is to select either a horizontal or vertical scan path relative to the front of the plotter. The path is simply chosen by pressing 'H' or 'V' accordingly. The network analyzer will then enter the local lockout state and all buttons on the panel will be inoperative with the computer assuming total control. The following message will then appear on the monitor:

```
Use the keypad on the DC motor controller or the plotter
arrow keys to define the start and end points.

F1 to lock in point co-ordinates
F2 to display the distance between the starting and current position

Locate the starting point...
```

Following the instructions, move the probe to point $P_1$ as shown in Fig. A.2. Then by pressing the F1 key the points coordinates will be locked in and you will be prompted to locate the destination point. If you wish to know the distance between $P_1$ and any other point the F2 key can be used. For instance, if the F2 key is pressed when the probe is at the point $P_2$ the computer will display the message $\Delta$=30.00 mm. Finally, proceeding to the destination point $P_3$ the co-ordinates are locked in by pressing F1 once again. The total scan path length will then be displayed on the monitor:

```
The total length to be scanned is: 100.00 mm
```

A scan path from $P_3$ to $P_1$ is equally acceptable.

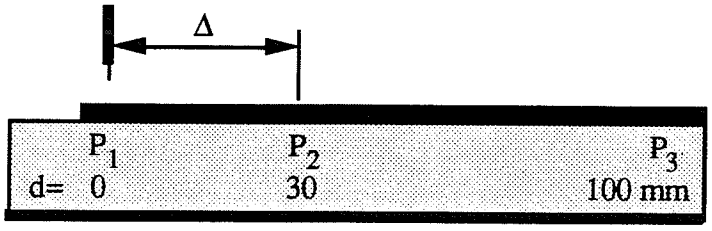


Figure A.2. One-dimensional multi-frequency scan of a microstrip line.

### A.3.3 Sampling Interval and Test Frequencies

With the scan path defined, the next step is to specify the sampling interval and test frequencies. Assuming a 1 mm sampling interval with an averaging value of 50 and test frequencies of 1.5, 2.5, and 3.5 GHz, the questions posed and the proper responses would be as follows:

```
Enter the step size in mm (min=0.025): 1.0
Enter the averaging value (1 to 4095): 50

Would you like a discrete frequency Sweep or would you like to
input a List of test frequencies? S

Input initial frequency (GHz): 1.5
Input frequency increment (GHz): 1.0
Input the number of test points: 3
Input a filename (max 8 chars): MLINE

There are 101 samples in the horizontal direction.

Press enter to continue...
```

Alternatively, one could enter an arbitrary list of test frequencies. The network analyzer will then undergo an initialization routine and display a $S_{21}$ magnitude and phase plot. Three markers are set at the start, center, and stop frequencies for reference. Following this the computer will echo all input information to the display for verification. In addition, a message will appear which prompts you to select the test frequency for which you would like the $S_{21}$ measurements to be displayed on the monitor. The test frequencies are indexed by an integer beginning at the lowest frequency.

### A.3.4 Data Acquisition

With all the test parameters specified, the data acquisition process will begin automatically with the data displayed on the computer monitor as follows:

```
Frequency (GHz): 2.5
Magnitude  (dB): X
Phase     (deg): Y
Remaining Samples: 100
```

where X and Y are the magnitude and phase values of $S_{21}$ at the specified test frequency for observation, in this case 2.5 GHz.

Upon completion of the scan, the data is written to disk and the user has the option of adding comments to the data file. Finally, the user has the option of scanning the same path, defining a new path, or to exit to DOS.

### A.3.5 Data File

The final MLINE.1D file which is format compatible with the RPLOT graphics software would be similar to the following.

```
%% MLINE.1D
%%  f1= 1.5000 GHz
%%  f2= 2.5000 GHz
%%  f3= 3.5000 GHz
%% Total samples:  101
%% Number readings per point: 50
%% Scan path length: 100.0000 mm
%% Sampling interval: 1.000 mm
%% Scan start time: 12:10:30.00
%% Scan stop time: 12:25:40.35
%%
%% Comments would be saved here
%names distance magf1 phsf1 magf2 phsf2 magf3 phsf3
  0.000  -34.955  -77.090  -30.970  132.871  -34.798  -94.663
  1.000  -34.951  -75.238  -31.005  136.106  -34.846  -89.651
    .        .        .        .        .        .        .
    .        .        .        .        .        .        .
    .        .        .        .        .        .        .
100.000  -30.901   25.127  -27.565  100.205   20.045  160.042
```

The lines preceded with %% are ignored by RPLOT and the %names line labels each column of the data file accordingly.

# Appendix B

## Hardware Configuration

Table B.1 summarizes the hardware configuration for the HP7220C plotter, National Instruments GPIB PCII card, and the Dash-16 A/D card. The Dash-16 card is to be used when a GPIB compatible measurement device is unavailable and an independent analog to digital converter is required [57]. The CTC-823 DC motor controller is configured by software commands issued by the EMDAP software.

Table B.1. Hardware configuration for plotter, GPIB card, and A/D card.

| HP7220C Plotter | |
|---|---|
| Baud Rate | 2400 |
| SW1 | OFF |
| SW2 | NORM |
| SW3 | OFF |
| SW4 | EVEN |
| SW5 | FULL |
| SW6 | HARDWIRE |
| GPIB PCII | |
| Base I/O address | $2B8 |
| DMA channel | 1 |
| IRQ line | 5 |
| DASH-16 | |
| Base address | $200 |
| Gain | 1 |
| A/D | BIP |
| Channel Config. | 16 |
| DMA | 1 |

# References


[1] P.G. May, Editorial, *IBM Journal of Research and Development*, vol. 34, pp. 139-140, March/May 1990.

[2] N. Richardson, "E-beam probing for VLSI circuit debug," *VLSI Systems Design*, vol. 8, p. 24, Aug. 1987.

[3] W.T. Lee, "Engineering a device for electron-beam probing," *IEEE Design and Test of Computers*, pp. 36-48, June 1989.

[4] H. Todokoro, S. Fukuhara, and T. Komoda, "Electron-beam LSI tester," *Japan annual reviews in electronics, computers and telecommunications*, vol. 13, pp. 373-382, edited by J. Nishizawa, North-Holland, 1984.

[5] K. Ura and H. Fujioka, "Function testing of semiconductor devices with stroboscopic scanning electron microscope," *Japan annual reviews in electronics, computers and telecommunications*, pp. 308-327, edited by J. Nishizawa, North-Holland, 1982.

[6] J. Wilson and J.F.B. Hawkes, *Opotoelectronics An Introduction*, Prentice Hall, Great Britain, 1989.

[7] W. Mertin, C. Bohm, *et al*, "Two-dimensional field mapping in MMIC-substrates by electro-optic sampling technique," *IEEE MTT-S Digest*, pp. 1443-1446, 1992.

[8] J. Valdmanis, "Advanced electro-optic sampling permits non-invasive testing of IC performance," *Electronic Engineering*, pp. 35-42, Feb. 1989.

[9] K.A. Nickerson, G. Pakulski, D.R. Conn, "Electro-optic measurement technique for millimeter wave antennas," *Proc. 1990 ANTEM Conference*, pp. 330-336, Winnipeg, Canada, Aug. 1990.

[10] J.M. Wiesenfield, "Electro-optic sampling of high-speed devices and integrated circuits," *IBM Journal of Research and Development*, vol. 34, pp. 141-161, March/May 1990.

[11] D.R. Hjelme and A.R. Mickelson, "Voltage calibration of the direct electro-optic sampling technique," *IEEE Trans. Microwave Theory Tech.*, vol. MTT-40, pp. 1941-1950, Oct. 1992.

[12] S.S. Osofsky and S.E. Schwarz, "Design and performance of a non-contacting probe for measurements on high-frequency planar circuits," *IEEE Trans. Microwave Theory Tech.*, vol. MTT-40, pp.1701-1708, Aug. 1992.

[13] S.S. Osofsky and S.E. Schwarz, "A non-contacting probe for measurements on high-frequency planar circuits," in *1989 IEEE MTT-S Int. Microwave Symp. Digest*, Long Beach, California, vol. II, no. BB-1, pp. 823-825, June 1989.

[14] P.G. Frayne and J. Whitehurst, "Mode analysis in radiating and non radiating planar open structures using a scanning microwave probe," *IEE Conf. on Antennas and Propagation*, London, 1988.

[15] P.G. Frayne and A.J. Leggetter, "A surface field technique for printed antennas," *IEE Conf. on Antennas and Propagation*, UK, 1989.

[16] P.G. Frayne, *The Handbook of Microstrip Antennas*, Peter Peregrinus Ltd, London, United Kingdom 1989, Chapter 21 "Microstrip field diagnostics," pp. 1193-1225.

[17] T.S. Forzley, "Near field probes for mapping of high frequency circuits," *B. Sc. Thesis*, University of Manitoba, Dept. of Electrical and Computer Engineering, Mar. 1990.

[18] T.S. Forzley and G.E. Bridges, "Field probe for high-frequency planar circuit measurements," *Proceedings of the Canadian Conference on Electrical and Computer Engineering*, vol. II, pp. 70.3.1-70.3.4, Ottawa, Canada, Sept. 1990.

[19] G.E. Bridges, T.S. Forzley, and D.J. Thomson, "Novel near field probe for on-wafer integrated circuit measurements," *Proceedings of the Canadian Conference on Very Large Scale Integration*, pp. 1.1.1-1.1.8, Kingston, Canada, Aug. 1991.

[20] J.R. Wait, *Electromagnetic Wave Theory*, Harper and Row, New York, 1985.

[21] R.F. Harrington, *Field Computation by Moment Methods*, Macmillan, New York, 1968.

[22] T.S. Forzley and G. Bridges, "Numerical and experimental analysis of electric and magnetic field sensors for printed circuit board fault testing," Final Report, National Research Council, Contract XSF90-00014-(304), Sept. 1990, 39 pages.

[23] K.C. Gupta, R. Garg, and I.J. Bahl, *Microstrip Lines and Slotlines*, Artech House, Dedham, Mass., 1979.

[24] H. A. Atwater, "Test of microstrip formulas," *IEEE Trans. Microwave Theory Tech.*, vol. MTT-36, pp. 619-621, Mar. 1988.

[25] P. Pramanick and P. Bhartia, "An accurate description of dispersion in microstrip ," *Microwave Journal*, pp.89-96, Dec. 1983.

[26] M.V. Schneider, "Microstrip dispersion," *Proc. IEEE*, vol. 60, pp. 144-146, Jan. 1972.

[27] R.E. Collin, *Field Theory of Guided Waves*, McGraw-Hill, New York, 1960.

[28] W.J. Getsinger, "Microstrip dispersion model," *IEEE Trans. Microwave Theory Tech.*, vol. MTT-21, pp. 34-39, Jan. 1973.

[29] T.C. Edwards and R.P. Owens, "2-18 GHz dispersion measurements on 10-100 ohm microstrip lines on sapphire," *IEEE Trans. Microwave Theory Tech.*, vol. MTT-24, pp. 506-513, Aug. 1976.

[30] E. Hammerstad and O. Jensen, "Accurate models for computer-aided design," in *IEEE MTT-S Int. Microwave Symp.*, pp. 407-409, June 1980.

[31] E. Yamashita, K. Atsuki, and T. Veda, "An approximate dispersion formula of microstrip lines for computer-aided design of microwave integrated circuits," *IEEE Trans. Microwave Theory Tech.*, vol. MTT-27, pp. 1036-1038, Dec. 1979.

[32] M. Kobayashi, "A dispersion formula satisfying recent requirements in microstrip CAD," *IEEE Trans. Microwave Theory Tech.*, vol. MTT-36, pp. 1246-1250, Aug. 1988.

[33] M. Kirschning and R. Jansen, "Accurate model for effective dielectric constant of microstrip up to millimeter wave frequencies," *Electron. Lett.*, vol. 18, pp 272-273, Mar. 1982.

[34] M. Kobayashi, "Important role of inflection in the dispersive properties of microstrip line," *IEEE Trans. Microwave Theory Tech.*, vol. MTT-30, pp. 2057-2059, Nov. 1982.

[35] M. Kobayashi and F. Ando, "Dispersion characteristics of open microstrip lines," *IEEE Trans. Microwave Theory Tech.*, vol. MTT-35, pp. 101-105, Feb. 1987.

[36] M. Kobayashi, "Analysis of the microstrip and the electrooptic light modulator," *IEEE Trans. Microwave Theory Tech.*, vol. MTT-26, pp. 119-126, Feb. 1978.

[37] M. Kobayashi and R. Terakado, "Accurately approximate formula of effective filling fraction for microstrip line with isotropic substrate and its application to the case of anisotropic substrate," *IEEE Trans. Microwave Theory Tech.*, vol. MTT-27, pp. 776-778, Sept. 1979.

[38] K.C. Gupta, R. Garg, R. Chadha, *Computer-Aided Design of Microwave Circuits,* Artech House, Dedham, Mass., 1981.

[39] I.J. Bahl and R. Garg, "Simple and accurate formulas for a microstrip of finite strip thickness," *Proc. IEEE*, vol. 65, pp. 1611-1612, Nov. 1977.

[40] G. Kompa, "Planar waveguide model for calculating microstrip components," *Electron. Lett .*, vol. 11, pp. 459-460, Sept. 1975.

[41] D.W. Trim, *Calculus and Analytic Geometry,* Addison Wesley, 1984.

[42] G. Kompa, "Dispersion measurements of the first two higher-order modes in open microstrip," AEÜ-29, pp. 182-184, 1975.

[43] A.R. Van de Capelle and P.J. Luypaert, "Fundamental and higher-order modes in microstrip," *Electron. Lett.*, vol. 9, pp. 345-346, July 1973.

[44] S. Deibele and J. B. Beyer, "Measurements of microstrip effective relative permittivities," *IEEE Trans. Microwave Theory Tech.*, vol. MTT-35, pp. 535-588, May 1987.

[45] P. Troughton, "Measurement techniques in microstrip," *Electron. Lett.*, vol. 5, pp. 25-26, Jan. 1969.

[46] T.S. Forzley and G.E. Bridges, "Dispersion characteristics of open microstrip using a direct VSW measurement approach," *Proc. 1992 ANTEM Conference,* Winnipeg, Canada, Aug. 1992.

[47] H.J. Finlay, R.H. Jansen, *et al*, "Accurate characterization and modeling of transmission lines for GaAs MMIC's," *IEEE Trans. Microwave Theory Tech.*, vol. MTT-36, pp. 961-966, June 1988.

[48] R.P. Owens, "Curvature effect in microstrip ring resonators," *Electron. Lett.*, vol. 12, pp. 356-357, July 1976.

[49] E.L. Ginzton, *Microwave Measurements*, McGraw-Hill, New York, 1957.

[50] D.J. Roscoe, "A study of compatible radiating elements for MMIC/MHMIC applications," *M. Sc. Thesis*, University of Manitoba, Dept. of Electrical and Computer Engineering, May 1989.

[51] C.H. Walter, *Traveling Wave Antennas*, General Publishing Company Ltd., 1965.

[52] C.F. Liau, "Near field measurement of planar microwave circuits and antennas," *B. Sc. Thesis*, University of Manitoba, Dept. of Electrical and Computer Engineering, March 1992.

[53] L. Roy, M.G. Stubbs, J.S. Wight, "Slot antennas on GaAs for integrated array applications," *Proc. 1992 ANTEM Conference*, Winnipeg, Canada, Aug. 1992.

[54] R. Dorbolo, "Design and test of cyrogenicaly operated microwave circuits," *B. Sc. Thesis*, University of Manitoba, Dept. of Electrical and Computer Engineering, March 1991.

[55] A. Dhouib, Communications Research Centre, Ottawa, private communication.

[56] G.E. Bridges, T.S. Forzley, and D.J. Thomson, "Novel near-field probe for on-wafer integrated circuit measurements," *Microelectronics Journal*, vol. 23, pp. 363-369, 1992.

[57] V.T. Betz and N.P. East, "Calculation of far-field radiation pattern from near-field antenna measurements," *B. Sc. Thesis*, University of Manitoba, Dept. of Electrical and Computer Engineering, Mar. 1991.